research report

Energy Dissipation of Thin-Walled Cold-Formed Steel Members

RESEARCH REPORT RP13-2

JULY 2013

American Iron and Steel Institute

DISCLAIMER

The material contained herein has been developed by researchers based on their research findings and is for general information only. The information in it should not be used without first securing competent advice with respect to its suitability for any given application. The publication of the information is not intended as a representation or warranty on the part of the American Iron and Steel Institute or of any other person named herein, that the information is suitable for any general or particular use or of freedom from infringement of any patent or patents. Anyone making use of the information assumes all liability arising from such use.

VIRGINIA POLYTECHNIC INSTITUTE
AND STATE UNIVERSITY

The Charles E. Via, Jr. Department of
Civil and Environmental Engineering
Blacksburg, VA 24061

Structural Engineering and Materials

ENERGY DISSIPATION OF THIN-WALLED COLD-FORMED STEEL MEMBERS

by

David A. Padilla-Llano,
Graduate Research Assistant

Cristopher D. Moen, Ph.D., P.E.

Matthew R. Eatherton, Ph.D., P.E., S.E.

Report No. CE/VPI-ST-13/06

July 2013

Summary

Design of cold-formed steel (CFS) structures subjected to lateral seismic forces traditionally relies on the cyclic strength of subassemblages such as strapped/sheathed shear walls. Little regard is paid to the behavior of the individual components, their contribution to the lateral resistance of CFS structures, or to the actual seismic behavior of the structure as a whole. Understanding the cyclic behavior at the individual component level is necessary to develop accurate and computationally efficient models, a toolbox of nonlinear elements, capable of accurately and efficiently simulating the seismic behavior of CFS members and the infinite number of possible configurations in cold-formed steel structures.

This report summarizes results from a research program designed to investigate the cyclic behavior and energy dissipation of cold-formed steel C–sections structural axial and flexural framing members. Twenty four axial tests and 24 flexural tests were performed to evaluate the energy dissipation characteristics of axial and flexural members experiencing global, distortional and local buckling deformations. Specimen cross-section dimensions and lengths were selected to isolate the specific buckling modes. A cyclic loading protocol is adapted for cold-formed steel members to evaluate the energy dissipation characteristics. The protocol target displacements are defined based on elastic buckling properties.

Experimental data is utilized to calibrate a hysteretic model that represents the cyclic response of cold-formed steel C-section structural framing members. The model includes strength degradation, unloading stiffness degradation and pinching behavior of the observed experimental response. Model parameters and damage rules are calibrated for local, distortional and global buckling based on the hysteretic energy dissipated. The calibrated parameters can be utilized to develop a toolbox of nonlinear hysteretic springs to represent framing axial members in CFS structures for seismic analysis and facilitate performance based earthquake engineering of CFS structures.

Keywords: *Cold-formed steel, seismic energy dissipation, hysteretic behavior, buckling, thin-walled.*

Contents

1 Introduction

Current seismic analysis and design procedures for cold-formed steel (CFS) frame buildings focuses on the strength of individual shear wall units [1], e.g., shear walls constructed with CFS steel members sheathed with Structural 1 plywood (4 ply), oriented strand board (OSB), gypsum board, or thin sheet steel or strap bracing. These systems are designed using prescriptive procedures and tabulated values that are based on an extensive number of shear wall tests. Although this design methodology is expected to provide adequate protection against collapse during design level seismic events, it provides little information about the predicted seismic performance of the actual CFS structures. Actual CFS buildings comprise a wide range of structural layouts that include, besides shear walls, odd geometries (e.g. intersecting walls), load transfer mechanisms not included in tests, and many gravity resisting elements and connections. Research efforts to characterize the response and develop models for CFS lateral load resisting systems typically focus as well on the response of shear walls to push-over and cyclic tests (e.g. [2]). Specific guidance about energy dissipation or strength degradation for the design of these systems, their components (e.g., drag struts, boundary chord studs), and other components of CFS buildings is not readily available either.

The shift of earthquake engineering towards performance-based design of structures in last twenty years has created considerable interest in understanding and controlling the seismic performance of structures at different seismic hazard levels. Furthermore, to develop proper seismic performance factors it is necessary to consider suites of ground motions, ground motion intensities and consideration of different structural configurations [3]. This translates into a sizable number of analyses that require efficient and reasonably accurate modeling tools capable of capturing the structural response of the different structural components of CFS buildings. Such tools will be useful to perform nonlinear dynamic time-history analysis and incremental dynamic analysis of CFS framed buildings, which are necessary for a performance based earthquake design. Fig. 1.1 demonstrates the concept for simulating CFS framing using aforesaid tools where hysteretic springs, calibrated using experimental data from cyclic tests, can be employed to represent each of the members and connections. In order to develop a modeling toolbox like the one just mentioned, it is

necessary to investigate and characterize the cyclic behavior and energy dissipation of individual CFS systems, member components and connections. In the spirit of this goal, this report summarizes results and finding from a research project that investigates the cyclic behavior, and energy dissipation characteristics CFS axial and flexural members.

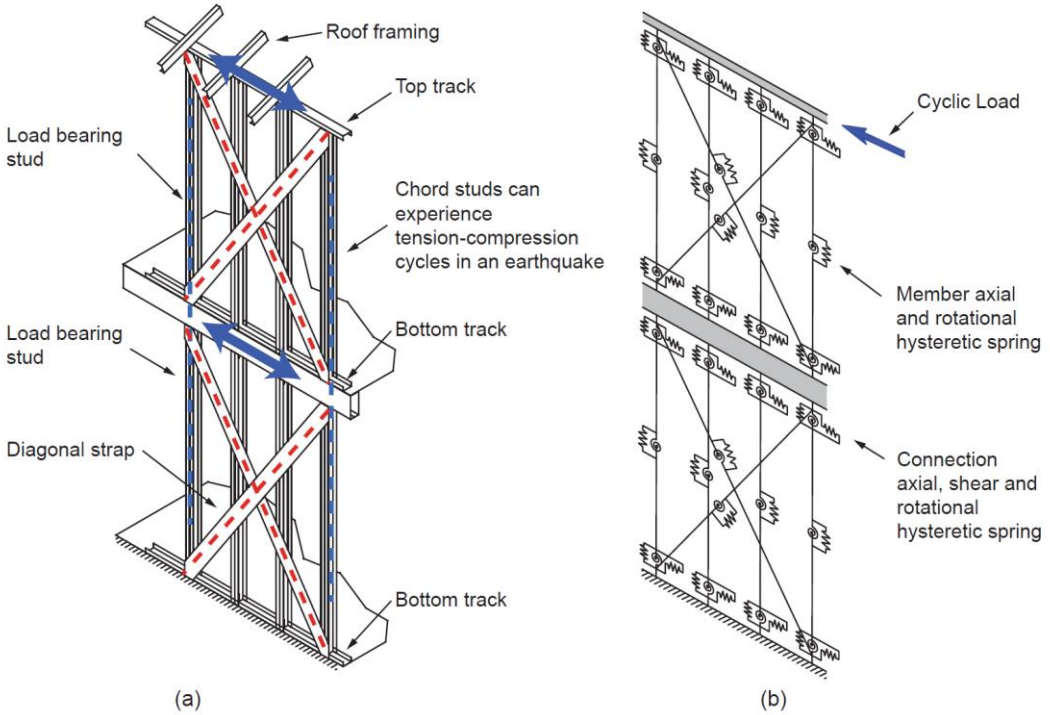

Fig. 1.1. Cold-formed strap bracing (a); and corresponding phenomenological model (b).

2 Research Program

The objective of this research project is to characterize the cyclic behavior and energy dissipation of cold-formed structural components subjected to axial or flexural deformations. To fulfill this objective a research program was devised that included cyclic and monotonic testing of CFS axial and flexural members that exhibit global, distortional or local buckling. The program consisted of the following major tasks:

1) establish a cyclic loading protocol for CFS axial and flexural members;
2) perform monotonic and cyclic test on CFS axial members;
3) perform monotonic and cyclic test on CFS flexural members; and
4) characterize the load-deformation responses to calibrate a hysteretic model that represents the cyclic behavior of CFS axial and flexural members.

The following sections describe the research details on completing these tasks. The report begins with a review of available literature that explores the cyclic behavior of axial and flexural members experiencing buckling, and provides context for the research summarized in this report. Next, the testing program to investigate the cyclic behavior and energy dissipation characteristics of CFS axial and flexural members is described. The report continues summarizing the experimental results of cyclic and monotonic test of CFS axial and flexural members exhibiting local, distortional and global buckling including a discussion about their energy dissipation characteristics. The calibration of a hysteretic model that represents the cyclic response of CFS members is also presented.

3 Background

Prior research on the behavior of structural sections subjected to cyclic axial and cyclic flexural loading are discussed to provide context for the current study.

3.1 Cyclic response of axial members including buckling

Cyclic axial tests have been performed on hot-rolled steel structural sections used for steel-framed buildings and offshore oil platforms. The cyclic axial behavior of globally slender steel members (struts, braces) has been studied starting in the early 1970s with analytical solutions and experimental programs. Analytical hysteretic response models for columns experiencing a plastic hinge were developed for use in finite element models [4–7]. Some of the models included cross-sectional slenderness as a softening parameter [8, 9]. The analytical models were combined with experimental data in a few cases to develop semi-empirical equations that predict bracing member fracture life, i.e., number of cycles to tensile fracture [10]. The viability of these analytical models was established by experiments on structural sections ranging from solid steel bars [4], to hollow thin-walled tubes [11], W-sections [12], and angles [13]. A few experiments even considered the influence of cold-bending on energy dissipation [14]. Some important conclusions from these studies included the following:

- Inelastic elongation during tensile excursions occurred in a relatively predictable manner [13].
- Tension strength remained fairly constant during inelastic cycles, but compression strength degraded with the number of cycles (implying damage accumulation in compression).
- When local buckling accompanied global deformation, the member failure mode was typically tensile fracture caused by stress concentrations at a fold.
- Inelastic deformation of the steel was the key contributor to energy dissipation as compared to inherent material damping
- The total energy dissipation appears to be independent of initial loading direction (tension then compression or compression and then tension) [13].
- The amount of total dissipated hysteretic energy decreases as the global

slenderness increases [11].

Only a few studies have focused on cyclic behavior associated with local buckling [15–18]. It was observed that local buckling compression strength degraded to a constant magnitude with increasing cycles, which is different than global buckling cyclic behavior where compression strength goes to zero as the plastic hinge develops. To the authors' knowledge, none of studies found in the literature investigated the cyclic behavior of CFS axial members that considered separately the different buckling limit states (i.e., global, distortional and local buckling) proper of thin-walled members. As such, the study described herein helps on filling the gap in the literature concerning the cyclic behavior of thin-walled axial members that experience local and distortional buckling.

3.2 Cyclic response of flexural members including buckling

Although there have been studies on the monotonic behavior of cold-formed steel flexural members (e.g. [19]), there have been considerable fewer studies on the cyclic performance of cold-formed steel flexural members. Calderoni et al., [18] tested back-to-back lipped C-sections loaded in three point bending to study local buckling cyclic strength degradation. Post-buckling ductility and inelastic energy dissipation were observed. Related studies included preliminary hysteretic modeling [20], and comparison between experimental and finite element simulation results [21]. Hsu and Chi [22] also performed cyclic tests on back-to-back cold-formed steel lipped C-sections with the goal of demonstrating a design alternative to hot-rolled steel I-beams in mid-rise buildings. Tests have also been performed on cold-formed steel flexural members as part of bolted steel moment frames (e.g. [23], [24]). The studies found in the literature have not isolated the cyclic flexural behavior of cold-formed steel members undergoing different buckling modes.

4 Experiments on CFS Axial Members

A testing program was conducted to study the cyclic response of CFS axial members experiencing local, distortional and global buckling. The testing program included twelve cyclic tests, twelve monotonic tests in compression, and two monotonic tests in tension, conducted on common CFS C-sections without perforations. Cyclic tests were conducted to determine the effects of reversed cyclic loading (i.e., tension and compression) and cumulative axial deformation on damage and hysteretic energy dissipation. Monotonic tests were performed to establish a load-deformation envelope for comparison to the cyclic test response.

4.1 Specimen selection strategy

Specimens are selected such that their predicted monotonic capacity in compression is governed either by local, distortional or global buckling as predicted by the AISI Direct Strength Method [25]. The cross-sections considered were selected from standard sizes as listed in the Structural Stud Manufacturers Association catalog [26]. Cross-section dimensions and length (L) were varied to isolate each buckling limit state. Long members (L=2286mm) were selected for global buckling, a shorter length (L=610mm) was selected for distortional buckling, and shortest members (L=305mm) for local buckling. Two different web depths (92mm and 152 mm) were selected. The test program included two specimens subjected to quasi-static cyclic displacement and two specimens subjected to monotonic displacement (in compression) per specimen type. Only two monotonic tests in tension were included to establish the envelope in the tension side. These two tests are considered here to be representative of the tension behavior of the tested CFS members. The test matrix is summarized in Table 4.1 (with nominal dimensions) and specimen nomenclature is explained in Fig. 4.1a.

4.2 Specimen dimensions, material properties and elastic buckling loads

Cross-section dimensions were measured at member mid-height using methods described in [27], see Table 4.2 and Fig. 4.1b. These values were utilized to calculate the elastic buckling loads for local buckling, $P_{cr\ell}$, distortional buckling, P_{crd}, and global buckling, P_{cre}, the associated half-wavelength for local and distortional buckling ($L_{cr\ell}$ and L_{crd}

respectively) with finite strip eigen-buckling analysis in the CUFSM software [28]. The boundary conditions were assumed to be warping fixed (i.e., fixed-fixed) when calculating the elastic buckling loads. Thus, an effective length of *0.5L* when calculating P_{cre} was considered. In addition, P_{crd} was calculated including the effects of warping-fixed ends [27] and half-wavelengths L_{crd} larger than the total member length [25]. The tension yield load, P_y, was determined using the measured cross-section area and the average yield stress F_y obtained from three coupon tests per specimen. Coupon tests were conducted in accordance with ASTM E8M-04 [29] with one coupon taken from each flange and one from the web. The monotonic compression capacity, P_n, was calculated using the AISI Direct Strength Method [25]. These values are summarized in Table 4.3.

Table 4.1. Test matrix with nominal dimensions and number of tests.

Specimen [(a)]	Buckling Limit [(b)]	L (mm)	H (mm)	B (mm)	t (mm)	No. of Cyclic Tests	No. of Monotonic Tests
362S162-54-LA#	Local	305	92	41	1.44	2	2
362S162-54-LA#T	$\lambda_\ell >> \lambda_d$ and λ_e	305	92	41	1.44	2	2
600S162-33-LA#		305	152	41	0.88	2	2
362S137-68-DA#	Distortional	610	92	35	1.81	2	2
600S137-68-DA#	$\lambda_d >> \lambda_\ell$ and λ_e	610	152	35	1.81	2	2
362S137-68-GA#	Global	2286	92	35	1.81	2	2
600S137-97-GA#	$\lambda_e >> \lambda_\ell$ and λ_d	2286	152	35	2.58	2	2

(a) A= Axial, G= Global, D= Distortional, L= Local, # indicates Cyclic or Monotonic, T = Tension

(b) λ_ℓ, λ_d and λ_e = local, distortional and global slenderness parameter respectively (AISI 2007)

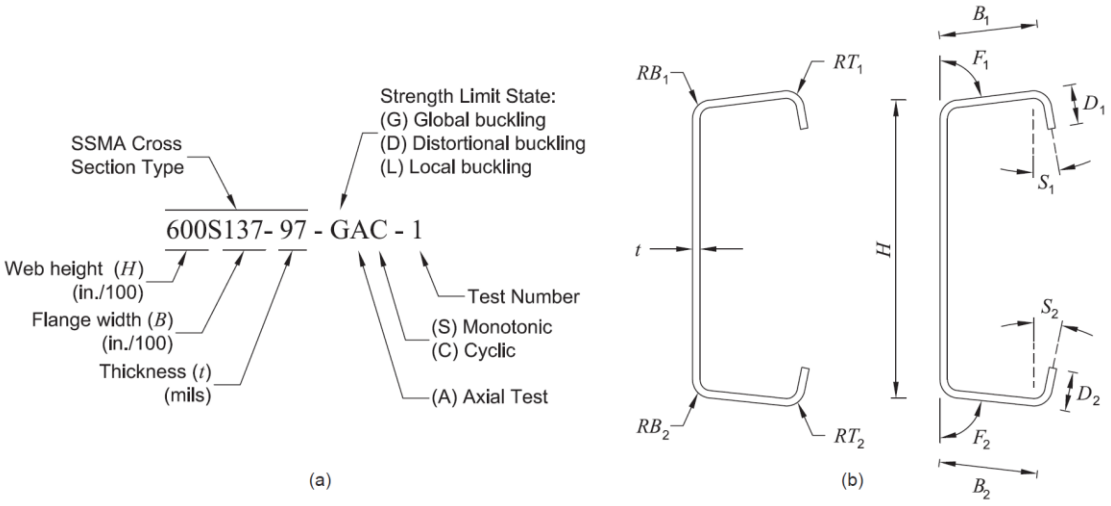

Fig. 4.1. Specimen naming notation (a); and cross-section dimension (b).

Table 4.2. Measured axial specimen dimensions.

Specimen	L	A_g	D_1	D_2	B_1	B_2	H	RT_1	RB_1	RT_2	RB_2	F_1	F_2	S_1	S_2	t
	(mm)	(mm^2)	(mm)	(mm)	(mm)	(mm)	(mm)	(mm)	(mm)	(mm)	(mm)	(°)	(°)	(°)	(°)	(mm)
600S137-97-GAM-1	2286	631	19.1	17.3	36.2	35.8	152.7	5.2	5.8	4.8	5.2	84.1	89.3	1.7	1.6	2.59
600S137-97-GAM-2	2286	632	19.1	17.5	36.1	35.7	152.2	5.0	6.0	4.8	5.2	83.8	87.9	1.6	1.9	2.60
600S137-97-GAC-1	2286	634	17.6	19.5	35.8	36.0	152.1	4.8	5.6	4.8	5.4	87.6	84.3	1.0	1.4	2.60
600S137-97-GAC-2	2286	629	17.6	18.9	35.6	35.9	152.5	4.8	5.2	5.2	6.0	87.6	85.1	3.1	2.0	2.58
362S137-68-GAM-1	2286	315	11.6	13.4	34.5	33.5	93.3	4.0	4.0	4.4	4.4	88.4	87.6	-2.5	4.8	1.82
362S137-68-GAM-2	2286	316	11.7	13.5	34.5	33.3	93.2	4.0	3.8	4.4	4.4	86.6	87.8	-3.5	3.6	1.82
362S137-68-GAC-1	2286	315	11.8	13.3	34.4	33.6	93.3	4.0	4.0	4.4	4.4	86.6	88.1	-2.0	3.4	1.82
362S137-68-GAC-2	2286	315	11.8	13.3	34.4	33.4	93.3	4.0	4.0	4.4	4.4	88.5	88.2	-2.5	4.1	1.82
600S137-68-DAM-1	610	416	10.9	11.5	34.8	33.8	152.7	4.0	3.6	4.4	4.2	90.5	88.6	-1.5	0.6	1.80
600S137-68-DAM-2	610	415	10.7	11.5	34.8	33.8	152.7	4.0	4.0	4.4	4.0	90.5	89.5	-1.4	-0.7	1.80
600S137-68-DAC-1	610	416	10.8	11.3	34.4	34.2	152.7	4.0	4.0	4.2	4.0	91.9	88.1	-1.1	5.0	1.80
600S137-68-DAC-2	610	415	10.5	11.9	34.9	33.8	152.5	4.0	4.0	4.4	4.2	89.9	89.6	-1.1	-0.1	1.80
362S137-68-DAM-1	610	318	11.9	13.4	34.8	33.5	94.0	4.0	4.0	4.4	4.4	88.8	86.9	-4.7	5.4	1.82
362S137-68-DAM-2	610	317	12.0	12.9	34.5	33.9	93.3	4.0	4.0	4.4	4.4	89.8	86.4	-2.0	4.2	1.82
362S137-68-DAC-1	610	313	11.5	13.2	34.5	33.5	93.2	4.0	4.0	4.4	4.4	87.6	88.1	-2.3	4.1	1.81
362S137-68-DAC-2	610	314	11.6	13.4	34.4	33.9	93.2	4.0	4.0	4.4	4.4	89.7	86.2	-2.1	4.0	1.81
600S162-33-LAM-1	305	215	12.9	13.6	42.1	41.7	149.9	3.6	4.2	3.4	4.4	84.4	90.7	5.2	1.6	0.86
600S162-33-LAM-2	305	215	13.0	13.5	42.0	41.5	150.3	3.6	4.0	3.6	4.4	88.1	91.9	2.0	-0.2	0.86
600S162-33-LAC-1	305	215	12.7	13.6	41.9	41.7	150.6	3.6	4.0	3.6	4.4	84.6	91.1	6.0	1.5	0.86
600S162-33-LAC-2	305	215	12.7	13.6	41.9	41.5	150.3	3.6	4.0	3.2	4.4	86.6	89.1	3.1	3.6	0.86
362S162-54-LAM-1	305	272	12.0	11.6	41.6	42.3	93.1	3.6	4.4	4.2	4.4	90.2	89.8	0.9	2.4	1.44
362S162-54-LAM-2	305	273	11.7	12.2	42.3	41.6	92.7	4.2	4.4	3.6	4.4	89.2	89.2	3.2	2.2	1.44
362S162-54-LAC-1	305	272	11.7	11.8	42.0	41.6	92.7	4.0	4.4	3.6	4.4	88.9	89.5	1.0	2.0	1.44
362S162-54-LAC-2	305	273	11.8	12.0	42.3	41.7	92.9	4.2	4.4	3.8	4.4	89.0	89.2	5.1	2.3	1.44
362S162-54-LAMT-1	305	272	11.8	12.3	41.1	42.2	92.8	3.6	4.2	4.0	4.2	92.4	88.8	-3.6	3.6	1.46
362S162-54-LAMT-2	305	274	11.7	12.2	41.3	42.3	93.9	3.6	4.4	4.2	4.3	90.1	88.1	1.4	3.9	1.46

See the dimension definitions in Fig. 2

Table 4.3. Elastic buckling properties and predicted compressive capacity.

Specimen	F_y (MPa)	F_u (MPa)	P_y (kN)	P_n (kN)	P_{cre} (kN)	λ_e	P_{crd} (kN)	λ_d	L_{crd} (mm)	$P_{crℓ}$ (kN)	$\lambda_ℓ$	$L_{crℓ}$ (mm)	δ_e ($\times 10^{-3}$mm)
600S137-97-GAM-1	388	529	245	121	147	1.29	228	1.04	314	198	0.78	119	654
600S137-97-GAM-2	394	529	249	122	147	1.30	232	1.04	314	201	0.78	118	653
600S137-97-GAC-1	382	523	242	121	147	1.28	233	1.02	318	202	0.78	118	650
600S137-97-GAC-2	388	528	244	120	145	1.30	225	1.04	315	196	0.78	119	647
362S137-68-GAM-1	392	531	123	60	71	1.32	165	0.86	253	130	0.68	71	636
362S137-68-GAM-2	387	529	122	59	70	1.32	167	0.86	252	131	0.67	71	624
362S137-68-GAC-1	389	535	123	59	70	1.32	166	0.86	254	130	0.67	71	626
362S137-68-GAC-2	386	529	121	60	71	1.30	165	0.86	254	130	0.68	71	638
600S137-68-DAM-1	427	558	177	91	1249	0.38	76	1.53	260	62	1.64	123	173
600S137-68-DAM-2	427	558	177	90	1243	0.38	75	1.53	258	62	1.64	124	172
600S137-68-DAC-1	427	558	177	91	1270	0.37	76	1.53	259	62	1.64	124	172
600S137-68-DAC-2	427	558	177	91	1256	0.38	76	1.53	259	62	1.64	123	173
362S137-68-DAM-1	389	529	124	103	968	0.36	180	0.83	256	130	0.95	72	533
362S137-68-DAM-2	389	529	123	103	961	0.36	180	0.83	255	132	0.94	71	537
362S137-68-DAC-1	389	528	122	101	933	0.36	175	0.83	252	128	0.95	71	529
362S137-68-DAC-2	389	528	122	102	947	0.36	177	0.83	254	128	0.95	71	531
600S162-33-LAM-1	333	398	72	27	4138	0.13	62	1.08	515	8	3.04	111	32
600S162-33-LAM-2	333	398	72	32	4307	0.13	53	1.16	462	11	2.49	108	48
600S162-33-LAC-1	333	398	72	27	4125	0.13	60	1.09	512	8	3.05	112	32
600S162-33-LAC-2	333	398	72	27	4147	0.13	60	1.09	511	8	3.05	111	32
362S162-54-LAM-1	416	476	113	81	3704	0.17	157	0.85	330	70	1.26	72	232
362S162-54-LAM-2	416	476	113	81	3674	0.18	160	0.84	333	71	1.26	71	234
362S162-54-LAC-1	416	476	113	81	3626	0.18	157	0.85	328	70	1.26	71	233
362S162-54-LAC-2	416	476	113	81	3683	0.18	158	0.85	332	70	1.26	72	232
362S162-54-LAMT-1	416	476	113	81	3717	0.17	161	0.84	334	70	1.26	71	233
362S162-54-LAMT-2	416	476	114	81	3720	0.17	159	0.85	332	69	1.27	72	228

$\lambda_e = (P_v/P_{cre})^{0.5}$; $\lambda_d = (P_v/P_{crd})^{0.5}$; $\lambda_ℓ = (P_{ne}/P_{crℓ})^{0.5}$.

4.3 Test setup and instrumentation

A loading frame was assembled to perform the cyclic tests (see Fig. 4.2). End plates were welded to both ends of the specimens to transfer axial forces while providing rotation fixed and longitudinal warping fixed end boundary conditions. The axial deformations were measured using two LVDTs connected between the top and bottom end plates as shown on the right of Fig. 4.2. The attachment of the LVDT fixtures to the end plate as close to the specimen as possible minimizes potential error associated with elastic end plate deformation (predicted to be non-negligible using finite element modeling for instances when the specimen is in tension). The specimens were subjected to a cyclic displacement history at a constant displacement rate of 0.008 (mm/min)/(mm of specimen length). Based on previous monotonic tension tests, it is expected that this displacement rate will produce strengths within an approximate range between 2% larger than the static value and 5% smaller than

expected earthquake displacement rates [30], while producing an average test time of 90 minutes. The displacement rate for the monotonic tests was 0.0001 (mm/min)/(mm of specimen length) which corresponds to the maximum rate of 21MPa per minute recommended in the AISI test method for column distortional buckling [31].

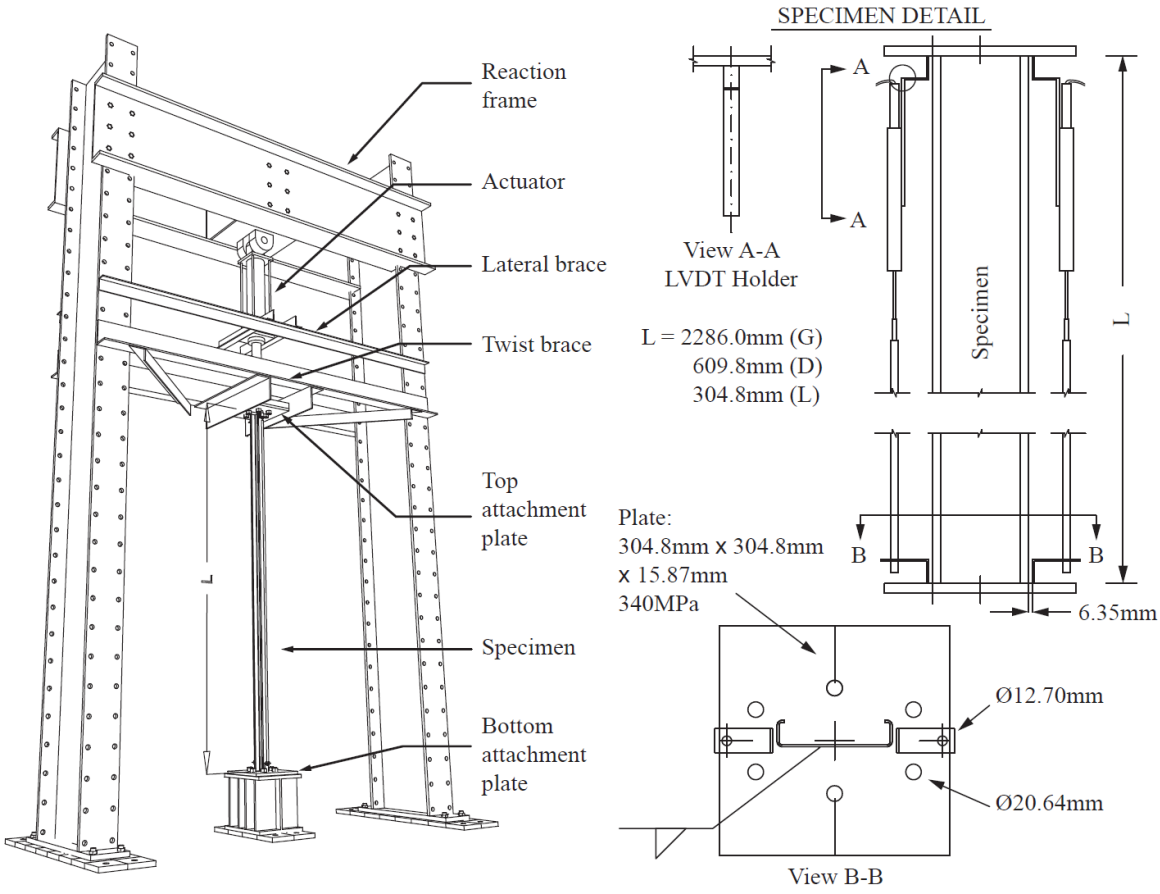

Fig. 4.2. Test setup and specimen detail.

4.4 Loading protocol

Cyclic loading protocols attempt to experimentally simulate deformation demands, cumulative deformation, and the number of inelastic cycles a system (or component) might endure during a design level seismic event [32]. The peak axial displacement demand, cumulative displacement demand, and number of inelastic cycles in a particular cold-formed steel member depends on many factors such as the location of the member in the building (end studs in a shear wall experience larger axial deformation demands than studs in a typical partition wall), end fixity/constraints (connections may not fully transfer tension,

compression, or moments to the member), the building's dynamic properties (elastic and nonlinear), and ground motion properties (which can vary depending source characteristics, distance to fault, site characteristics, etc.). Because of the inherent challenges associated with predicting demands on specific CFS members, the loading protocol adopted here (see Fig. 4.3) instead focuses on the progression of damage limit states in the member rather than reproducing seismic demands for a specific member configuration.

The loading protocol in Fig. 4.3 was adapted from the FEMA 461 quasi-static cyclic deformation-controlled testing protocol. The FEMA 461 protocol can be used obtain fragility data and hysteretic response characteristics of building components for which damage is best predicted by imposed deformations [33]. CFS axial members may experience asymmetrical loading because of different reasons such as the nature of the end connections (e.g. screwed or welded connection), and location within a building system (e.g. end stud compared to an inside stud in a shear wall). Using a symmetric protocol with equal deformation demands in compression and tension captures the damage and energy dissipation from cross-sectional deformation of the thin-walled channel sections under compression and damage and tearing that can occur by the reversal of these deformations under tension loading. Hysteretic models built based on the responses obtained from this protocol are expected to be capable of capturing the behavior under different loading patterns such as one-sided loading.

The FEMA 461 protocol is defined to reach a deformation associated with the most severe damage state at a preset point in the loading protocol, such as the 20^{th} cycle. It is also suggested that at least six cycles should be completed prior to reaching the lowest damage state [33]. For the CFS axial members considered herein, the lowest damage state is assumed to be the initiation of buckling deformations. Hence, linear elastic behavior is expected during the first six cycles.

The loading protocol use for this research consists of amplitude increasing steps with two cycles per step. Each step amplitude is related to the previous by the equation $\delta_i=1.4\delta_{i-1}$ (see Fig. 4.3). The anchor point is the elastic axial displacement, $\delta_e=P_eL/AE$, that defines the amplitude of the fourth step (i.e., 7^{th} and 8^{th} cycles). P_e is the compressive load at which buckling deformations are expected to initiate, hence, linear elastic behavior is expected during the first six cycles. P_e is calculated using slenderness limits defined in the AISI Direct

Strength Method (DSM) [25]. The DSM approach dictates that local buckling initiates at λ_ℓ=0.776 and the distortional buckling initiates at λ_d=0.561. Using $\lambda=(P_e/P_{cr})^{0.5}$, then P_e=0.60$P_{cr\ell}$ and P_e=0.31P_{crd}. The load that initiates global buckling deformation is assumed to be P_e=0.50P_{cre}. Values of δ_e are listed in Table 4.3 for all specimens.

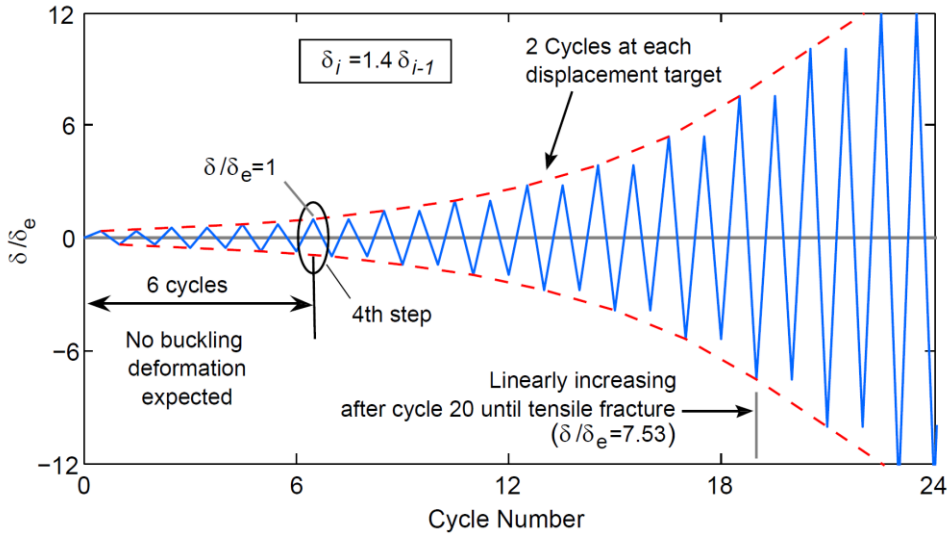

Fig. 4.3. Cyclic compression-tension cold-formed steel loading protocol.

4.5 Specimen imperfections

Initial imperfections of CFS members greatly affect their axial strength and initial stiffness in compression. Moreover, the predicted strength decreases the most if the imperfections resemble the governing buckling mode [27, 34, 35]. Member imperfections are defined as the specimen geometry deviations from the straight "perfect" member before attaching it to the loading frame (see Fig. 4.4). The "perfect" C-shaped member is straight, has a flat web surface and flat flanges perpendicular to the web as shown in Fig. 4.4.a. Imperfection measurements were measured using photogrammetry and conventional measuring methods. Between 750 and 1800 (depending on specimen length) targets were attached to the member web and flanges for the photogrammetry methods (see Fig. 4.5b). The spatial coordinates of every target were then processed using PhotoModeler® [36] to estimate the specimen initial imperfections and geometry. The conventional measuring method is used to validate measurements from the photogrammetry method. The conventional method uses the distance from a reference plane to selected points of the cross-

section along the length of the specimen (see Fig. 4.5a). Both methods use the same procedure to quantify and characterize imperfections briefly described below.

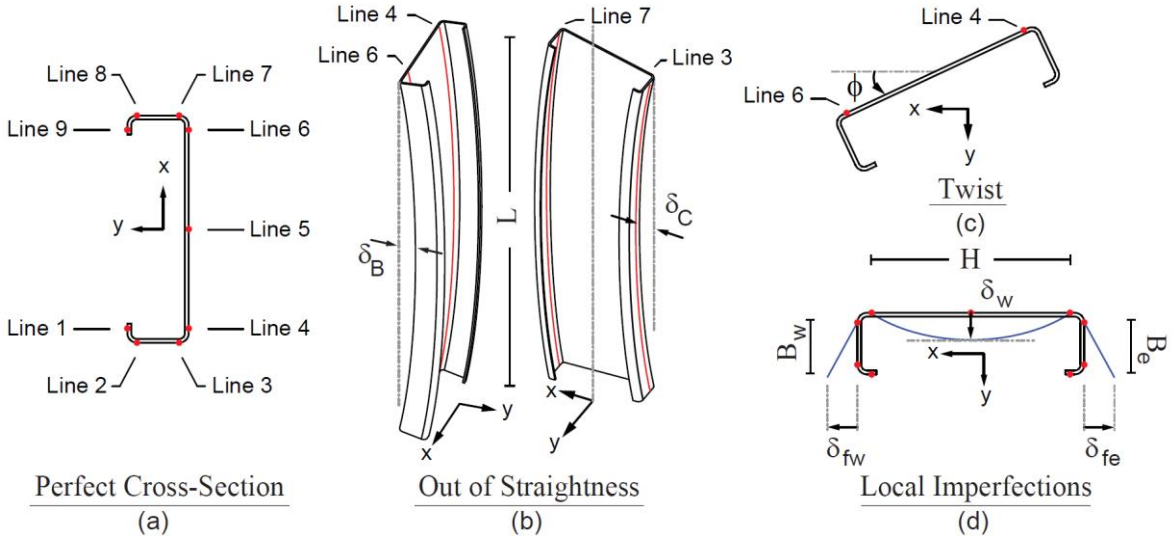

Fig. 4.4. Global and local imperfection definition.

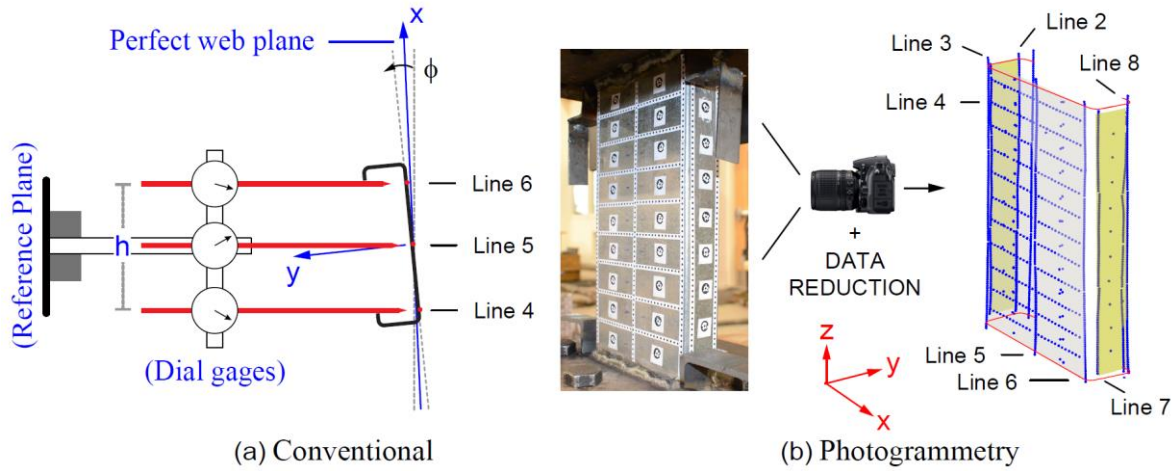

Fig. 4.5. Imperfection measurement methods.

The procedure for characterizing initial imperfections requires defining the shape of the perfect C-shaped member. The web is defined by the plane that best fits the points on line 4 and 6. This plane serves as the reference for all the imperfection measurements and the y-axis is set normal to this plane (see Fig. 4.4a, d). Two planes perpendicular to the web plane and separated the measured width of the cross-section are used to describe the flanges of the perfect C-section. The out of straightness in the weak axis direction δ_B, in both methods is

the average perpendicular distance of points in lines 4 and 6 to the plane that describes the web of a perfect C-section. The out of straightness in the strong axis direction δ_C, is the average perpendicular distance of line 3 and 7 to the respective planes that describes the flanges of the perfect C-section. Out of straightness in the strong axis direction is only available in the photogrammetry method. The overall twist, ϕ, of the cross-section at a certain height is the angle that a line going from a point in line 4 to a point in line 6 forms with the plane of the perfect web (see Fig. 4.4c). The web imperfection δ_w is estimated as the perpendicular distance of a point in line 5 to the line going from a point in line 4 to a point in line 6. The imperfection of the flanges in the conventional method is derived from the cross-section dimensions listed in Table 4.2. In the photogrammetry method the flange imperfections δ_{fe} and δ_{fw} are computed as the perpendicular distance of points in lines 2 and 8 to the plane of the perfect flanges.

Imperfections were measured for all the specimens using the conventional method, and for nine specimens using the photogrammetry method. Fig. 4.6 and Fig. 4.7 compare the global and local imperfections measured using both methods for specimen 362S137-68-DAM-2. Comparison of the two methods shows that using photogrammetry it is possible to accurately capture the imperfections as defined for conventional methods in [27, 35]. Using photogrammetry allowed a greater discretization of the geometry and permitted to capture the flange geometry close to the end plates where it was not possible to obtain measurements using the conventional method (see Fig. 4.7).

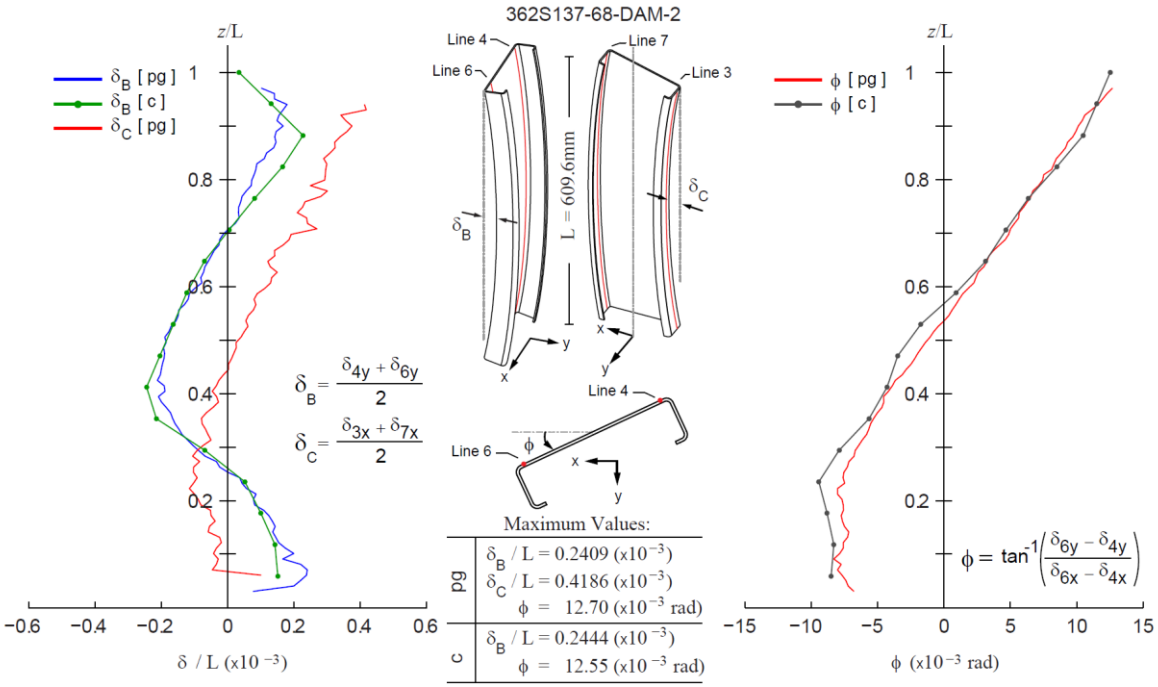

Fig. 4.6. Global imperfections for specimen 362S137-68-DAM-2.
(pg = photogrammetry, c = conventional)

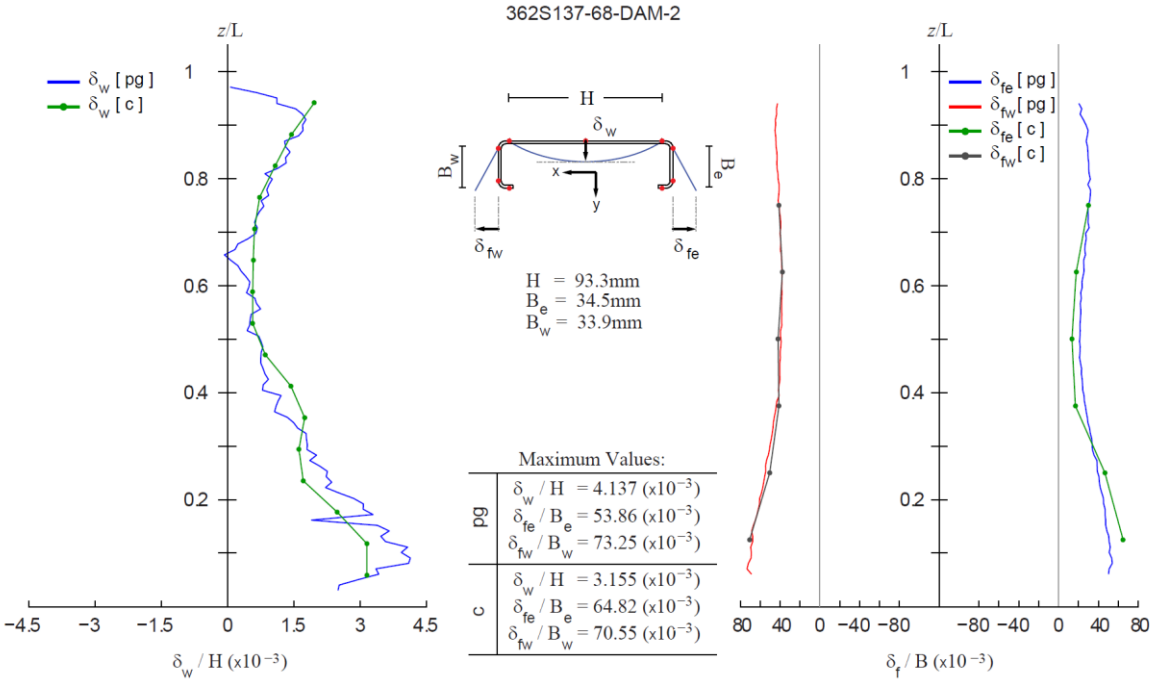

Fig. 4.7. Global imperfections for specimen 362S137-68-DAM-2.
(pg = photogrammetry, c = conventional)

The average maximum measured imperfections were generally smaller than the tolerance limits given in ASTM C955-09 [32] as shown in Table 4.4 and Table 4.5. However, for some specimens the global imperfections where larger than the ASTM limit and affected their strength. For instance, the maximum value for $\delta_B/L=2.21$ in Table 4.4 corresponds to specimen 600S137-97-GAM-2, which strength was reduced about 27% from the predicted strength (see Table 4.7 and Fig. 4.10b). Large initial global imperfections also affected the buckling mode. For example specimen 362S137-68-GAM-1 had the larger initial twist, which led to flexural-torsional buckling. The out of straightness in the strong axis direction δ_C for the local buckling members was in average larger than the ASTM limits; however, its effect on the compressive strength and buckling mode is negligible (see 4.6.2). Local imperfections were all lower than the ASTM limits, and smaller than the 75% and 95% percentile values $\delta_w/t = 0.66$ and $\delta_f/t = 3.44$ respectively suggested for typical members in [38]. Local imperfections are not expected to adversely influence the compressive strength or initial stiffness.

Table 4.4. Maximum imperfections using conventional method.

		Imperfections conventional method				
		δ_B/L ($\times10^{-3}$)	**ϕ** (°)	**δ_W/H** ($\times10^{-3}$)	**δ_{FE}/B_e** ($\times10^{-3}$)	**δ_{FW}/B_w** ($\times10^{-3}$)
Global	Mean	1.04 (L/961)	2.64	8.16 (H/123)	48.16 (B/21)	46.27 (B/22)
	Max	2.21 (L/452)	3.93	44.45 (H/22)	76.40 (B/13)	86.99 (B/11)
	Min	0.22 (L/4556)	1.66	1.67 (H/598)	19.14 (B/52)	26.91 (B/37)
	St.Dev	0.70	0.78	14.69	18.65	21.49
	COV	0.68	0.29	1.80	0.39	0.46
Distortional	Mean	0.60 (L/1678)	1.39	3.25 (H/308)	41.50 (B/24)	28.25 (B/35)
	Max	0.97 (L/1028)	3.48	6.14 (H/163)	54.10 (B/18)	51.22 (B/20)
	Min	0.23 (L/4389)	0.10	0.81 (H/1231)	14.58 (B/69)	9.68 (B/103)
	St.Dev	0.23	1.13	1.95	12.77	13.40
	COV	0.38	0.81	0.60	0.31	0.47
Local	Mean	0.46 (L/2187)	0.77	3.74 (H/267)	43.87 (B/23)	37.57 (B/27)
	Max	0.78 (L/1277)	2.16	10.58 (H/95)	79.92 (B/13)	51.46 (B/19)
	Min	0.20 (L/5080)	0.02	1.66 (H/604)	12.24 (B/82)	22.45 (B/45)
	St.Dev	0.20	0.71	2.87	23.98	12.50
	COV	0.44	0.92	0.77	0.55	0.33
ASTM C955 Tol.		L/960	-	2 x 1.59mm (max)	2 x 1.59mm (max)	2 x 1.59mm (max)

Table 4.5. Maximum imperfections using photogrammetry method.

		Imperfections photogrammetry method					
		δ_B/L ($\times10^{-3}$)	δ_C/L ($\times10^{-3}$)	ϕ (°)	δ_W/H ($\times10^{-3}$)	δ_{FE}/B_e ($\times10^{-3}$)	δ_{FW}/B_w ($\times10^{-3}$)
Distortional	Mean	0.73 (L/1361)	0.56 (L/1771)	1.57	3.86 (H/259)	34.90 (B/29)	35.97 (B/28)
	Max	1.37 (L/732)	0.95 (L/1052)	2.69	6.68 (H/150)	38.84 (B/26)	53.90 (B/19)
	Min	0.45 (L/2211)	0.30 (L/3288)	0.21	1.47 (H/681)	33.44 (B/30)	19.40 (B/52)
	St.Dev	0.43	0.27	1.10	2.19	2.64	14.11
	COV	0.58	0.49	0.70	0.57	0.08	0.39
Local	Mean	0.63 (L/1596)	1.63 (L/612)	1.32	9.45 (H/106)	38.62 (B/26)	45.65 (B/22)
	Max	0.99 (L/1015)	3.22 (L/311)	2.77	13.10 (H/76)	41.61 (B/24)	52.66 (B/19)
	Min	0.14 (L/7262)	0.80 (L/1252)	0.16	7.91 (H/126)	32.21 (B/31)	36.26 (B/28)
	St.Dev	0.36	1.09	1.12	2.48	4.32	6.93
	COV	0.57	0.67	0.85	0.26	0.11	0.15
ASTM C955 Tol.		L/960	L/960	-	2 x 1.59mm (max)	2 x 1.59mm (max)	2 x 1.59mm (max)

Measurements from the photogrammetry method were used to characterize the specimen initial geometry as a combination of trigonometric functions that describe imperfection magnitudes superposed to the geometry of a perfect C-shaped cross-section. This type of characterization makes it possible to represent the initial geometry with a limited set of variables as opposed to a large 3D point cloud. The initial geometry can then be accurately simulated in finite element analysis or other calculations for comparison with experimental results. The initial imperfection including imperfections can be reconstructed by modifying the geometry of the perfect cross-section in Fig. 4.8a such that the coordinates of points 2 through 8 match the measured imperfections δ_B, δ_C, ϕ, δ_w, δ_{fe}, and δ_{fw}. For local web imperfections for example, the geometry is modified such that the out-of-plane deformation at any point along line 5 (i.e., P_5 in Fig. 4.8a) is equal to δ_w. The geometry of the imperfect cross-section is derived by applying first the local deformations δ_w, δ_{fe}, and δ_{fw} to the points in the perfect cross section as depicted in Fig. 4.8b. The resulting geometry is the further modified by applying the global imperfections ϕ, δ_B, δ_C (see Fig. 4.8c). The procedure to derive the imperfect cross-section geometry in Fig. 4.8 can be used to reconstruct the imperfections for any cross-section along the member. To provide a continuum along the length of the members, a sine-wave series (Eq. 4.1) consisting of four terms plus a linear term was fit to each of the measured imperfection $\delta_i(z)$ using a least squares approach.

$$\delta_i(z) = (mz + b) + \sum_{k=1}^{4} C_k \sin\left(\frac{\pi}{L_k} z + \varphi_k\right) \qquad 4.1$$

The linear term '$mz + b$' was subtracted from the data before fitting sine-wave series in Eq. (4.1). Removal of the linear term is essential to obtain coefficients L_k comparable to the half wavelength values predicted in Table 3. The fitted parameters are listed in are listed in Table 6. Comparing the fitted half-wavelengths L_k in Table 6 to the respective L_{crd} and $L_{cr\ell}$ values from Table 4.3, one can see that not always the longest half-wavelength L_1 corresponds to the predicted half-wavelengths. However, the terms with the highest amplitudes C_k generally correspond to L_k values that are close to the predicted L_{cr}. Using the values in Table 4.6, and Eq. 4.1, the geometry of the cross-section including imperfections can be reconstructed.

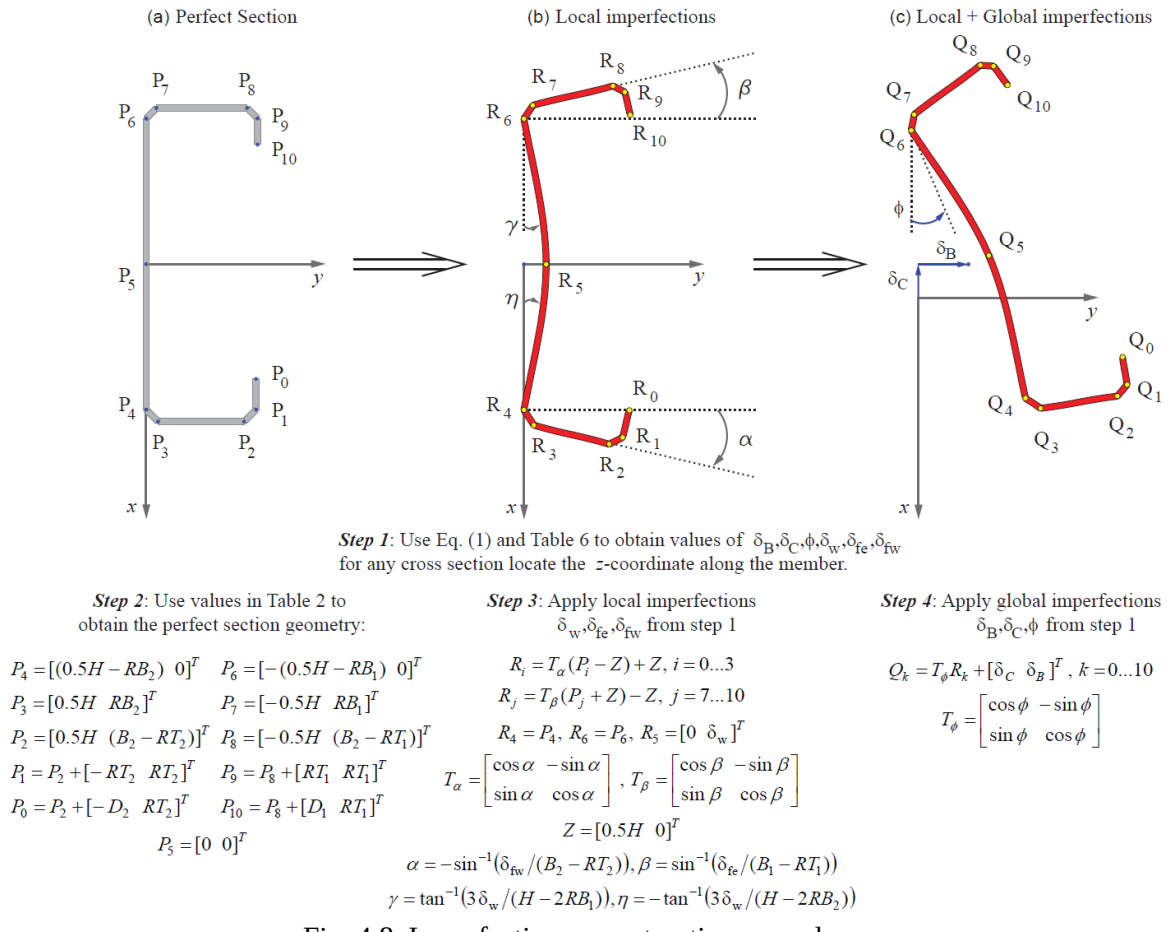

Fig. 4.8. Imperfection reconstruction procedure.

Table 4.6. Imperfection fitted coefficients.

		L_1	L_2	L_3	L_4	C_1	C_2	C_3	C_4	φ_1	φ_2	φ_3	φ_4	m	b	R^2	$adjR^2$	SSE	$RMSE$
		(mm)				(mm) or (°)				(rad)				(mm/mm) or (°/mm)	(mm) or (°)				
362S137-68-DAC-2	δ_B	251.9	172.3	130.7	95.9	0.403	0.255	0.103	0.026	0.932	1.945	3.141	3.142	-1.75E-05	0.00	1.000	1.000	1.30E-03	3.90E-03
	δ_C	225.1	154.5	108.1	92.2	0.092	0.067	0.030	0.010	0.481	1.380	1.766	3.141	6.89E-05	-0.03	0.999	0.999	1.94E-04	1.60E-03
	ϕ	279.0	74.9	96.6	61.5	0.073	0.011	0.011	0.010	-1.807	3.142	-2.893	3.142	4.50E-03	-1.39	0.956	0.950	1.70E-02	1.44E-02
	δ_w	291.5	572.3	73.2	90.8	0.119	0.027	0.007	0.005	1.289	-1.207	-1.263	0.616	-1.18E-04	0.15	0.999	0.999	5.78E-04	2.70E-03
	δ_{fe}	265.1	112.6	98.6	133.4	0.281	0.062	0.041	0.032	-2.049	-0.312	0.957	-2.077	1.70E-03	-1.77	1.000	1.000	1.10E-03	3.80E-03
	δ_{fw}	175.8	132.6	221.7	98.8	0.258	0.122	0.075	0.029	0.976	2.041	-0.431	3.141	2.60E-03	0.37	0.999	0.999	9.33E-04	3.50E-03
362S137-68-DAM-2	δ_B	286.6	59.8	58.8	152.2	0.113	0.022	0.021	0.020	1.480	-0.570	2.197	0.097	8.70E-06	0.00	1.000	0.999	3.41E-04	2.00E-03
	δ_C	244.5	176.6	97.3	65.1	0.063	0.035	0.004	0.003	0.919	2.198	-0.126	-1.997	5.55E-04	-0.12	0.999	0.999	9.23E-05	1.10E-03
	ϕ	251.2	165.5	118.1	96.0	0.118	0.084	0.029	0.008	1.078	1.590	2.138	3.141	2.20E-03	-0.69	0.999	0.999	4.46E-04	2.30E-03
	δ_w	287.2	609.5	142.2	95.7	0.099	0.021	0.011	0.006	1.150	-1.280	0.822	-2.249	-4.16E-04	0.26	0.997	0.997	1.20E-03	3.80E-03
	δ_{fe}	287.9	175.4	103.0	76.4	0.261	0.119	0.026	0.020	-1.724	3.142	3.142	3.142	1.50E-03	-1.53	0.998	0.997	1.11E-02	1.19E-02
	δ_{fw}	246.8	163.9	117.3	93.5	0.396	0.158	0.049	0.020	0.838	1.756	2.463	3.142	-1.70E-03	2.11	1.000	1.000	9.04E-04	3.40E-03
362S137-68-GAC-2	δ_B	1016.7	584.6	379.6	290.9	0.190	0.127	0.056	0.041	0.935	3.142	3.142	3.142	-2.23E-05	0.01	0.965	0.963	1.94E-01	3.30E-02
	δ_C	756.5	567.4	463.3	194.6	0.324	0.226	0.056	0.010	-0.465	0.883	2.445	2.039	1.18E-04	-0.12	0.998	0.997	7.40E-03	7.10E-03
	ϕ	993.8	622.5	386.5	292.9	0.477	0.090	0.065	0.044	1.071	3.142	3.142	3.142	-1.20E-04	0.11	0.992	0.992	1.66E-01	3.07E-02
	δ_w	1028.7	359.2	453.4	308.2	0.078	0.078	0.061	0.046	-1.947	-1.811	-3.142	0.182	-2.97E-05	-0.06	0.986	0.985	1.54E-02	9.40E-03
	δ_{fe}	916.1	436.0	246.1	72.1	0.225	0.118	0.088	0.001	0.555	-3.142	-0.410	-3.142	2.90E-04	-1.19	0.995	0.995	2.55E-02	1.33E-02
	δ_{fw}	311.6	683.1	254.1	482.0	0.077	0.077	0.042	0.036	1.832	1.483	1.778	-3.140	-3.86E-05	1.45	0.960	0.957	2.60E-02	1.34E-02
362S162-54-LAC-1	δ_B	133.2	63.7	44.8	35.0	0.031	0.018	0.010	0.003	-1.547	2.163	3.142	3.142	-7.41E-04	0.07	0.991	0.989	2.41E-04	2.70E-03
	δ_C	105.4	87.2	38.5	23.3	0.059	0.026	0.004	0.003	0.277	2.020	3.136	2.140	2.20E-03	-0.36	0.993	0.990	2.12E-04	2.90E-03
	ϕ	125.0	64.3	43.7	262.0	0.019	0.006	0.004	0.004	1.039	-1.395	-0.959	3.142	1.08E-02	-1.66	0.990	0.987	1.06E-04	1.80E-03
	δ_w	111.3	69.6	33.1	29.5	0.038	0.028	0.011	0.008	-2.176	-1.972	1.787	3.142	2.50E-03	-0.15	0.949	0.931	2.30E-03	8.70E-03
	δ_{fe}	94.1	68.9	55.3	25.7	0.177	0.166	0.051	0.006	-0.216	0.978	2.532	0.490	-6.00E-03	0.16	0.997	0.995	6.27E-04	5.00E-03
	δ_{fw}	112.0	52.5	27.6	19.7	0.095	0.024	0.020	0.012	-2.600	2.138	0.507	1.340	1.02E-02	-1.00	0.978	0.970	5.30E-03	1.43E-02
362S162-54-LAM-2	δ_B	42.5	37.3	69.8	28.7	0.008	0.008	0.004	0.002	-3.009	-1.347	3.082	3.099	-2.89E-05	0.01	0.949	0.932	6.72E-05	1.40E-03
	δ_C	99.6	162.9	61.7	25.6	0.019	0.010	0.004	0.002	1.618	-0.677	2.179	1.077	-6.98E-04	0.13	0.983	0.975	6.20E-05	1.60E-03
	ϕ	138.0	47.0	38.5	24.0	0.029	0.016	0.010	0.005	-1.580	2.645	3.142	2.070	-5.51E-04	0.08	0.963	0.952	9.27E-04	5.30E-03
	δ_w	108.3	190.1	71.2	43.1	0.097	0.046	0.038	0.019	1.703	0.872	3.078	0.025	3.30E-03	-0.39	0.997	0.996	2.49E-04	2.80E-03
	δ_{fe}	109.9	122.7	51.6	42.4	0.098	0.060	0.033	0.021	-3.142	-2.107	1.775	3.065	-7.00E-03	0.78	0.999	0.999	4.32E-04	4.20E-03
	δ_{fw}	96.3	66.2	50.3	37.2	0.316	0.204	0.065	0.011	-0.244	0.838	2.038	2.789	8.90E-03	-1.01	1.000	1.000	1.74E-04	2.70E-03
600S137-68-DAC-2	δ_B	289.7	158.1	608.2	118.7	0.180	0.063	0.036	0.007	1.578	1.776	0.769	3.141	3.75E-05	-0.01	1.000	0.999	6.19E-04	2.80E-03
	δ_C	248.6	124.2	464.6	82.8	0.066	0.024	0.005	0.003	-1.926	0.680	-1.533	2.036	1.66E-04	-0.01	0.999	0.999	1.54E-04	1.50E-03
	ϕ	281.2	98.7	135.3	80.9	0.041	0.016	0.007	0.007	-1.823	-1.999	3.142	-1.469	-1.69E-04	0.06	0.997	0.997	2.49E-04	1.80E-03
	δ_w	256.4	184.4	100.1	60.3	0.176	0.078	0.015	0.011	0.887	3.142	3.142	2.753	-2.00E-03	1.01	0.987	0.985	1.30E-02	1.27E-02
	δ_{fe}	117.9	253.5	85.7	51.4	0.074	0.074	0.054	0.015	-3.085	-2.034	3.142	1.843	2.30E-03	-0.77	0.975	0.972	1.57E-02	1.47E-02
	δ_{fw}	203.9	149.2	106.6	90.8	0.231	0.206	0.102	0.023	0.520	1.097	1.720	3.141	-2.80E-03	1.43	0.998	0.998	2.80E-03	6.30E-03
600S137-68-DAM-2	δ_B	272.8	180.0	63.4	98.6	0.102	0.034	0.002	0.002	1.177	1.556	0.857	-3.141	5.66E-05	-0.02	0.999	0.999	3.60E-04	2.10E-03
	δ_C	265.1	123.3	64.9	51.8	0.054	0.017	0.006	0.004	-2.188	-3.086	-3.142	1.614	-1.10E-03	0.40	0.983	0.981	3.20E-03	6.60E-03
	ϕ	267.6	165.6	117.6	95.6	0.131	0.077	0.034	0.013	0.986	1.581	2.140	3.142	-3.80E-03	1.15	1.000	1.000	1.68E-04	1.40E-03
	δ_w	146.0	101.9	237.7	84.7	0.036	0.036	0.020	0.016	-2.073	-2.283	-2.412	-1.107	1.07E-04	-0.04	0.987	0.986	9.05E-04	3.30E-03
	δ_{fe}	259.1	88.5	122.7	72.6	0.147	0.067	0.059	0.040	-2.110	2.880	-3.142	3.142	1.60E-03	-0.42	0.990	0.989	1.40E-02	1.35E-02
	δ_{fw}	143.1	111.8	190.8	97.9	0.374	0.250	0.232	0.115	0.754	1.564	-0.280	3.142	4.68E-04	0.21	0.997	0.997	3.20E-03	6.60E-03
600S162-33-LAC-2	δ_B	98.8	94.5	32.6	30.0	0.156	0.136	0.040	0.038	-0.110	3.142	1.045	3.142	-3.80E-04	0.07	0.924	0.904	7.40E-03	1.48E-02
	δ_C	62.1	94.1	45.5	37.7	0.080	0.069	0.052	0.020	2.703	-3.142	2.377	3.141	-3.18E-05	-0.05	0.994	0.991	7.93E-04	5.50E-03
	ϕ	115.2	75.9	46.9	36.6	0.088	0.055	0.025	0.010	-2.130	-1.815	2.949	3.142	2.00E-03	-0.30	0.968	0.957	7.40E-03	1.52E-02
	δ_w	120.3	62.5	44.3	34.8	0.170	0.104	0.099	0.051	-2.091	-3.142	3.142	3.142	3.70E-03	-0.68	0.976	0.971	2.88E-02	2.87E-02
	δ_{fe}	111.1	37.7	44.9	32.7	0.203	0.202	0.149	0.093	-2.641	1.259	0.200	2.351	-8.00E-03	-0.26	0.989	0.985	1.43E-02	2.34E-02
	δ_{fw}	80.3	59.0	158.8	32.8	0.168	0.099	0.073	0.050	1.664	2.544	-1.136	3.142	8.80E-03	-0.82	0.997	0.996	2.00E-03	8.80E-03
600S162-33-LAM-2	δ_B	74.1	57.0	131.8	114.0	0.028	0.019	0.019	0.011	-1.945	-0.755	-0.130	-2.932	3.78E-04	-0.04	0.984	0.979	1.85E-04	2.40E-03
	δ_C	66.1	49.1	89.0	25.5	0.032	0.016	0.011	0.004	2.451	3.142	0.193	-0.033	4.10E-03	-0.77	0.974	0.963	4.07E-04	4.00E-03
	ϕ	128.5	74.4	51.1	37.3	0.021	0.016	0.006	0.004	0.622	3.140	2.437	3.141	5.50E-03	-0.84	0.985	0.980	2.89E-04	3.00E-03
	δ_w	127.8	64.7	46.7	37.7	0.276	0.275	0.190	0.098	-1.992	-3.022	3.142	3.142	-3.30E-03	-0.88	0.975	0.970	1.06E-01	5.51E-02
	δ_{fe}	40.9	100.6	54.5	31.0	0.066	0.066	0.066	0.034	3.095	-3.142	2.339	3.142	-6.80E-03	-0.36	0.918	0.888	2.11E-02	2.79E-02
	δ_{fw}	95.8	71.7	54.3	38.6	0.565	0.436	0.159	0.007	-0.343	1.400	2.460	1.572	-5.70E-03	0.16	0.999	0.999	1.30E-03	7.00E-03

4.6 Cyclic and Monotonic Axial Responses

Cyclic and monotonic load-deformation responses were obtained for specimens experiencing local, distortional, and global buckling limit states. From the monotonic tests, the average ratio of test peak load (in compression) to predicted load P_{min}/P_n was 1.00 with a coefficient of variation of 0.09 (see Table 4.7 and Table 4.8). This result shows that the actual boundary conditions accurately represent the assumed constraints of rotational fixity and warping fixity at the specimen ends. The cyclic response is linear during the first six cycles with equal stiffness in tension and compression for all specimens (see Fig. 4.9a, Fig. 4.11a, and Fig. 4.13a). As expected, the cyclic response is asymmetric due to the presence of buckling deformations in compression. Strength and stiffness in compression are sensitive to imperfections and cross-section deformations, and they degraded under cycling loading due to inelastic deformations. Additional details for each of the limit states are discussed below and test videos are available on Virginia Tech's digital repository [39].

Table 4.7. Test maximum loads.

Specimen	P_{max} (kN)	δ_{Pmax} ($\times10^{-3}$mm)	P_{min} (kN)	δ_{Pmin} ($\times10^{-3}$mm)	δ_y ($\times10^{-3}$mm)	P_{max}/P_y	P_{min}/P_n	δ_{Pmax}/L ($\times10^{-3}$)	δ_{Pmin}/L ($\times10^{-3}$)	δ_{Pmax}/δ_y	δ_{Pmin}/δ_y
600S137-97-GAM-1	-	-	-117	-2413	4358	-	0.97	-	-1.06	-	-0.55
600S137-97-GAM-2	-	-	-101	-2921	4424	-	0.83	-	-1.28	-	-0.66
600S137-97-GAC-1	236	8890	-129	-2362	4289	0.98	1.06	3.89	-1.03	2.07	-0.55
600S137-97-GAC-2	237	16180	-127	-2388	4361	0.97	1.06	7.08	-1.04	3.71	-0.55
362S137-68-GAM-1	-	-	-56	-2718	4400	-	0.94	-	-1.19	-	-0.62
362S137-68-GAM-2	-	-	-53	-2362	4355	-	0.90	-	-1.03	-	-0.54
362S137-68-GAC-1	122	8331	-50	-2464	4376	1.00	0.84	3.64	-1.08	1.90	-0.56
362S137-68-GAC-2	123	9068	-49	-2261	4339	1.01	0.83	3.97	-0.99	2.09	-0.52
600S137-68-DAM-1	-	-	-97	-1829	1277	-	1.07	-	-3.00	-	-1.43
600S137-68-DAM-2	-	-	-97	-1626	1279	-	1.08	-	-2.67	-	-1.27
600S137-68-DAC-1	175	3226	-96	-1295	1279	0.99	1.06	5.29	-2.13	2.52	-1.01
600S137-68-DAC-2	174	2769	-100	-1118	1278	0.98	1.10	4.54	-1.83	2.17	-0.87
362S137-68-DAM-1	-	-	-100	-1778	1166	-	0.96	-	-2.92	-	-1.52
362S137-68-DAM-2	-	-	-98	-1499	1166	-	0.95	-	-2.46	-	-1.28
362S137-68-DAC-1	127	5512	-99	-1168	1167	1.05	0.98	9.04	-1.92	4.72	-1.00
362S137-68-DAC-2	128	5766	-96	-991	1167	1.05	0.94	9.46	-1.63	4.94	-0.85
600S162-33-LAM-1	-	-	-31	-406	499	-	1.12	-	-1.33	-	-0.82
600S162-33-LAM-2	-	-	-33	-559	499	-	1.04	-	-1.83	-	-1.12
600S162-33-LAC-1	66	838	-29	-457	499	0.92	1.06	2.75	-1.50	1.68	-0.92
600S162-33-LAC-2	67	991	-32	-457	499	0.94	1.19	3.25	-1.50	1.99	-0.92
362S162-54-LAM-1	-	-	-88	-813	623	-	1.08	-	-2.67	-	-1.31
362S162-54-LAM-2	-	-	-86	-889	623	-	1.05	-	-2.92	-	-1.43
362S162-54-LAC-1	109	1295	-88	-508	623	0.97	1.08	4.25	-1.67	2.08	-0.82
362S162-54-LAC-2	110	1270	-90	-635	623	0.97	1.11	4.17	-2.08	2.04	-1.02
362S162-54-LAMT-1	110	1719	-	-	623	0.97	-	5.64	-	2.76	-
362S162-54-LAMT-2	115	9896	-	-	623	1.01	-	32.47	-	15.89	-

P_{max}, δ_{Pmax} = test max. tension and corresponding displacement; P_{min}, δ_{Pmin} = test max. compression and corresponding displacement

$\delta_y = P_y L/EA_g$ the elastic yielding displacement.

Table 4.8. Test-to-predicted statistics.

Specimen Group	P_{max}/P_y		P_{min}/P_n		δ_{Pmax}/L		δ_{Pmin}/L		δ_{Pmax}/δ_y		δ_{Pmin}/δ_y	
	μ	cov	μ	cov	μ	cov	μ	cov	μ	cov	μ	cov
Global	0.99	0.02	0.93	0.10	4.64	0.35	1.09	0.09	2.44	0.35	0.57	0.08
Distortional	1.02	0.03	1.02	0.07	7.08	0.36	2.32	0.22	3.59	0.40	1.16	0.22
Local	0.95	0.02	1.09	0.04	3.60	0.20	1.94	0.30	1.95	0.09	1.04	0.22
Monotonic	-	-	1.00	0.09	-	-	2.03	0.40	-	-	1.05	0.36
Cyclic	0.99	0.04	1.03	0.11	5.11	0.43	1.53	0.27	2.66	0.43	0.80	0.25
All Spec.	0.99	0.04	1.01	0.10	5.11	0.43	1.78	0.38	2.66	0.43	0.92	0.35

μ = mean value; cov = coefficient of variation.

Tension tests are not included

4.6.1 Global buckling limit state

The response of the cyclic global buckling (GAC) specimens was characterized by weak-axis flexural buckling which in later cycles led to folding of the stiffening lips near the mid-height as shown in Fig. 4.9d. Damage due to reversal of the strains accumulated at the mid-height folded lips as subsequent excursions in tension and compression took place. Strength in compression degraded rapidly in the cycles after the peak compressive load was reached due to the damaged accumulated at the folded lips. These deterioration is evidenced by the difference between the monotonic curves and the compression side of the cyclic responses in Fig. 4.10. Unloading stiffness also deteriorated during cyclic loading and the member unloaded nonlinearly from the compression side as shown in Fig. 4.9b. Web inelastic buckling occurred near the supports after significant damage accumulated at the mid-height folded lips. Excursions in tension after peak compressive load is reached are characterized by very low stiffness until the member straightens out as shown in Fig. 4.9b. Ductile yielding at a consistent tension yield capacity was observed at the mid-height cross-section as shown in bottom-left quadrant of Fig. 4.9c. The final failure mode was gradual tearing of the section starting at the folded lips and propagating through the cross section, or in some cases fracture near the welded connection.

The monotonic responses of the global buckling (GAM) specimens were generally characterized by weak axis flexural buckling, with folding of the stiffening lips at mid-height. Specimen 362S137-68-GAM-1 however, exhibited flexural-torsional buckling due to torsional initial imperfections in the member. The maximum twist of 3.93° in this member was the highest among all specimens (see Table 4.4). This resulted in a higher peak

compression load and higher monotonic envelope as shown in Fig. 4.10a, and Table 4.7. The peak compression load of specimen 600S137-97-GAM-2 was reduced by 17% compared to the others due to large initial global imperfections (δ_B=L/452, see Table 4.4) in the weak axis direction (Fig. 4.10b).

Imperfections influence the global buckling mode, initial stiffness, and the peak compression strength under monotonic loading. This influence is negligible for members under cyclic loading because during the first elastic tension excursions the imperfections straighten out. The result is equal initial stiffness in compression and tension (see Fig. 4.9a), and close to predicted strength values.

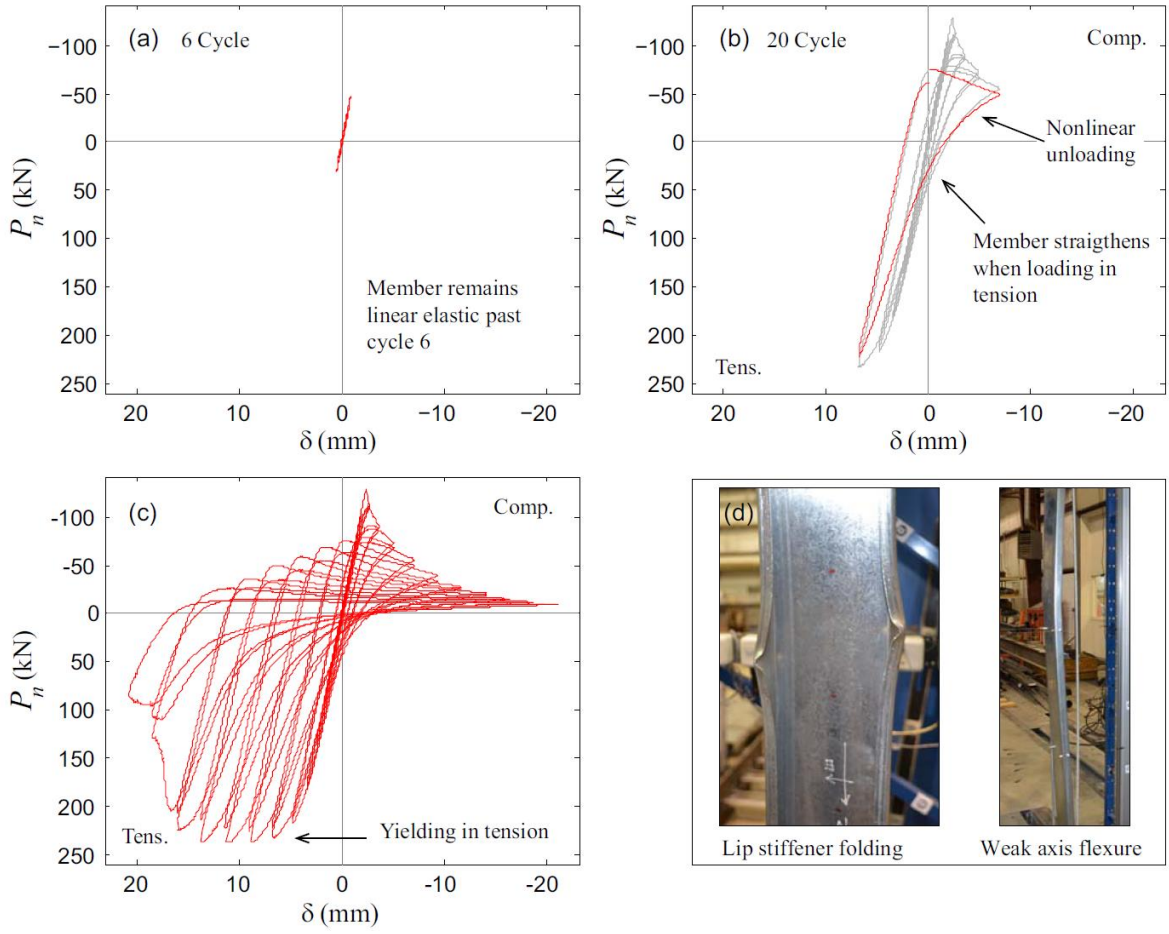

Fig. 4.9. Cyclic load-deformation response specimen 600S137-97-GAC-1,
(a) 6 cycles, (b) 20 cycles, (c) complete response, (d) failure mode.

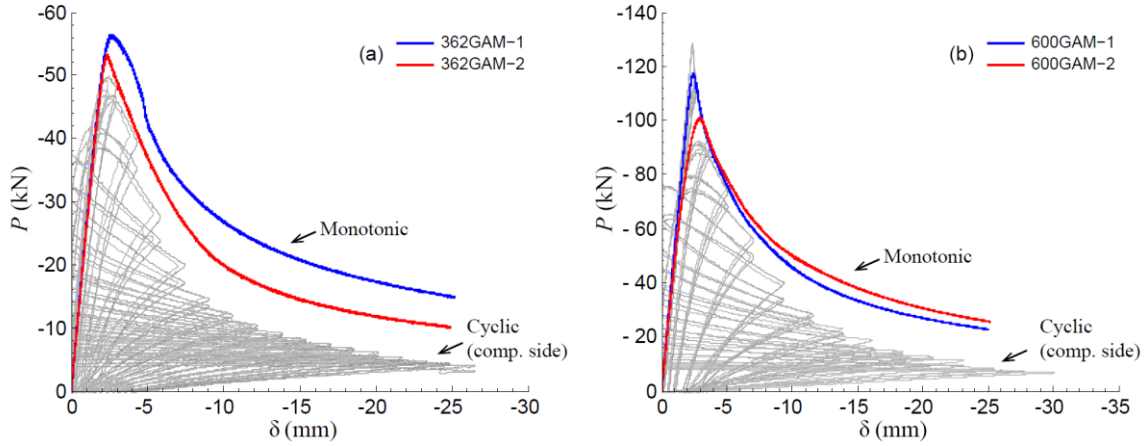

Fig. 4.10. Global buckling monotonic response envelope, (a) 362 series, (b) 600 series (Tension side of the cyclic responses has been omitted).

4.6.2 Local buckling limit state

Cyclic response of the local buckling (LAC) specimens was characterized by web buckling with at least two half-waves occurring before reaching the peak compressive load. After the peak load in compression, one half-wave locked around mid-height and damage accumulated at that location (see Fig. 4.11d). Compressive strength and unloading stiffness then degraded quickly on the compression side as shown in Fig. 4.11(b-c); however unlike global buckling members, unloading from compression was linear for all excursions (see Fig. 4.12). The difference between the monotonic curves and the compression side of the cyclic responses in Fig. 4.12 demonstrates this deterioration. Strength in tension deteriorated faster in the 600LAC specimens than for the 362LAC specimens. The 362LAC specimens experienced yielding close to the rounded corners and a yield line across the web. Tearing started thereafter at the center of the web and propagated to the corners, and rest of the cross-section. The 600LAC specimens exhibited similar behavior, but as shown in Fig. 4.11d, two yield lines formed around mid-height where tearing occurred. The 600LAC specimens underwent about 100 cycles after which the web was still carrying some tensile load.

The monotonic response of the local buckling (LAM) specimens demonstrated similar deformations as their cyclic counterpart; however, in the 362LAM specimens these deformations occurred closer to the top end plate. Initial stiffness for the 362LAM specimens was lower than for their cyclic counterparts due to initial imperfections (see Fig. 4.12a). The

later were larger for the 362LAM specimens ($\delta_B >= L/2940$ and $\delta_w >= H/330$) compared to the values observed for the 362LAC specimens ($\delta_B <= L/3900$ and $\delta_w <= H/342$). Initial imperfections straighten out in members under cyclic loading reducing their influence on the initial stiffness under compression loading. The initial stiffness of the 600LAM specimens is similar to their cyclic counterpart (600LAC specimens) as shown in Fig. 4.12b. The imperfections observed in the 600LAM specimens were smaller ($\delta_B >= L/1465$ and $\delta_w >= H/313$) than those observed in the 600LAC specimens ($\delta_B >= L/1277$ and $\delta_w >= H/95$), and thus the effects in the initial stiffness are less evident. Both cyclic and monotonic exceeded the predicted compressive capacity P_n, but the maximum tension strength fell below the yield load P_y for the 600LAC specimens (see Table 4.7). It is hypothesized that for thinner members (e.g., 600S162-33-LAC) the flanges and corners carried more of the tensile load than the web, and therefore, the cross-section was not fully effective in tension. This as a consequence of the large web buckling deformations during compression excursions that did not fully straightened out when loading in tension leading to non-uniform yielding across the section.

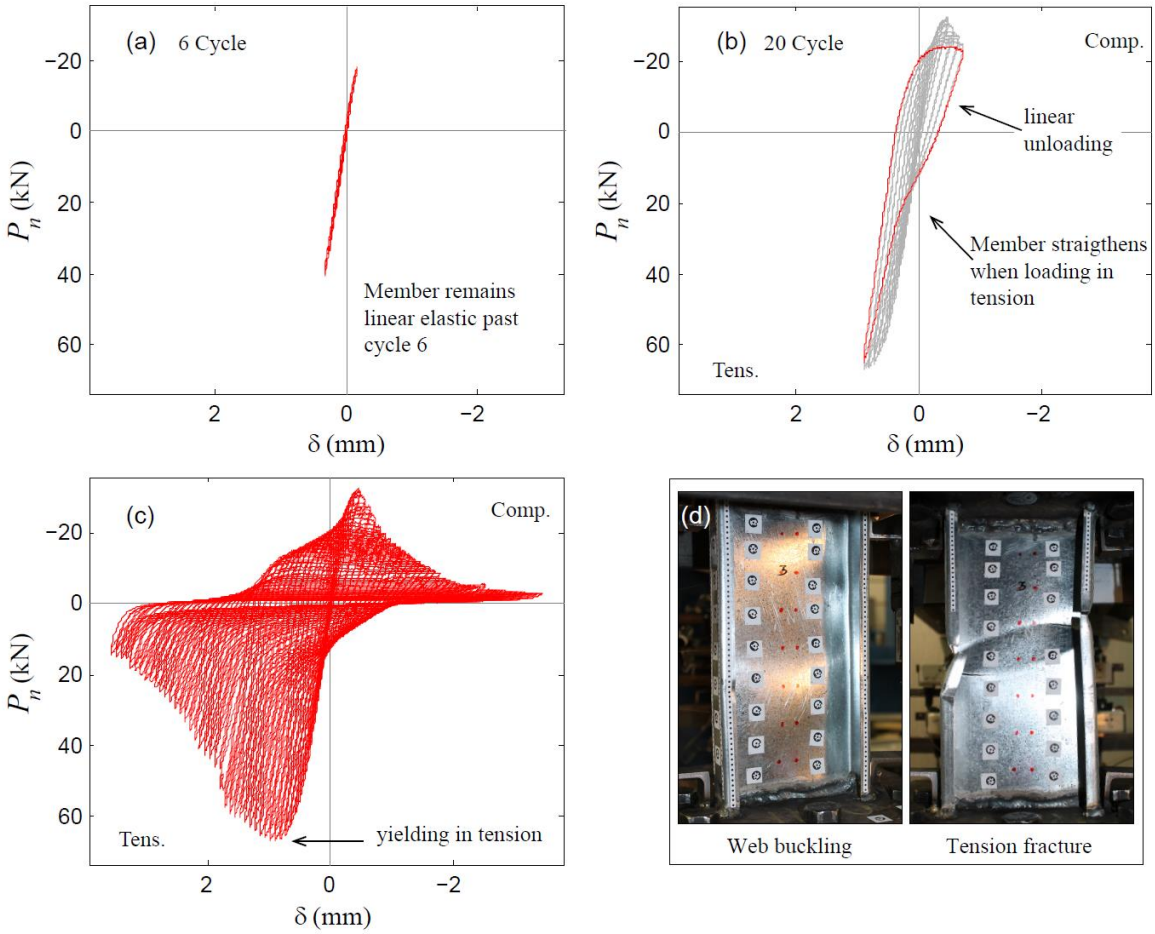

Fig. 4.11. Cyclic load-deformation response specimen 600S162-33-LAC-2,
(a) 6 cycles, (b) 20 cycles, (c) complete response, (d) failure mode.

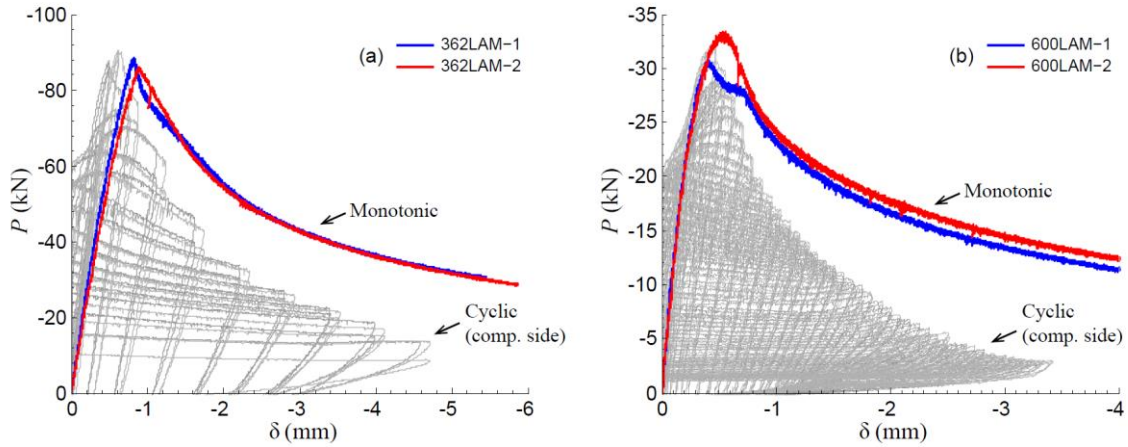

Fig. 4.12. Local buckling monotonic response envelope, (a) 362 series, (b) 600 series
(Tension side of the cyclic responses has been omitted).

4.6.3 Distortional buckling limit state

The cyclic response of the distortional buckling 600DAC specimens was characterized by the formation of at least one half-wavelength centered at mid-height as seen in Fig. 4.13d. Damage accumulated from inelastic strains at the rounded corners as the member stretched and compressed. Strength in compression and unloading stiffness degraded due to the inelastic strains accumulated in the damaged half-wave as shown by the difference between the monotonic curves and the cyclic envelopes in Fig. 4.14. The strength in tension remained constant until tearing started at the rounded corners and propagated around the cross section. The deformations experienced by the 362DAC specimens were a combination of distortional and local buckling of the web near one of the end plates. However, web buckling deformations were more visually noticeable than opening of the flanges. The hysteretic behavior of the 362DAC members was found to be similar to the behavior of the local buckling 362LAC specimens. The 362DAC specimens experienced fewer cycles than the 600DAC specimens before fracture, for instance 25 cycles versus 50 cycles for the 362S137-68-DAC-1 and 600S137-68-DAC-1 specimens respectively. The cumulative axial deformations at fracture for the 362DAC specimens were, $\Sigma\delta/L<0.7$, about half of the cumulative axial deformations of the 600DAC specimens, $\Sigma\delta/L<1.4$ (see Fig. 4.17).

The monotonic response of the DAM specimens exhibited similar deformations as their cyclic counterpart. Their initial stiffness however, is lower than for the DAC specimens as seen in Fig. 4.14. The 600DAM specimens exceeded the predicted capacity in compression while the 362DAM specimens reached values 2% to 6% lower than P_n for both cyclic and monotonic (see Table 4.7).

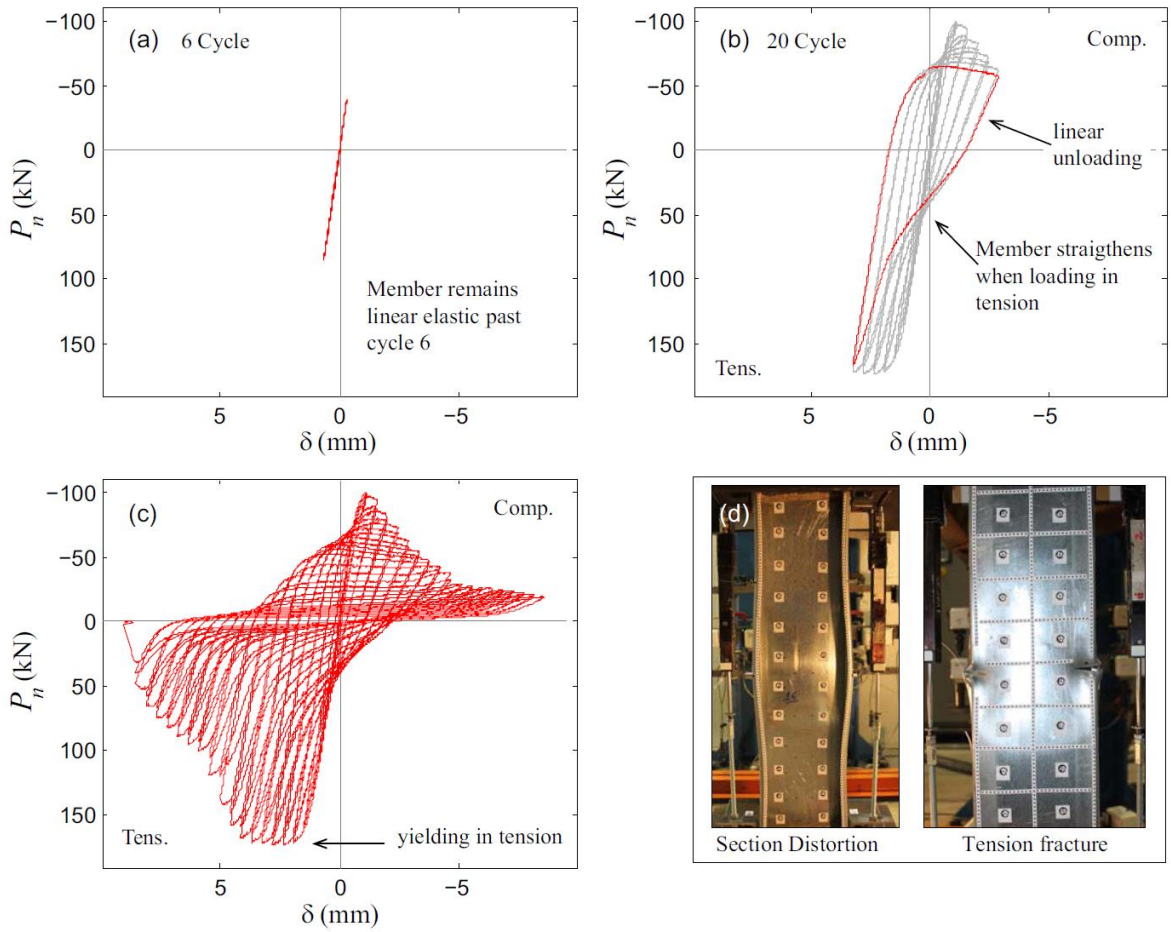

Fig. 4.13. Cyclic load-deformation response specimen 600S137-68-DAC-2, (a) 6 cycles, (b) 20 cycles, (c) complete response, (d) failure mode.

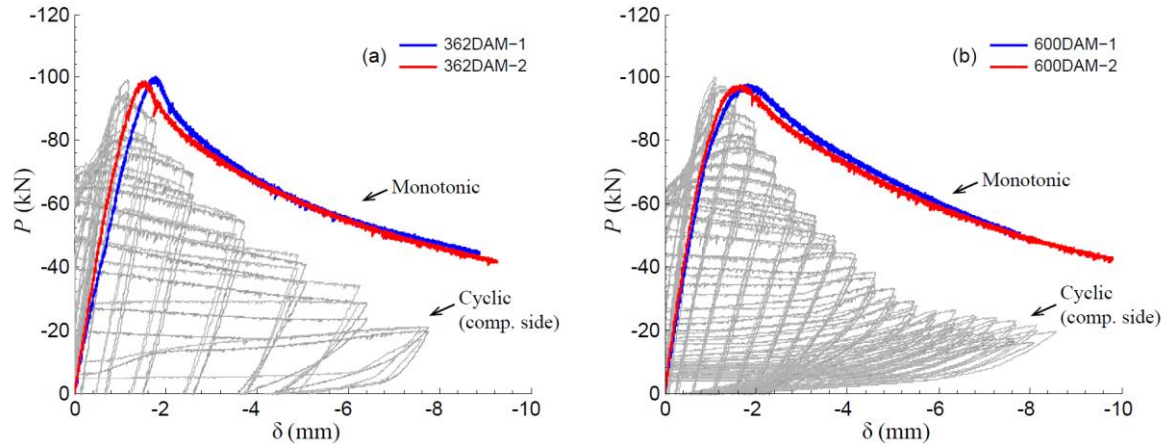

Fig. 4.14. Distortional buckling monotonic response envelope, (a) 362 series, (b) 600 series (Tension side of the cyclic responses has been omitted).

4.6.4 Monotonic tension response

The monotonic tension response of the 362LAMT specimens was linear up to about 80% of the peak tension load (P_{max}) when yielding starts, then a short nonlinear segment followed by a linear segment with decreased stiffness and large axial deformations up to the peak tension load (see Fig. 4.15). Strength reduces rapidly after peak load when tearing started and until complete fracture of the cross section occurs. The normalized axial deformations δ/δ_y reached far exceed the maximum normalized deformations reached during the tension excursions by any of the specimens that underwent cyclic loading (see Table 4.7). The monotonic responses when normalized to P_y and δ_y shown in Fig. 4.15 are considered here as representative of the behavior in tension of all the tested CFS members.

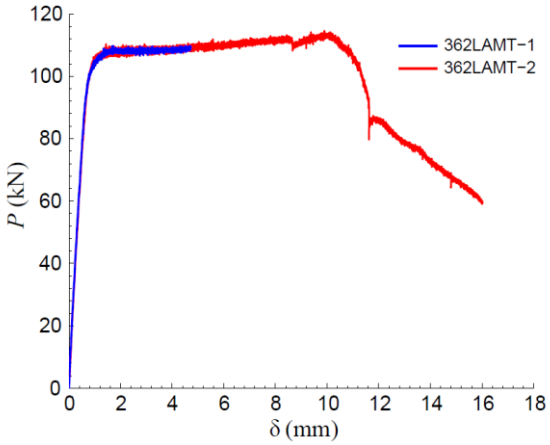

Fig. 4.15. Tension monotonic response of 362LAMT specimens.

4.6.5 Load-deformation response comparisons

Meaningful comparisons of hysteretic response across limit states are challenging because of the different cross-sections, specimen lengths, and buckling failure modes considered in this study. The amount of strength degradation, stiffness degradation, and pinching of the hysteretic response varies for the different specimens; however, the behavior is similar across the different buckling modes, lengths and cross-sections considered. Fig. 4.16 compares the normalized envelopes of the hysteretic response of all the specimens in this study. It can be seen that all the specimens have the same normalized pre-buckling stiffness k/k_e ($k_e = AE/L$). Strength in compression, compared to the peak compression load,

decreased in all specimens at similar rates as the axial deformation δ/δ_y increased ($\delta_y=P_y/k_e$). In tension however, the same trend is not observed with increasing axial deformation δ/δ_y. The maximum normalized axial deformation in compression was similar for all the specimens.

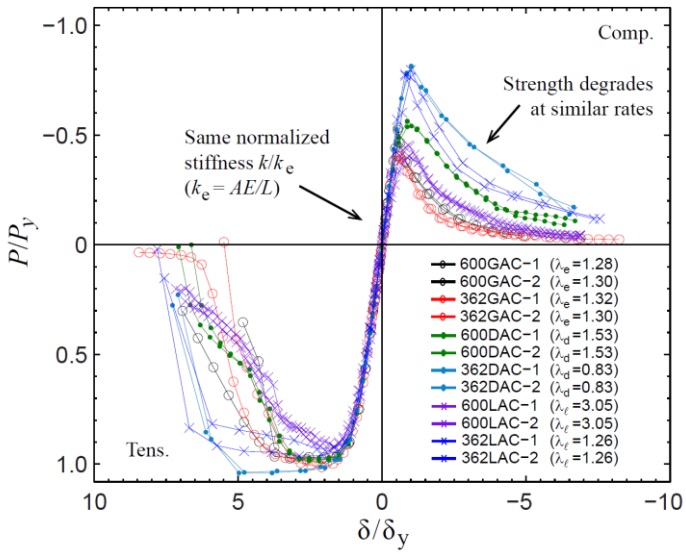

Fig. 4.16. Cyclic *P-δ* response envelopes.

4.7 Energy Dissipation of CFS Axial Members

Even though the cyclic envelopes in Fig. 4.16 and in general the cyclic behavior is similar for all the specimens, there are differences in the hysteretic response. Specimens with smaller cross-sectional slenderness exhibited less pinching of the load-deformation response that translated in differences on the amount of hysteretic energy dissipated. Fig. 4.17a compares the normalized hysteretic energy per cycle as a function of cumulative axial displacement $\Sigma\delta/L$. The hysteretic energy dissipated each cycle E_{ci} was normalized to the area of the rectangle E_{cr} bounded by the maximum and minimum axial deformation experienced in that cycle and the predicted strengths in compression and tension (see inset in Fig. 4.17a). The energy curves for the 362LAC and 362DAC specimens show the largest per cycle energy dissipation values (higher than 0.35), with short *cumulative deformation life* values (represented by the total cumulative axial deformation $\Sigma\delta/L$, see Table 4.9). The 600GAC and 362GAC specimens exhibit the least amount of energy dissipation as caused by more severe pinching of the load-deformation response. For the local and distortional

buckling specimens, the unloading stiffness from compression to tension is higher than for global buckling specimens leading to less pinching of the load-deformation response and more energy dissipated per cycle.

Energy dissipated decreases with increasing cross-sectional slenderness within the damaged half-wave, which is consistent with previous studies (see [15]). Fig. 4.17b shows per cycle hysteretic energy dissipated per half-wavelength as a function of the cumulative axial deformation $\Sigma\delta/L$. Specimens with the higher cross-sectional slenderness (e.g., 600LAC and 600DAC) dissipate less energy per half-wavelength (per cycle and total) but have the largest cumulative deformation life (see last column of Table 4.9). For instance, in Fig. 4.17b the curves corresponding to the 600LAC and 600DAC members show smaller values of energy dissipated per cycle per half-wave (lesser than 2.5 kN-mm/mm) with longer cumulative deformation life values (total $\Sigma\delta/L>1.0$) than the other specimens. In contrast, the specimens experiencing inelastic buckling (e.g., 362LAC and 362DAC) dissipate more energy per cycle per half-wavelength, but fracture in tension with shorter cumulative deformation life (total $\Sigma\delta/L<0.7$). This trend is also observed in the case of the cumulative hysteretic energy dissipated within the damaged half-wave. Table 4.9 summarizes the cumulative hysteretic energy (HE) dissipated at cumulative axial deformations $\Sigma\delta/L$ = 0.25, 0.5, 1.0 and at fracture (i.e., the end of the test). From this table it can be seen that the cumulative energy dissipated per half-wavelength (HE/L_{cr}) is larger for specimens that exhibited inelastic buckling (i.e., 362LAC and 362DAC specimens). However, the cumulative deformation life is shorter as mentioned above. Fig. 4.18 shows the total hysteretic energy dissipated within the damaged half-wave as a function of the member slenderness (see HE_T/L_{cr} in Table 4.9). It is clear from the figure that as cross-sectional slenderness decreases the energy dissipation capacity per half-wave length increases. Specimens experiencing global buckling (e.g., 600GAC and 362GAC) have the lowest energy dissipation capacity per half-wavelength and have a short cumulative deformation life compared to the other buckling limit states. Since the response of the 362DAC specimens was similar to the 362LAC specimens, the half-wavelength and slenderness values used in Fig. 4.17b and Fig. 4.18 are the corresponding λ_ℓ and $L_{cr\ell}$ from Table 4.3.

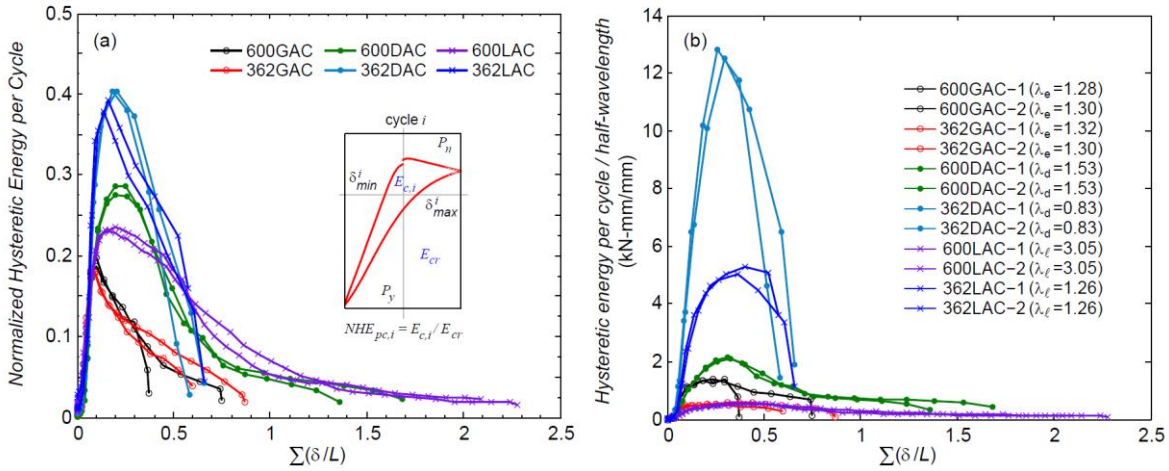

Fig. 4.17. Hysteretic energy per cycle vs. cumulative axial deformation
(a) normalized, (b) per half-wavelength.

Table 4.9. Hysteretic energy dissipation for axial members.

Specimen	$HE_{0.25}$	$HE_{0.5}$	$HE_{1.0}$	HE_T	$HE_{0.25}/L_{cr}$	$HE_{0.5}/L_{cr}$	$HE_{1.0}/L_{cr}$	HE_T/L_{cr}	max $\Sigma\delta/L$
	(kN-mm)				(kN-mm/mm)				(×100)
600S137-97-GAC-1	12234	-	-	16063	10.70	-	-	14.05	37
600S137-97-GAC-2	12339	19327	-	22983	10.79	16.91	-	20.11	75
362S137-68-GAC-1	5676	10176	-	14952	4.97	8.90	-	13.08	87
362S137-68-GAC-2	5508	9078	-	10009	4.82	7.94	-	8.76	60
600S137-68-DAC-1	3125	6191	8234	8935	12.06	23.90	31.78	34.49	136
600S137-68-DAC-2	2844	5800	7598	8960	11.00	22.43	29.38	34.65	168
362S137-68-DAC-1	3131	5846	-	6458	44.02	82.20	-	90.81	66
362S137-68-DAC-2	3614	6195	-	6368	50.81	87.11	-	89.55	58
600S162-33-LAC-1	630	1313	2033	2550	5.64	11.75	18.19	22.82	209
600S162-33-LAC-2	593	1248	1863	2344	5.33	11.22	16.74	21.07	228
362S162-54-LAC-1	1580	3270	-	3839	22.21	45.98	-	53.98	57
362S162-54-LAC-2	1767	3316	-	3773	24.67	46.29	-	52.68	66

HE_{xx} = cumulative hysteretic energy dissipated up to $\Sigma\delta/L$ = xx.
HE_T = cumulative hysteretic energy dissipated until failure.

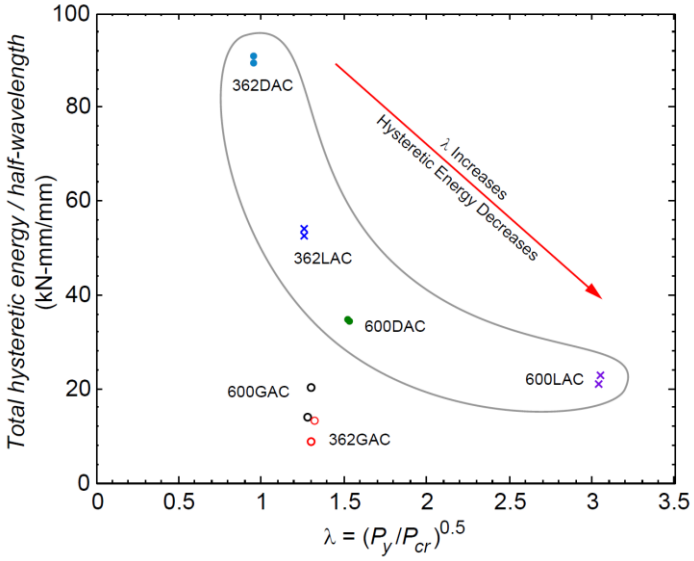

Fig. 4.18. Total hysteretic energy per half-wavelength (HE_T/L_{cr}) vs. cross-sectional or global slenderness.

5 Hysteretic Model for CFS Axial Members

Hysteretic models capable of accurately simulating the behavior of CFS axial members need to capture the asymmetric nature of the cyclic response, strength and stiffness degradation, as well as the pinching of the load-deflection curve. In the work presented herein, characterization of the cyclic response is pursued using the uniaxial material model *Pinching4* [40] as implemented in OpenSees [41]. The model (shown in Fig. 5.1) is defined by a backbone curve, unloading-reloading paths that account for pinching, and a damage model for strength and stiffness degradation. The backbone curves are derived from normalized monotonic responses and the damage model for strength and stiffness deterioration is calibrated by comparing the monotonic and cyclic responses. The calibration procedure is described below.

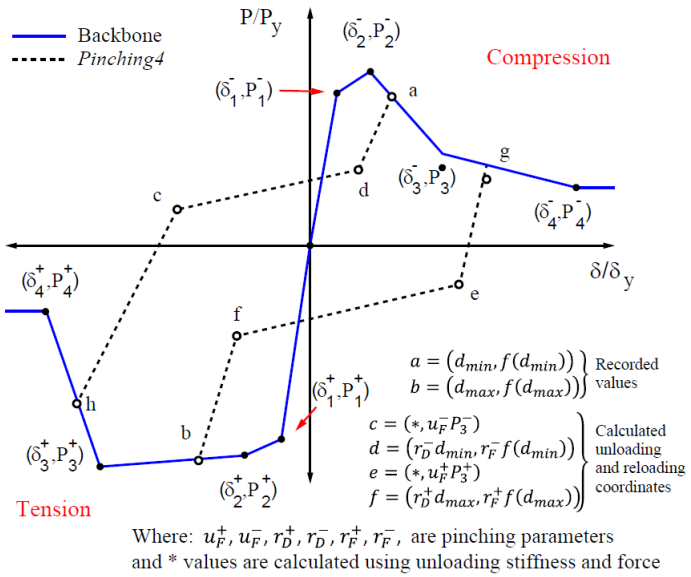

Fig. 5.1. *Pinching4* material model for CFS axial members.

5.1 Monotonic Response Characterization – Backbone

Backbone curves were fit to the monotonic test data using a combination of defined anchor points and fit values to match the energy represented by the area under the monotonic load-deformation curve. The backbone consists of load and displacement coordinates, labeled as δ_i, P_i in Fig. 5.1, for eight unique points, four in compression and four in tension. It is noted that the hysteric modeling is conducted in normalized coordinates (δ/δ_y, and P/P_y)

to allow more direct comparison between specimens and to facilitate application of the hysteric parameters to different configurations. The anchor points for tension and compression are described in the following sections and the remaining values were selected using a least squares method to minimize the error between the energy dissipated in the monotonic tests and the energy dissipated by the multi-linear model. The fit was performed separately for pre-peak and post-peak energy to prevent over or under compensation of the dissipated energy [42]. Additional constraints were utilized to encourage the model backbone to resemble the experimental curve.

5.1.1 Compression Backbone

Two line segments prior to the peak load were used to capture the elastic and pre-buckling nonlinearities in the response. Backbone point (δ_2^-,P_2^-) as shown in Fig. 5.1 was anchored to the point of maximum compression load and corresponding displacement. Two post-peak segments with negative slope were included to account for the softening and post-peak strength loss as observed from the tests. Point (δ_4^-,P_4^-) was anchored to an axial deformation δ=6.0δ_y and associated force obtained from the test data. This point corresponds to strength loss of at least 50% for all tested specimens and a zero-slope is assumed beyond this point. The coordinates for backbone point 1 and 3 were found using a least squares fit to create the same amount of area under the pre-peak, and post-peak curves respectively. The coordinates defining the fit compression backbones are summarized in Table 5.1.

5.1.2 Tension Backbone

For tension, the backbone is calibrated from the two monotonic tests listed in Table 4.1. These tests are considered here to be representative of the tension behavior of the tested CFS members. Three segments prior to peak load are intended to capture the initial yielding and post-yielding part of the response. A fourth segment with negative slope is included to represent the loss of strength due to tearing and fracture observed from the tests. The coordinates defining the tension backbone are summarized at the bottom of Table 5.1.

However, one of the shortcomings of the *Pinching4* hysteretic model is that while the backbone can be separately defined in compression and tension, the strength and stiffness degradation parameters are universal to both compression and tension. The effect of the

accumulation of damage on compression and tension response of cold-formed steel members is significantly different. An attempt was made therefore to improve the behavior of the hysteretic model by adjusting the tension backbone. The adjusted tension backbone was developed as a hybrid between the monotonic tests and the tension side of the cyclic envelopes shown in Fig. 4.16. As a result the adjusted backbone is defined using larger forces and smaller normalized deformations than the backbones fit to the monotonic tension tests. The adjusted tension backbone is given at the bottom of Table 5.1 and shown graphically in Fig. 5.2.

Table 5.1. Backbone definition points for each specimen.

	Specimen	P_y (kN)	k_e [(a)] (kN/mm)	δ_y [(b)] (mm)	δ_1/δ_y	δ_2/δ_y	δ_3/δ_y	δ_4/δ_y	P_1/P_y	P_2/P_y	P_3/P_y	P_4/P_y	k_1/k_e	k_2/k_e ($\times10^{-3}$)	k_3/k_e ($\times10^{-3}$)	k_4/k_e ($\times10^{-3}$)
	Compression															
1	600S137-97-GAM-1	245	56.13	4.36	0.463	0.562	1.394	5.600	0.433	0.482	0.210	0.096	935	490	-326	-27
2	600S137-97-GAM-2	249	56.23	4.42	0.452	0.664	1.815	5.600	0.373	0.414	0.205	0.107	826	195	-182	-26
3	362S137-68-GAM-1	123	28.04	4.40	0.440	0.618	1.642	5.600	0.414	0.460	0.233	0.124	942	258	-222	-28
4	362S137-68-GAM-2	122	28.08	4.35	0.419	0.535	1.528	5.600	0.391	0.435	0.181	0.083	933	374	-256	-24
5	600S137-68-DAM-1	177	138.86	1.28	0.837	1.427	3.779	6.000	0.493	0.548	0.377	0.286	589	93	-72	-41
6	600S137-68-DAM-2	177	138.36	1.28	0.758	1.278	3.438	6.000	0.495	0.549	0.379	0.284	652	106	-79	-37
7	362S137-68-DAM-1	124	106.13	1.17	1.144	1.523	3.045	6.000	0.735	0.816	0.556	0.417	642	215	-171	-47
8	362S137-68-DAM-2	123	105.68	1.17	0.935	1.293	3.100	6.000	0.724	0.804	0.549	0.411	774	225	-141	-48
9	600S162-33-LAM-1	72	143.49	0.50	0.526	0.816	2.913	6.000	0.385	0.427	0.259	0.188	731	147	-80	-23
10	600S162-33-LAM-2	72	143.56	0.50	0.608	1.110	2.234	6.000	0.416	0.462	0.298	0.203	684	92	-146	-25
11	362S162-54-LAM-1	113	181.80	0.62	1.017	1.309	2.877	6.000	0.699	0.777	0.478	0.333	688	266	-190	-47
12	362S162-54-LAM-2	113	181.92	0.62	1.108	1.434	2.791	6.000	0.681	0.756	0.489	0.331	614	232	-197	-49
	Tension															
14	362S162-54-LAMT-1	113	181.46	0.62	0.976	1.669	7.232	-	0.823	0.953	0.967	-	847	213	3	-
15	362S162-54-LAMT-2	114	182.79	0.62	1.126	2.880	16.168	25.633	0.870	0.957	0.997	0.450	779	102	3	-58
16	Tension Adjusted	114	182.79	0.62	1.128	1.488	6.000	8.000	1.044	1.134	1.172	0.872	926	250	9	-150

(a) $k_e = A_gE/L$ (E=203.4GPa)

(b) $\delta_y = P_y/k_e$

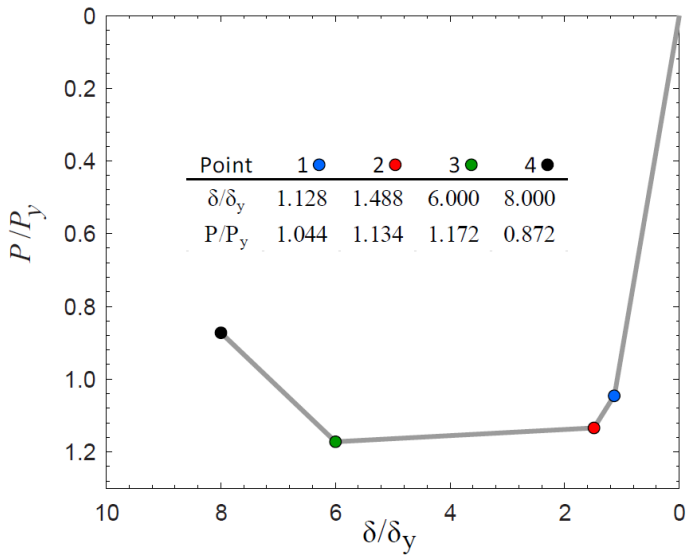

Fig. 5.2. Tension backbone coordinates.

5.2 Cyclic Response Characterization

Strength and stiffness deterioration are simulated in *Pinching4* using damage rules that are a function of the hysteretic energy dissipated and the historic deformation demand [35, 36]. Three damage rules are available in *Pinching4*, to simulate strength, unloading stiffness and reloading stiffness deterioration. Both strength (Eq. 5.1) and unloading stiffness (Eq. 5.2) degradation were incorporated in the proposed hysteretic model whereas reloading stiffness deterioration was neglected. The damage rules were defined using the damage index for backbone strength, $\eta_{f,i}$, and damage index for stiffness, $\eta_{k,i}$, as follows:

$$f_{\max,i} = (1-\eta_{f,i})\, f_{\max,o} \qquad 5.1$$

$$k_i = (1-\eta_{k,f})k_o \qquad 5.2$$

$$\eta_i = \beta_1(\tilde{d}_{\max,i})^{\beta 3} + \beta_2(E_i/(\gamma_E \cdot E_m))^{\beta 4} \le \gamma_{\text{limit}} \qquad 5.3$$

where the index i = current load excursion value; o = value achieved if damage were not included (i.e. monotonic backbone curve); f_{max} = maximum strength for the current excursion, k = unloading stiffness, E_i = cumulative hysteretic energy dissipated during previous excursions, E_m = maximum of the energy dissipated under monotonic loading in achieving point P_4 in Fig. 5.1; γ_E = parameter to define the maximum energy dissipated during cyclic

loading; and β_i = parameters fitted from experimental data. In general experimental values of the damage index η_i are calculated from the tests, and a least squares fit using Eq. 5.3 is employed to obtain values β_i for each tested member. For the proposed hysteretic model, the damage was computed as a function of energy rather than peak deformations so the term relating damage to peak displacements was removed by setting $\beta_1 = \beta_3 = 0$.

5.2.1 Strength degradation

Strength deterioration was calculated as the positive difference on strength between the monotonic backbone force ($f_{max,o}$) and the cyclic force envelope ($f_{max,i}$). The strength degradation behavior differs substantially between compression and tension excursions as shown in Fig. 5.3. In compression, strength deteriorates faster with a reduction at the end of the test of more than 50% the maximum strength. The curves in Fig. 5.3a suggest that compression strength degradation is cross-section and length independent. In tension the strength deterioration was more gradual, almost negligible, until tearing started and most or all strength was lost (i.e. fracture, see Fig. 5.3b). In the *Pinching4* hysteretic model, the accumulation of damage is defined to be the same in both tension and compression loading directions; hence, it was necessary to use the average of the strength deterioration in compression and tension to define the degradation parameters. The fitted β_i values fitted to each specimen's curve are listed in Table 5.2.

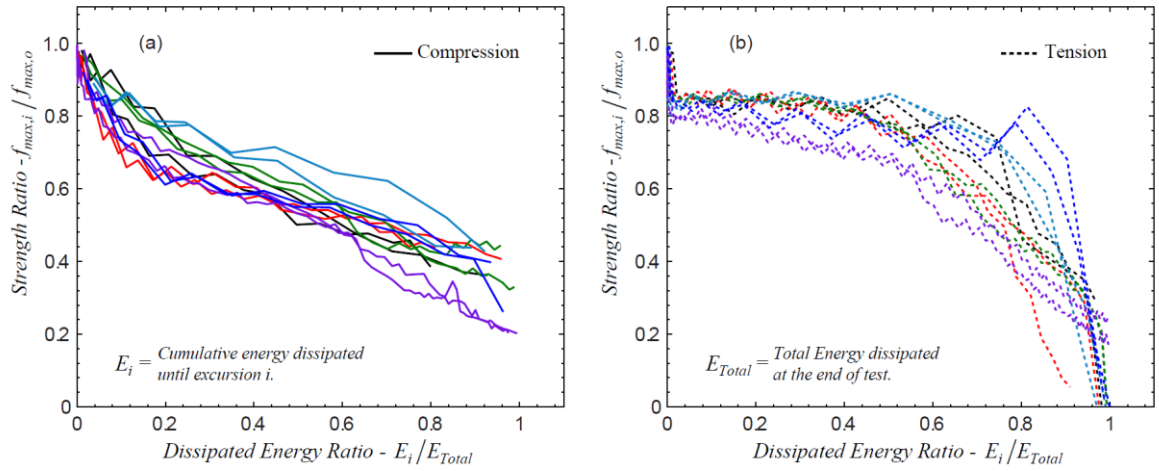

Fig. 5.3. Strength degradation, (a) compression; (b) tension.

5.2.2 Stiffness degradation

Unloading stiffness values were obtained by fitting a line to the unloading paths of the cyclic responses. The model is fit using a least squares method to minimize the error on the predicted load. The unloading stiffness is therefore the slope of segments *g*-*e* and *h*-*c* as shown in Fig. 5.1.

The differences between unloading stiffness degradation in tension and compression are even greater than the differences in strength degradation as shown in Fig. 5.4a. Unloading stiffness in compression rapidly decreases soon after the maximum compression is reached. Fig. 5.4a shows that unloading stiffness in compression for global buckling members is more pronounced than it is for local and distortional buckling members. A reduction of more than 80% occurs before 20% of the hysteretic energy is dissipated for global members. In tension, unloading stiffness deterioration happens more gradually than in compression and there is little distinction between the different buckling modes (global, local, or distortional) (see Fig. 5.4b). As was the case with strength degradation, the both experimental tension and compression values of $\eta_{k,i}$ were used to develop the stiffness degradation parameters since the hysteretic model does not allow definition of different tension and compression degradation. The fitted β_i values are listed in Table 5.2.

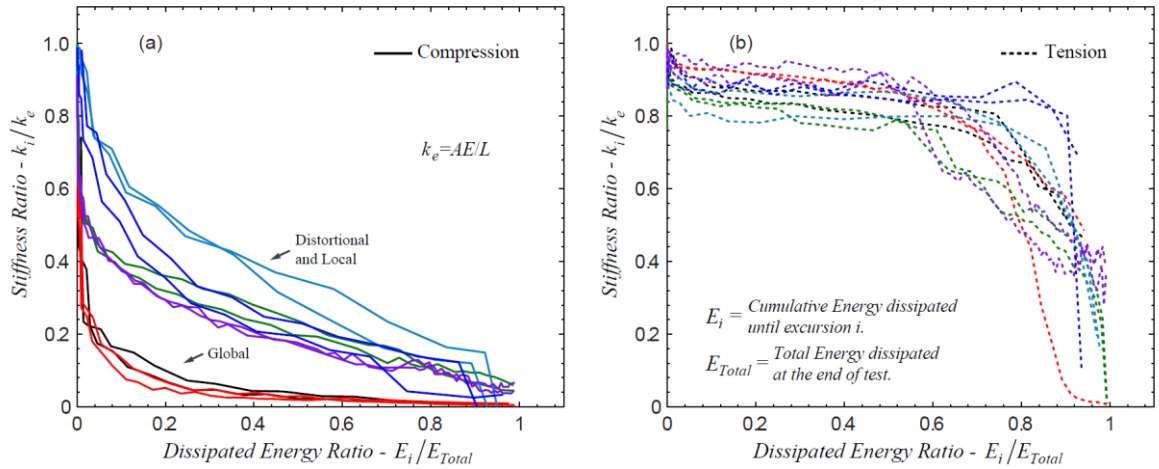

Fig. 5.4. Stiffness degradation, (a) compression; (b) tension.

5.2.3 Pinching behavior

The pinching behavior is defined by a set of pinching parameters, u_{F+}, u_{F-}, r_{D+}, r_{D-}, r_{F+}, and r_{F-}. The parameters r_{D-} and r_{D+} are the ratio of the deformation at which reloading starts (points *d* and *f* in Fig. 5.1) to the maximum/minimum historic deformation, d_{min} and d_{max}. The parameters r_{F-} and r_{F+} are the corresponding ratios of the load at the point at which reloading starts (points *d* and *f*) to the load corresponding to the maximum historic displacement, $f(d_{min})$ and $f(d_{max})$. The parameters u_{F-} and u_{F+} are the ratios of the load developed after unloading (point *c* and *e* in Fig. 5.1) to the load coordinate of backbone point 3, P_{3-} and P_{3+}.

An initial attempt to characterize pinching was made by fitting a tri-linear model to each unloading and reloading curve using a least squares method. The coordinates of the fitted points defining each segment were used to derive a first estimate of pinching parameters r_{D+}, r_{D-}, r_{F+}, r_{F-}, u_{F+}, and u_{F-} for every cycle. It was found, however, that these values are not constant and varied as the number of cycles increased. Since the pinching behavior in *Pinching4* is defined using constant pinching parameters, a second method was developed to consider the entire data set from a test. The second method consisted of minimizing the error between the dissipated hysteretic energy produced by the model and the experimentally observed energy dissipation. The optimization problem was implemented in MATLAB [43] using the average values of r_{D+}, r_{D-}, r_{F+}, r_{F-}, u_{F+}, and u_{F-} from the first estimate described above as seed values. Constraints were set to ensure the modeled load-deformation shape approximated the test data while minimizing the error in energy. The slopes of segments *h-c*, *c-d*, and *d-a* were constrained such that they decrease in that order (i.e. $k_{hc} > k_{cd} > k_{da}$). The load at point *c* was constrained to remain negative. The obtained values for r_{D+}, r_{D-}, r_{F+}, r_{F-}, u_{F+}, and u_{F-} are listed in Table 5.2 and a statistical evaluation of the pinching parameters as well as the damage parameters is given in Table 5.3.

Table 5.2. *Pinching4* model parameters for each specimen.

Specimen	Damage Parameters						Pinching Parameters						
	Strength [a]		Stiffness [a]				Compression			Tension			Backbone
	β_2	β_4	β_2	β_4	γ_E	E_M [b]	r_{D-}	r_{F-}	u_{F-}	r_{D+}	r_{F+}	u_{F+}	Used [c]
600S137-97-GAC-1	0.70	0.98	0.69	0.20	1.88	8541	0.40	0.92	0.50	0.55	0.25	-0.10	1, 16
600S137-97-GAC-2	0.58	0.60	0.73	0.22	2.62	8761	0.40	0.92	0.50	0.75	0.25	-0.10	1, 16
362S137-68-GAC-1	0.69	0.71	0.90	0.33	3.39	4417	0.40	0.92	0.50	0.35	0.25	-0.03	4, 16
362S137-68-GAC-2	0.66	0.70	0.70	0.22	2.25	4450	0.48	0.92	0.50	0.50	0.25	-0.03	4, 16
600S137-68-DAC-1	0.71	1.04	0.68	0.30	4.78	1868	0.66	0.92	0.50	0.80	0.30	-0.10	6, 16
600S137-68-DAC-2	0.68	0.82	0.72	0.27	4.86	1863	0.66	0.92	0.50	0.80	0.26	-0.10	6, 16
362S137-68-DAC-1	0.68	1.04	0.70	0.52	5.05	1260	0.65	0.92	0.50	0.45	0.62	-0.03	8, 16
362S137-68-DAC-2	0.67	1.09	0.67	0.40	4.95	1270	0.60	0.92	0.50	0.53	0.62	-0.03	8, 16
600S162-33-LAC-1	0.71	0.55	0.68	0.33	8.68	294	0.48	0.92	0.50	0.80	0.30	-0.10	10, 16
600S162-33-LAC-2	0.78	0.73	0.73	0.33	8.47	293	0.48	0.92	0.50	0.80	0.30	-0.10	10, 16
362S162-54-LAC-1	0.55	0.49	0.66	0.43	6.63	579	0.48	0.92	0.50	0.53	0.62	-0.03	11, 16
362S162-54-LAC-2	0.56	0.46	0.62	0.32	6.49	581	0.49	0.92	0.50	0.53	0.62	-0.03	11, 16

(a) Fit using positive and negative excursions; (b) Energy in units of kN-mm; (c) Backbone curve from Table 5.1

Table 5.3. Statistics for *Pinching4* parameters.

	Damage Parameters						Pinching Parameters					
	Strength		Stiffness				Compression			Tension		
	β_2	β_4	β_2	β_4	γ_E	E_M	r_{D-}	r_{F-}	u_{F-}	r_{D+}	r_{F+}	u_{F+}
μ	0.66	0.77	0.71	0.32	5.00	2848	0.52	0.92	0.50	0.62	0.39	-0.07
cov	0.10	0.29	0.09	0.29	0.45	1.07	0.20	0.00	0.00	0.26	0.45	-0.56

μ = mean value; cov = coefficient of variation.

5.3 Generalized hysteretic model

It is desirable to develop generalized hysteretic models that can be applied to a wide range of cold-formed steel sections of varying length. Two options are explored here for calibration of a generalized hysteretic model to simulate the axial behavior of cold-formed members.

5.3.1 Generalized compression backbone curves

Generalized backbone curves for the compression side derived from the values in Table 5.1 require identifying a functional relationship between these values and cross-sectional slenderness. A power regression of the form $P_i/P_y = C\lambda^r$ was pursued as an initial hypothesis for such a relationship where λ is the slenderness corresponding to the governing buckling limit state (i.e., λ_e, λ_d or λ_ℓ). This approach is similar to the AISI Direct Strength Method approach in which strength in compression is a function of the governing slenderness member slenderness. A similar power regression $\delta_i/\delta_y = C\lambda^r$ was pursued for the

displacements. The resulting expressions are summarized in the lower half of Table 5.4 and shown in Fig. 5.5 along with the corresponding backbone coordinates from Table 5.1. Points corresponding to global buckling do not follow the trends observed, and regression including these points would result in very low backbones for the distortional and local buckling specimens. These points, therefore were excluded when fitting the coefficients *C* and *r* for the power regressions in Fig. 5.5. However, excluding these points also makes the obtained expressions applicable to members experiencing local and distortional buckling, but not global buckling.

Generalized expressions that could be applicable to all members irrespective of the governing buckling mode should be functions of all three slenderness values λ_e, λ_d and λ_ℓ. A power regression of the form $P_i/P_y = C\lambda_e^r\lambda_d^s\lambda_\ell^t$ was pursued where λ_e, λ_d and λ_ℓ are the corresponding slenderness calculated using DSM for a specific member. The resulting expressions are summarized in Table 5.4 and shown in Fig. 5.6 along with the corresponding backbone coordinates from Table 5.1. The resulting expression allows estimating backbone curves for compression side using the same set of coefficients irrespective of the governing buckling mode.

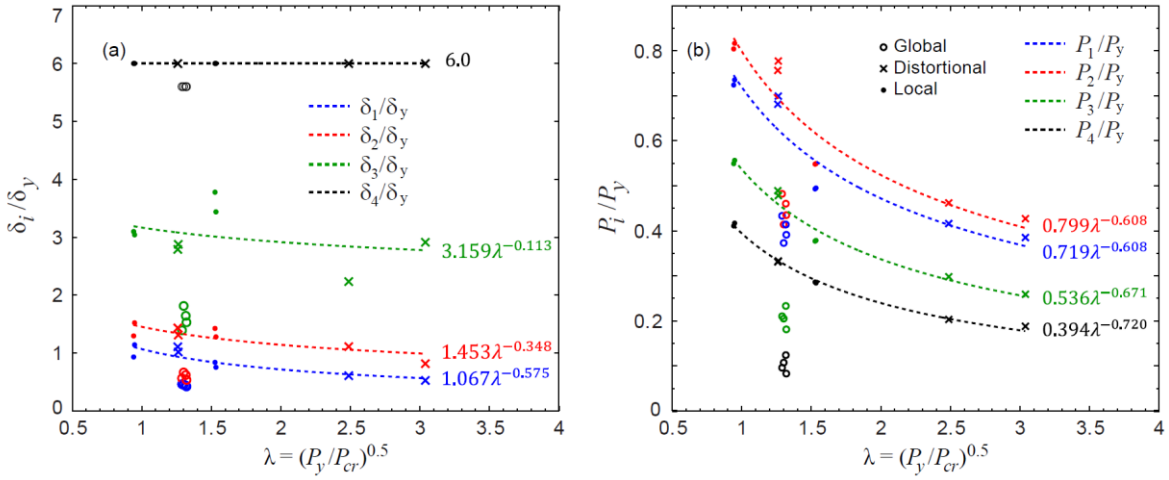

Fig. 5.5. Compression backbone coordinates as a function of governing λ.
(Global buckling data not included in the fit)

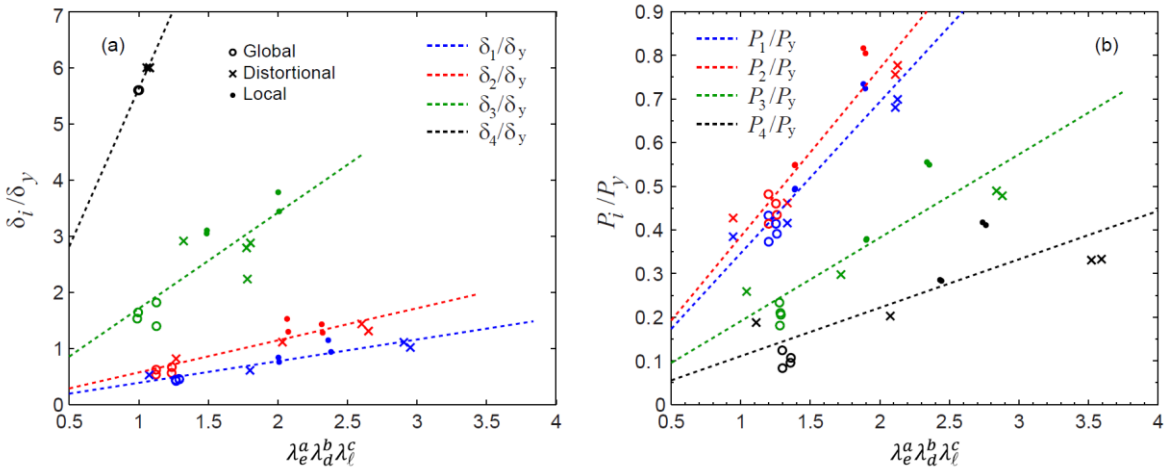

Fig. 5.6. Compression backbone coordinates as a function of λ_e, λ_d and λ_ℓ.

Table 5.4. Coefficients for generalized backbones.

Equation		δ_1/δ_y	δ_2/δ_y	δ_3/δ_y	δ_4/δ_y	P_1/P_y	P_2/P_y	P_3/P_y	P_4/P_y
$C\lambda_e^r\lambda_d^s\lambda_\ell^t$	C	0.386	0.571	1.708	5.626	0.347	0.385	0.191	0.111
	r	-1.014	-0.933	-0.585	-0.059	-0.687	-0.687	-0.988	-1.215
	s	1.509	1.704	1.352	0.079	0.777	0.777	1.415	1.932
	t	-1.886	-1.602	-0.908	-0.062	-1.357	-1.357	-1.860	-2.253
	$R^{2\,(a)}$	0.876	0.853	0.687	0.915	0.889	0.889	0.804	0.716
$C\lambda^r$	C	1.067	1.453	3.159	6.000	0.719	0.799	0.536	0.394
	r	-0.575	-0.348	-0.113	0.000	-0.608	-0.608	-0.671	-0.720
	$R^{2\,(a)}$	0.789	0.684	0.100	-	0.884	0.885	0.969	0.995

(a) Coefficient of determination

5.3.2 Generalized pinching parameters

In section 5.2 it was mentioned that strength degradation in compression appears to be cross-section and length independent and that tension degradation was almost negligible and seemed independent of cross-section and specimen length as well. The stiffness degradation curves in compression on the other hand, suggests a relationship with the cross-section slenderness, and the stiffness degradation behavior for global buckling specimens appeared to be different than local or distortional buckling. In addition, some of the parameters for *Pinching4* in Table 5.2 show large variations, *cov* values 20%, across the different specimens (See Table 5.3). Large variations suggest that the use of the average values might be inappropriate. For these reasons and because *Pinching4* requires the use of one set of strength/stiffness degradation parameters to be used in both compression and

tension; the relationship between the values in Table 5.2 with the global and cross-sectional slenderness was investigated.

Trends between each parameter with the slenderness corresponding to the governing buckling mode (i.e., λ_e, λ_d or λ_ℓ) are not clear as shown in Fig. 5.7a, and Fig. 5.8a. The scatter for each curve suggests that the generalized expression cannot be represented as a function of only the governing slenderness. A power regression of the form $\beta = C\lambda_e^a \lambda_d^b \lambda_\ell^c$ was pursued and the resulting curves are shown in Fig. 5.7b and Fig. 5.8b and the corresponding coefficients are summarized in Table 5.5. These expressions allow an approximation of the degradation coefficients β_2 and β_4 as well as pinching parameters r_{D+}, r_{D-}, r_{F+}, r_{F-}, u_{F+}, and u_{F-} for use with the *Pinching4* hysteretic model, irrespective of the governing buckling mode.

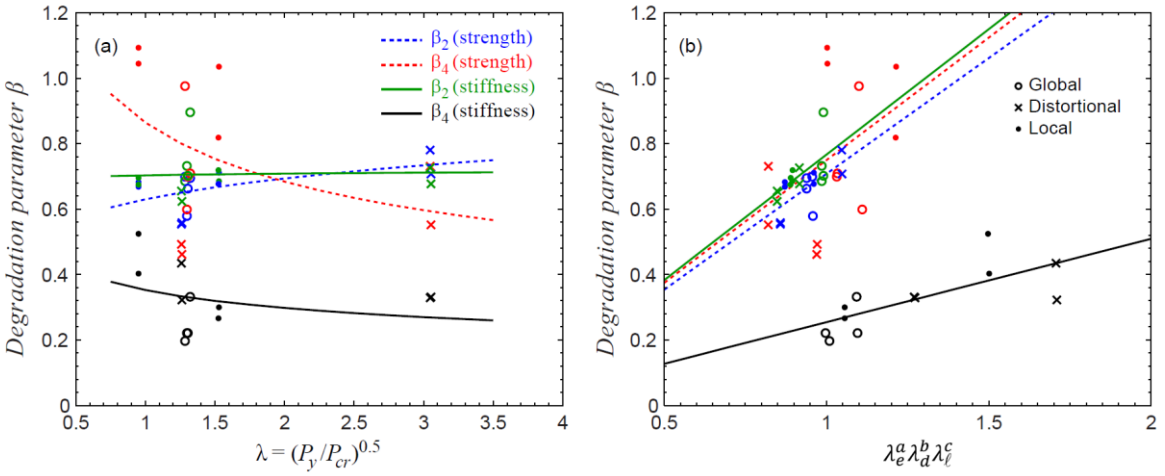

Fig. 5.7. Strength and stiffness degradation parameter β as a function of slenderness.

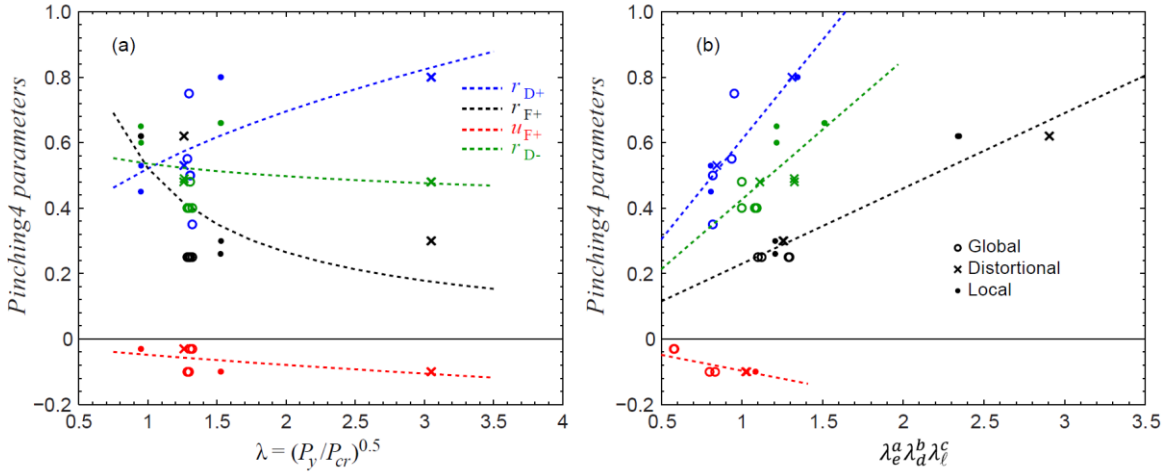

Fig. 5.8. *Pinching4* parameters as function of slenderness.

Table 5.5. Coefficients for generalized *Pinching4* parameters

		Damage Parameters					Pinching Parameters					
		Strength		Stiffness			Compression			Tension		
Equation		β_2	β_4	β_2	β_4	γ_E	r_{D-}	r_{F-}	u_{F-}	r_{D+}	r_{F+}	u_{F+}
$C\lambda_e^r\lambda_d^s\lambda_\ell^t$	C	0.708	0.749	0.766	0.255	3.083	0.426	0.92	0.50	0.609	0.230	-0.097
	r	0.142	-0.108	0.134	-0.340	-0.410	-0.322	0.00	0.00	0.104	-0.782	1.108
	s	-0.127	0.710	-0.159	-0.207	-0.140	0.889	0.00	0.00	0.480	0.057	0.417
	t	0.309	-0.431	0.179	-0.387	0.182	-0.563	0.00	0.00	0.393	-1.223	2.006
	$R^{2\,(a)}$	0.468	0.175	0.384	0.543	0.972	0.564	-	-	0.807	0.929	0.831
$C\lambda^r$	C	0.630	0.864	0.703	0.353	3.635	0.536	0.92	0.50	0.521	0.522	-0.048
	r	0.139	-0.338	0.011	-0.243	0.738	-0.107	0.00	0.00	0.417	-0.977	0.712
	$R^{2\,(a)}$	0.271	0.147	0.002	0.068	0.462	0.039	-	-	0.435	0.313	0.341

(a) Coefficient of determination

5.4 Simulated Axial Cyclic Responses

The calibrated hysteretic models are capable of capturing the observed response characteristics such as the post-peak degradation of strength and stiffness in compression and tension as shown in Fig. 5.9. However, the *Pinching4* hysteretic model is not capable of accurately representing the unloading-reloading from tension to compression (path *h-c-d-a* in Fig. 5.1). This is because the *Pinching4* model requires that the maximum load along the reloading path occurs at point *a*, whereas the observed cyclic responses suggest that the maximum load in the segment *h-c-d-a* should occur at point *c*.

Strength and stiffness degradation were captured reasonably well by the calibrated hysteretic model. However, since the *Pinching4* model utilizes the same set of degradation coefficients irrespective of the loading direction, the model tends to under-predict and over predict the amount of degradation in compression and tension respectively (Fig. 5.9).

The hysteretic energy dissipated by the simulated response develops slower than the experiments as evidenced by Fig. 5.10. The difference stems largely from the inability of the *Pinching4* hysteretic model to approximate the unloading-reloading path from tension to compression. At the end of the tests, the average ratio of energy dissipated for the model to energy dissipated for the tests E_{model}/E_{Test} was 0.91 with a coefficient of variation of 0.09 (see Table 5.6). The objective of the hysteretic shape calibration described above was to minimize the error in dissipated energy while remaining on the conservative side of underestimating energy dissipation and associated hysteretic damping. Other criteria for calibration are

possible and may be considered in the future.

The performance of the expression for generalized backbones (Table 5.4) and *Pinching4* parameters (Table 5.5) is illustrated in Fig. 5.11. The modeled responses share the same characteristics described above for the responses modeled using parameters from Table 5.1 and Table 5.2. However, in some cases the generalized model could overestimate or underestimate the strength and damage accumulated by the member. This is a natural consequence of using values calibrated to a small data set. More points obtained from additional cyclic testing or finite element analysis would improve the calibration of the fitted coefficients and therefore the accuracy of the generalized expressions.

Table 5.6. Test and model hysteretic energy.

Specimen	E_{Test}	E_{Model}	E_{Model}/E_{Test}	Backbone Used [b]
	(kN-mm)		-	
600S137-97-GAC-1	16063	12010	0.75	1, 16
600S137-97-GAC-2	22983	20982	0.91	1, 16
362S137-68-GAC-1	14952	12465	0.83	4, 16
362S137-68-GAC-2	10009	9129	0.91	4, 16
600S137-68-DAC-1	8935	8697	0.97	6, 16
600S137-68-DAC-2	8960	8836	0.99	6, 16
362S137-68-DAC-1	6458	5845	0.91	8, 16
362S137-68-DAC-2	6368	5812	0.91	8, 16
600S162-33-LAC-1	2550	2408	0.94	10, 16
600S162-33-LAC-2	2344	2457	1.05	10, 16
362S162-54-LAC-1	3839	3244	0.85	11, 16
362S162-54-LAC-2	3773	3442	0.91	11, 16

(a) Backbone curve from Table 2

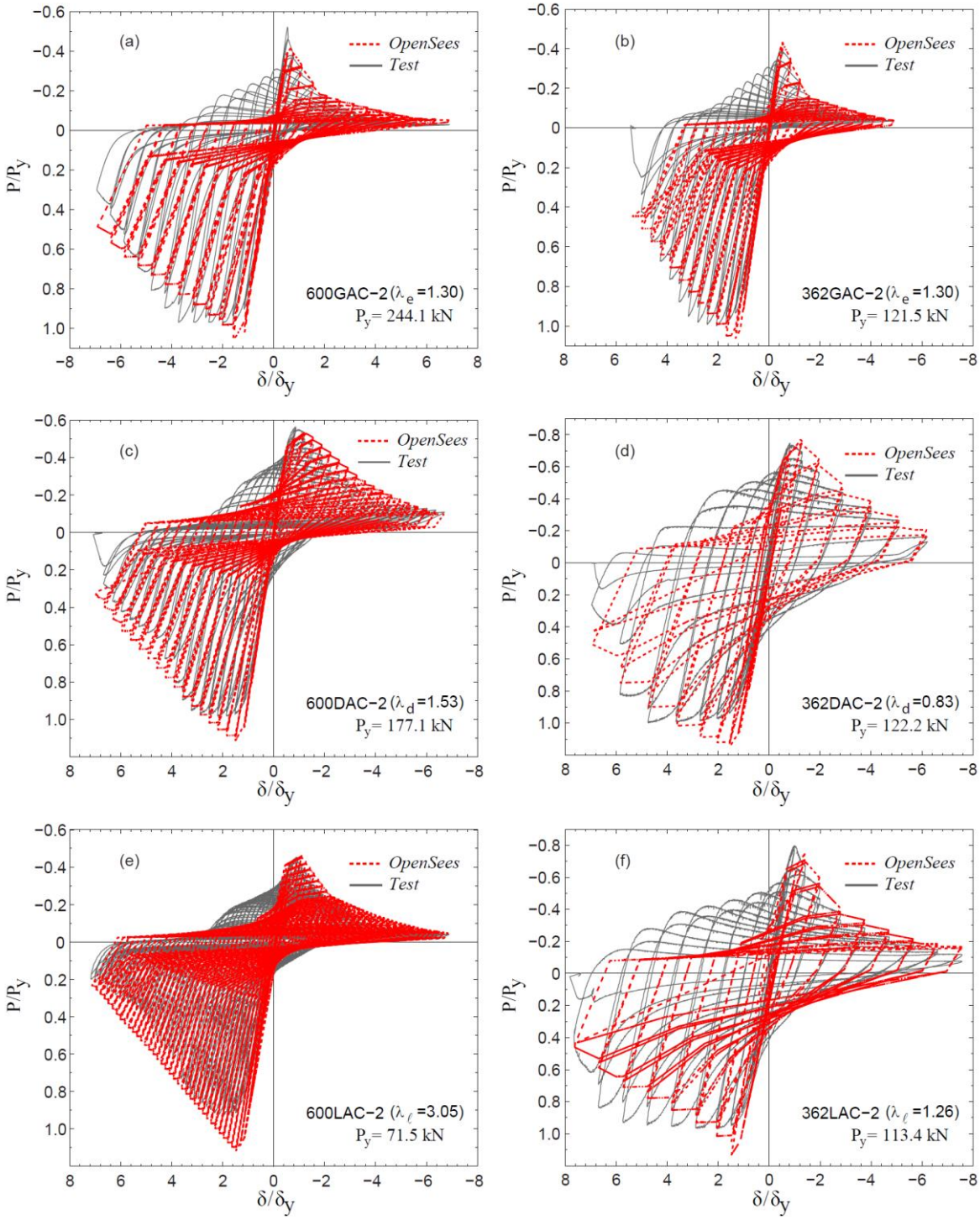

Fig. 5.9. Simulated axial response using *Pinching4*
(see Table 5.2 for r_D, r_F, and u_F values).

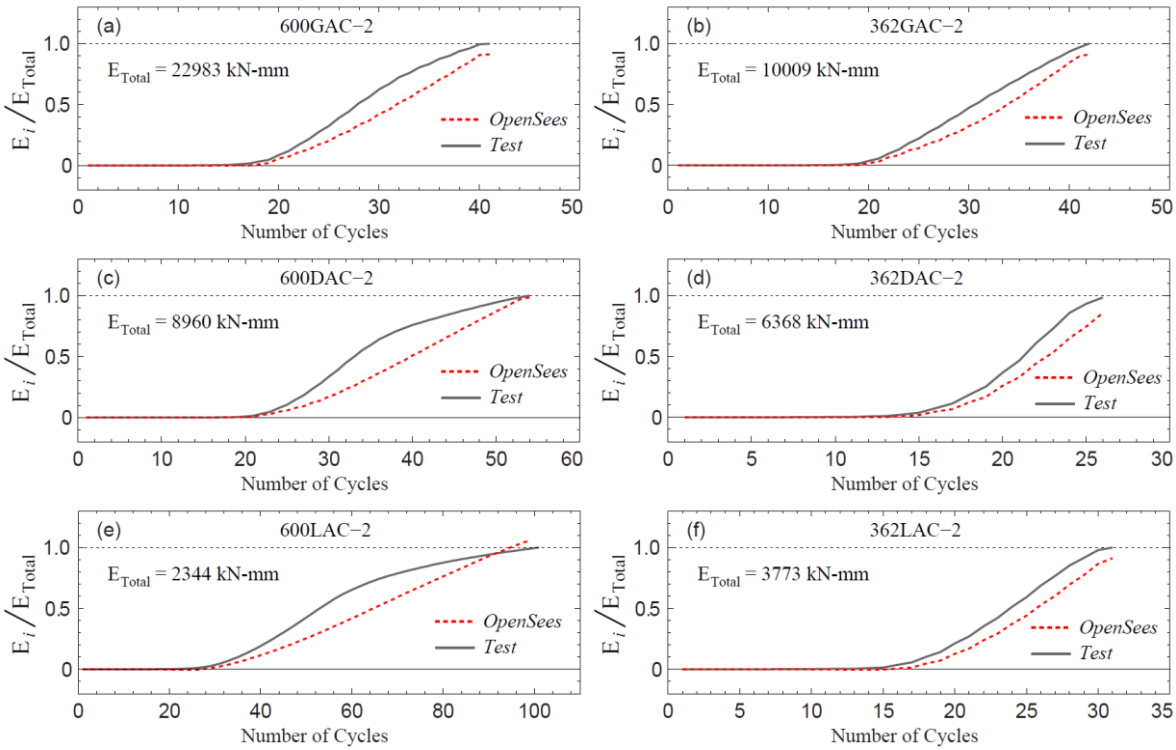

Fig. 5.10. Hysteretic energy comparison.

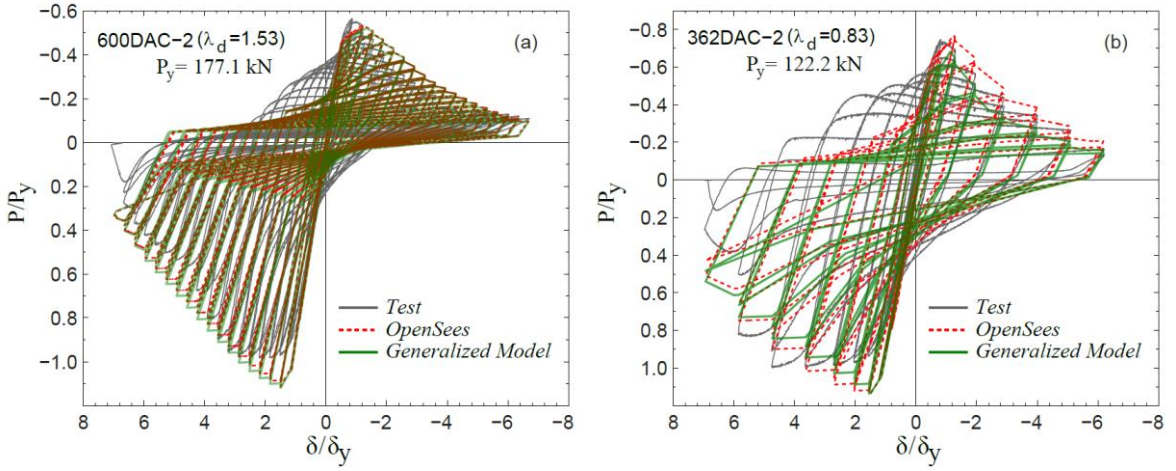

Fig. 5.11. Generalized model expressions comparisons.

6 Experiments on CFS Flexural Members

A testing program was conducted to study the cyclic response of CFS flexural members experiencing local, distortional and global buckling deformations. The study focused on members subjected to constant moment within the unbraced length, and interaction with shear or axial load was prevented through the boundary conditions provided. The testing program included twelve cyclic tests and twelve monotonic tests conducted on common CFS C-sections without perforations. Cyclic tests were conducted to determine the effects of reversed cyclic flexural loading and cumulative flexural deformation on damage and hysteretic energy dissipation. Monotonic flexural tests were performed to establish a moment-rotation envelope for comparison to the cyclic test response.

6.1 Specimen selection strategy

Specimens are selected such that their predicted monotonic flexural capacity is governed either by local, distortional or global buckling as predicted by the AISI Direct Strength Method [25]. The cross-sections considered were selected from standard sizes as listed in the Structural Stud Manufacturers Association catalog [26]. Cross-section dimensions and unbraced length (L_u) were varied to isolate each buckling limit state. Two different unbraced lengths were selected, a long unbraced length L_u=3048mm for global buckling, and a shorter unbraced length L_u=1626mm for distortional and local buckling. Three different web depths (305mm, 254mm and 203 mm) were selected. Two monotonic tests and two quasi-static cyclic tests were performed per specimen type. The test matrix is summarized in Table 6.1 (with nominal dimensions) and specimen nomenclature is explained in Fig. 6.1a.

Table 6.1. Test matrix with nominal dimensions and number of tests.

Specimen [(a)]	Buckling Limit [(b)]	L_u (mm)	H (mm)	B (mm)	t (mm)	No. of Cyclic Tests	No. of Monotonic Tests
800S200-33-LF#	Local	1626	203	51	0.88	2	2
1000S200-43-LF#	($\lambda_\ell >> \lambda_d$, λ_e)	1626	254	51	1.15	2	2
800S250-68-DF#	Distortional	1626	203	64	1.81	2	2
1200S250-97-DF#	$\lambda_d >> \lambda_\ell$ and λ_e	1626	305	64	2.58	2	2
800S162-97-GF#	Global	3048	203	41	2.58	2	2
1200S162-97-GF#	$\lambda_e >> \lambda_\ell$ and λ_d	3048	305	41	2.58	2	2

(a) F= Flexural, G= Global, D= Distortional, L= Local, # indicates Cyclic or Monotonic

(b) λ_ℓ, λ_d and λ_e = local, distortional and global slenderness parameter respectively (AISI 2007)

6.2 Specimen dimensions, material properties and elastic buckling moments

Cross-section dimensions were measured at the beam midspan using methods described in [27], see Table 6.2 and Fig. 6.1b. These values were utilized to calculate the elastic buckling moment for local buckling, $M_{cr\ell}$, distortional buckling, M_{crd}, and global buckling, M_{cre}, the associated half-wavelength for local and distortional buckling ($L_{cr\ell}$ and L_{crd} respectively) with finite strip eigen-buckling analysis in the CUFSM software [28]. The boundary conditions were assumed to be warping fixed between loading points when calculating the elastic buckling moments. Thus, an effective length of *0.5L* when calculating M_{cre} was considered. The yield moment, M_y, was determined using the cross-section moment of inertia area at mid-span and the average yield stress F_y obtained from three coupon tests per specimen. Coupon tests were conducted in accordance with ASTM E8M-04 [29] with one coupon taken from each flange and one from the web. The monotonic flexural capacity, M_n, was calculated using the AISI Direct Strength Method [25]. These values are summarized in Table 6.3.

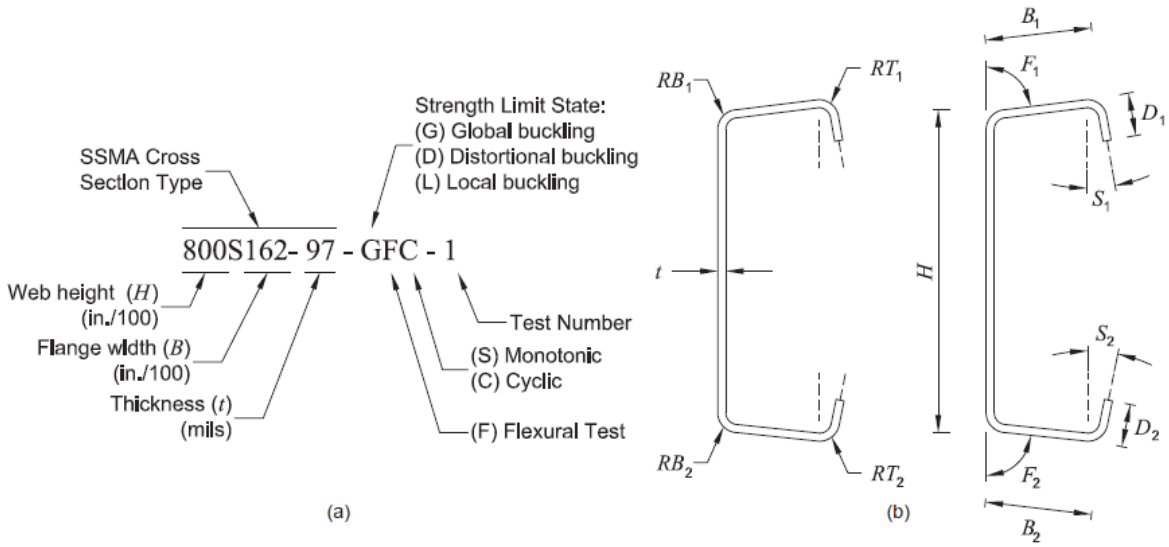

Fig. 6.1. Specimen naming notation (a); and cross-section dimension (b).

Table 6.2. Measured flexural specimen dimensions.

Specimen	L_u (mm)	A_g (mm^2)	D_1 (mm)	D_2 (mm)	B_1 (mm)	B_2 (mm)	H (mm)	RT_1 (mm)	RB_1 (mm)	RT_2 (mm)	RB_2 (mm)	F_1 (°)	F_2 (°)	S_1 (°)	S_2 (°)	t (mm)
1200S162-97-GFC-1	3048	995	9.8	11.3	42.5	43.1	305.7	4.8	5.6	5.2	5.6	91.2	88.0	-2.8	2.6	2.52
1200S162-97-GFC-2	3048	993	10.1	10.9	42.8	43.1	305.7	5.0	5.6	5.2	5.6	90.9	87.5	-2.8	3.0	2.51
1200S162-97-GFM-1	3048	991	10.0	11.1	42.3	43.2	305.9	4.8	5.6	5.2	5.6	91.2	88.2	-3.7	-3.1	2.51
1200S162-97-GFM-2	3048	992	10.8	10.0	42.8	42.0	305.7	5.2	5.6	4.8	5.6	88.7	90.7	2.5	-4.0	2.52
800S162-97-GFC-1	3048	734	9.7	11.4	42.9	42.5	203.9	4.4	5.6	5.2	5.2	90.6	88.8	-2.3	0.7	2.50
800S162-97-GFC-2	3048	734	12.4	13.0	40.6	40.2	203.9	5.0	5.4	5.2	5.4	90.3	88.8	0.5	2.1	2.50
800S162-97-GFM-1	3048	732	9.9	11.4	42.4	42.3	204.0	4.8	5.4	5.2	5.2	90.6	88.8	-2.7	-1.1	2.50
800S162-97-GFM-2	3048	735	12.2	13.6	40.3	39.9	203.8	4.8	5.4	5.2	5.2	89.0	87.7	0.7	2.1	2.51
1200S250-97-DFC-1	1626	1148	12.9	14.5	65.8	64.9	306.6	5.2	5.6	5.6	5.6	92.2	89.8	-4.2	-3.7	2.57
1200S250-97-DFC-2	1626	1140	12.6	14.5	65.1	65.7	306.5	5.2	5.6	5.6	5.6	91.4	89.5	-4.0	-4.1	2.56
1200S250-97-DFM-1	1626	1154	12.7	14.7	65.7	65.9	306.8	5.2	5.6	5.6	5.6	92.7	89.5	-5.3	-2.9	2.58
1200S250-97-DFM-2	1626	1148	12.8	14.7	66.0	66.4	306.8	5.2	5.6	5.6	5.6	92.0	89.7	-4.6	-5.7	2.56
800S250-68-DFC-1	1626	618	12.2	14.2	63.2	64.4	204.2	4.0	4.0	4.2	4.6	91.9	89.3	-5.3	-5.0	1.79
800S250-68-DFC-2	1626	615	14.6	11.5	63.8	63.0	204.2	8.7	4.8	4.2	4.0	90.6	90.5	-4.1	-4.1	1.80
800S250-68-DFM-1	1626	623	14.2	12.4	63.8	63.8	204.3	4.4	4.8	4.0	4.0	91.7	91.0	-3.2	-3.8	1.81
800S250-68-DFM-2	1626	625	14.4	12.1	65.0	63.7	204.1	4.4	4.4	4.2	4.0	90.6	90.6	-4.6	-4.1	1.81
1000S200-43-LFC-1	1626	418	10.2	11.8	49.2	50.3	254.0	3.6	3.2	3.6	3.6	89.6	87.0	1.0	0.9	1.14
1000S200-43-LFC-2	1626	422	10.3	12.0	49.1	50.1	254.4	3.6	3.2	3.6	3.6	90.5	86.8	0.7	2.0	1.15
1000S200-43-LFM-1	1626	422	10.3	12.0	49.2	50.2	254.5	3.6	3.2	3.6	3.6	90.4	87.4	0.2	1.1	1.15
1000S200-43-LFM-2	1626	424	10.1	12.0	49.2	50.3	254.4	3.6	3.2	3.6	3.6	90.8	87.2	0.3	1.5	1.16
800S200-33-LFC-1	1626	285	14.5	14.7	49.9	49.9	204.7	3.6	3.2	3.6	3.2	90.7	90.6	1.9	0.1	0.88
800S200-33-LFC-2	1626	302	14.0	14.1	52.8	50.2	203.7	3.6	3.2	4.4	3.2	90.1	90.5	-0.7	1.0	0.93
800S200-33-LFM-1	1626	286	14.5	15.2	49.5	49.9	204.5	3.6	3.2	3.6	3.2	91.5	88.9	-1.7	1.1	0.88
800S200-33-LFM-2	1626	287	14.7	14.7	50.0	49.3	204.7	3.6	3.0	3.6	3.4	90.7	89.6	-0.8	-0.2	0.88

Table 6.3. Elastic buckling properties and predicted compressive capacity.

Specimen	F_y (MPa)	F_u (MPa)	M_y (kN-mm)	M_n (kN-mm)	M_{cre} (kN-mm)	λ_e	M_{crd} (kN-mm)	λ_d	L_{crd} (mm)	$M_{cr\ell}$ (kN-mm)	λ_ℓ	$L_{cr\ell}$ (mm)	δ_e (×10^{-3}mm)
1200S162-97-GFC-1	448	574	32664	15524	15524	1.45	23387	1.18	252	28195	0.74	141	3871
1200S162-97-GFC-2	464	575	33835	15835	15835	1.46	23557	1.20	254	28379	0.75	141	3951
1200S162-97-GFM-1	451	566	32668	15272	15272	1.46	23276	1.18	252	28028	0.74	141	3830
1200S162-97-GFM-2	440	568	31850	16530	16530	1.39	24544	1.14	260	29561	0.75	139	4149
800S162-97-GFC-1	452	578	17786	10005	10006	1.33	24668	0.85	221	34810	0.54	92	6937
800S162-97-GFC-2	454	575	17752	9854	9854	1.34	27939	0.80	249	36219	0.52	92	6867
800S162-97-GFM-1	452	579	17711	9721	9721	1.35	24901	0.84	220	34704	0.53	92	6770
800S162-97-GFM-2	462	580	18182	9623	9623	1.37	27902	0.81	244	36195	0.52	92	6664
1200S250-97-DFC-1	411	537	38450	27721	208449	0.43	31050	1.11	376	39466	0.99	141	10537
1200S250-97-DFC-2	385	531	35914	26249	199162	0.42	30076	1.09	367	38276	0.97	141	10255
1200S250-97-DFM-1	389	530	36673	26845	206543	0.42	30839	1.09	370	39349	0.97	141	10393
1200S250-97-DFM-2	404	532	37977	27340	208425	0.43	30546	1.12	375	38865	0.99	141	10316
800S250-68-DFC-1	385	466	14292	10247	81992	0.42	11373	1.12	410	15650	0.96	117	14595
800S250-68-DFC-2	377	462	13833	10575	82729	0.41	13084	1.03	451	16544	0.91	113	16995
800S250-68-DFM-1	376	465	14007	10658	88723	0.40	13079	1.03	462	16680	0.92	113	16739
800S250-68-DFM-2	377	464	14148	10719	91237	0.39	13057	1.04	469	17022	0.91	113	16570
1000S200-43-LFC-1	424	478	12034	6056	36445	0.57	3997	1.74	363	3378	1.89	139	6037
1000S200-43-LFC-2	421	476	12047	6125	36989	0.57	4098	1.71	365	3443	1.87	139	6098
1000S200-43-LFM-1	418	479	11983	6114	37083	0.57	4110	1.71	365	3454	1.86	139	6111
1000S200-43-LFM-2	419	476	12045	6090	36932	0.57	4045	1.73	358	3468	1.86	140	6123
800S200-33-LFC-1	335	403	5550	3197	26252	0.46	3136	1.33	582	1797	1.76	109	6881
800S200-33-LFC-2	307	371	5377	3358	30191	0.42	3417	1.25	578	2184	1.57	109	7907
800S200-33-LFM-1	335	404	5575	3208	25679	0.47	3190	1.32	575	1799	1.76	110	6858
800S200-33-LFM-2	337	405	5632	3257	26365	0.46	3257	1.31	586	1843	1.75	109	7001

$\lambda_e = (M_v/M_{cre})^{0.5}$; $\lambda_d = (M_v/M_{crd})^{0.5}$; $\lambda_\ell = (M_{ne}/M_{cr\ell})^{0.5}$.

6.3 Test setup and instrumentation

Tests were conducted in four point bending to provide constant flexural moment along the unbraced length. The members span 4877mm from support to support and attached to the loading frame through a spreader beam that allow adjustment of the loading points to change the unbraced length L_u. Loading locations and end supports were detailed to accommodate upward and downward forces exerted by the actuator while allowing rotations. Round pins passing through slotted holes at the supports and one of the loading points at the height of the cross-section centroid prevent axial forces from developing in the specimen. Lateral braces were placed in the shear spans to develop longitudinal warping fixity at the loading points and ensured the desired unbraced length. Two LVDTs were utilized to measure the vertical displacement at the loading points. The average of the two displacements is used for control of the test through the customized control program. The specimens were subjected to a cyclic displacement history at a constant displacement rate derived such that the strain rate at the extreme fiber remains constant at 0.002 (mm/mm)/(min). The displacement rate for the monotonic tests was derived based on a constant strain rate at the extreme fiber of 0.00003 (mm/mm)/(min). The displacement rate for each type of specimen are listed in Table 6.4.

Table 6.4. Displacement rate.

Specimen	**Cyclic**	**Monotonic**
	(mm/min)	
800S200-33-LF#	20.565	0.349
1000S200-43-LF#	30.848	0.523
800S250-68-DF#	28.546	0.484
1200S250-97-DF#	42.820	0.726
800S162-97-GF#	34.256	0.581
1200S162-97-GF#	42.820	0.726

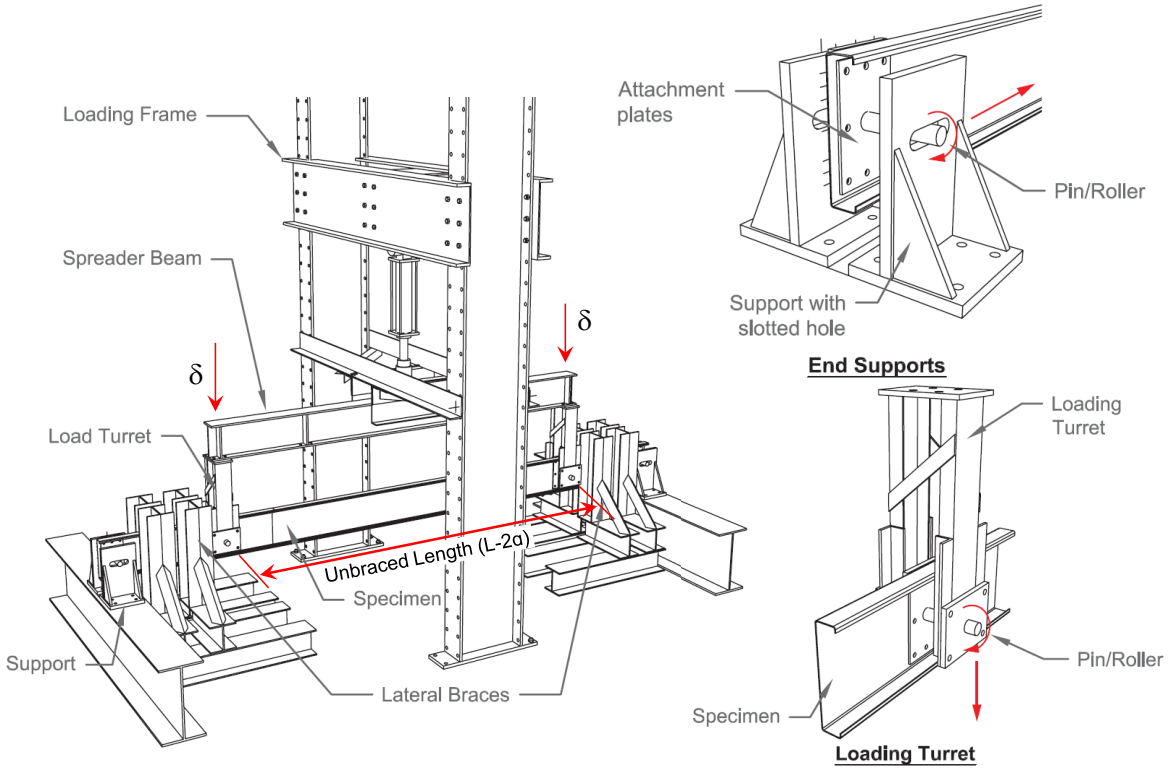

Fig. 6.2. Test setup with support and load point detail.

6.4 Loading Protocol

The loading protocol for cyclic testing of CFS flexural members is the same utilized for testing of axial members and is described in section 4.4. The anchor point δ_e in this case is the elastic displacement applied at the loading points corresponding to the moment M_e at which buckling deformations are expected to initiate. Linear elastic behavior is expected during the first six cycles before reaching δ_e. The anchor displacement is calculated as,

$$\delta_e = \frac{M_e a}{6EI}(3L - 4a) \qquad 6.1$$

where a = the distance from the centerline of the support to the loading point, and L=4877mm is the specimen span from centerline support to centerline support. The parameter M_e is calculated using slenderness limits defined in the AISI Direct Strength Method [25]. The DSM approach dictates that local buckling initiates at λ_ℓ=0.776 and the distortional buckling initiates at λ_d=0.673. Using $\lambda = (M_e/M_{cr})^{0.5}$, then M_e=0.60$M_{cr\ell}$ and M_e=0.45M_{crd}. The DSM approach dictates global buckling deformation initiates at M_e=0.36M_{cre}. Values of δ_e are listed in Table 6.3 for all specimens.

6.5 Experimental Results

Cyclic and monotonic moment-rotation ($M–\theta$) responses were obtained for specimens experiencing local, distortional, and global buckling limit states. Experimental values of the rotation at the loading point are calculated as $\theta=\delta/a$, where δ is the average of the displacements measured at the loading points. This approximation is consistent with lumped-spring models for CFS flexural members, e.g. [42]. Rotations are normalized to the elastic yield rotation, $\theta_y = M_y L_u/2EI$, at the loading point, which corresponds to the yield moment $M_y=SF_y$. Experimental values of the moment are calculated as $M=aP$, where P is half of the measured vertical load. Positive moment and rotations correspond to downward loading and the negative values correspond to upward loading. Members were loaded until the maximum stroke of the hydraulic actuator was reached or until the distance available to slide at the supports was max-out. In general all members were deformed to a maximum downward/upward displacement of at least 63mm. The following sections describe details of the monotonic and cyclic tests for each buckling limit state. Test videos are available on Virginia Tech's digital repository [39].

6.5.1 Monotonic flexural responses

Monotonic responses are shown in Fig. 6.3. The pre-peak responses are linear past 50% of the peak moment for all members and became nonlinear when buckling deformations appeared. The average ratio of test peak moment to predicted moment M_{max}/M_n was 0.98 with a coefficient of variation of 0.24 for all monotonic tests (see Table 6.6). The high COV is mostly related to the low test-to-predicted values (μ=0.68) observed for members experiencing global buckling (see Table 6.6). However, when considering only the local and distortional buckling specimens, the average test-to-predicted moment ratio under monotonic loading is 1.12 and coefficient of variation 0.09. These results demonstrate that the actual boundary conditions accurately represent the assumed constraints (i.e., warping fixed, k=0.5) at the loading points, and that the low test-to-predicted M_{max}/M_n for global buckling obey to other reasons. Sweep imperfections on the order of L/1495 were measured for the global buckling specimens and therefore it is expected that M_{max} should be less than M_{cre}. For local and distortional buckling members sweep imperfections were small and had minimal influence on the peak moment M_{max}. Buckling in all members started before the peak moment

and cross-section failure happened close to the mid-span (Fig. 6.4), with the exception of 800DFM-2 where failure occurred half way from the mid-span and the loading point (however this did not affected the moment-rotation response). Some additional details for each buckling member group are described next.

6.5.1.1 Global buckling members GFM

Global buckling members (GFM) exhibited lateral-torsional buckling that started before the maximum flexural strength M_{max}, see Fig. 6.4a. At peak moment, the top flange at intersection with the stiffening lip locally buckled inelastically and strength dropped rapidly to about 70% the peak-moment. The moment-rotation response stabilizes around $0.2M_y$ for both cross-section types (Fig. 6.3). Even though the top flanges buckled and are not contributing to the flexural-torsional stiffness, the member is still able to carry load for large deformations because the web and web-flange intersections experience compatibility-based membrane tension stiffening. Inelastic deformations developed close to the loading points as the second hinge formed in the later test stages.

6.5.1.2 Distortional buckling members DFM

Distortional members 800DFM exhibited distortional buckling of the top flange and top portion of the web with three half-waves similar to the ones showed in Fig. 6.4b. The top flange failed locally at the maximum strength M_{max} and strength dropped instantly to 65% the peak moment. Inelastic strains accumulated around the failed cross-section and the section folded into itself as deformations increased. Out of plane deformations similar to lateral torsional buckling were not observed and no hinges formed close to the loading points.

Distortional members 1200DFM, experienced buckling of the top portion of the web and flanges with four half-waves as seen in Fig. 6.4b. The top flange failed locally at the maximum strength M_{max} and strength dropped instantly to 75% the peak moment (Fig. 6.3). The post peak behavior resembled lateral torsional buckling with large out of plane deformation. Inelastic deformations developed close to the loading points as the second hinges formed in the later stages of the test with strength degrading to values also around $0.3M_y$.

6.5.1.3 Local buckling members LFM

Local members 800LFM exhibited buckling of the top portion of the web with 14 half-waves before the maximum flexural strength M_{max}. At peak moment, the top part of the web close to the junction to the flange, yielded and the mid cross-section collapsed (Fig. 6.4c) accompanied by an instant drop of the strength, to 50% the peak moment. The strength then degraded slowly and stabilized around $0.2M_y$ (Fig. 6.3). After the mid-span cross-section buckled the response resembled lateral torsional buckling and started deforming in the out of plane direction. Even though the web buckled at the mid-span cross-section, the member still carried load at large deformations due to the compatibility-based membrane tension stiffening at the web and web-flange intersections. Inelastic deformations developed close to the loading points as the second hinges formed in the later test stages.

Local members 1000LMF exhibited local buckling of the top portion of the web with about eight half-waves in the early cycles, and this quickly changed to distortional buckling with four half-waves in the top flange before the maximum flexural strength M_{max}. These members had stiffening lips shorter than the nominal values (compare nominal 15.8mm to the measured 10.2mm). Because of the shorter lips, the average predicted capacity by DSM M_{nd} =6096*kN-mm* was less than $M_{n\ell}$ =6624*kN-mm* and this was reflected in the buckling mode observed. At peak moment, the top flange locally buckled and strength dropped instantly to 65% of M_{max}. The post peak behavior resembled the behavior of the 800LMF members with large deformations and strength degrading slowly to values also around $0.2M_y$.

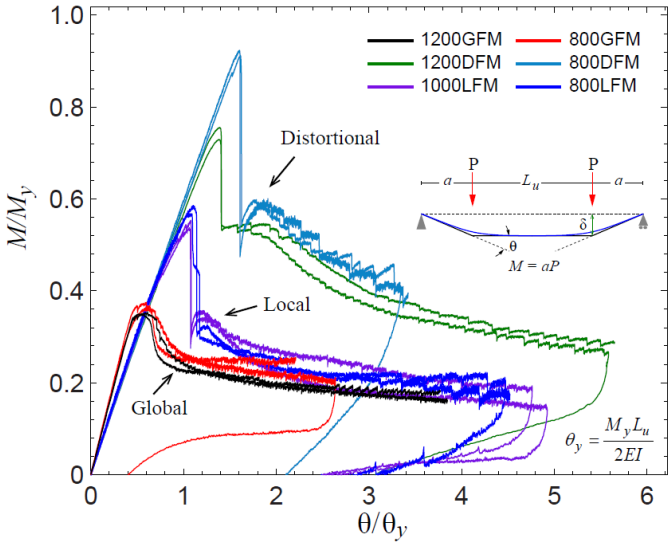

Fig. 6.3. Monotonic flexural responses.

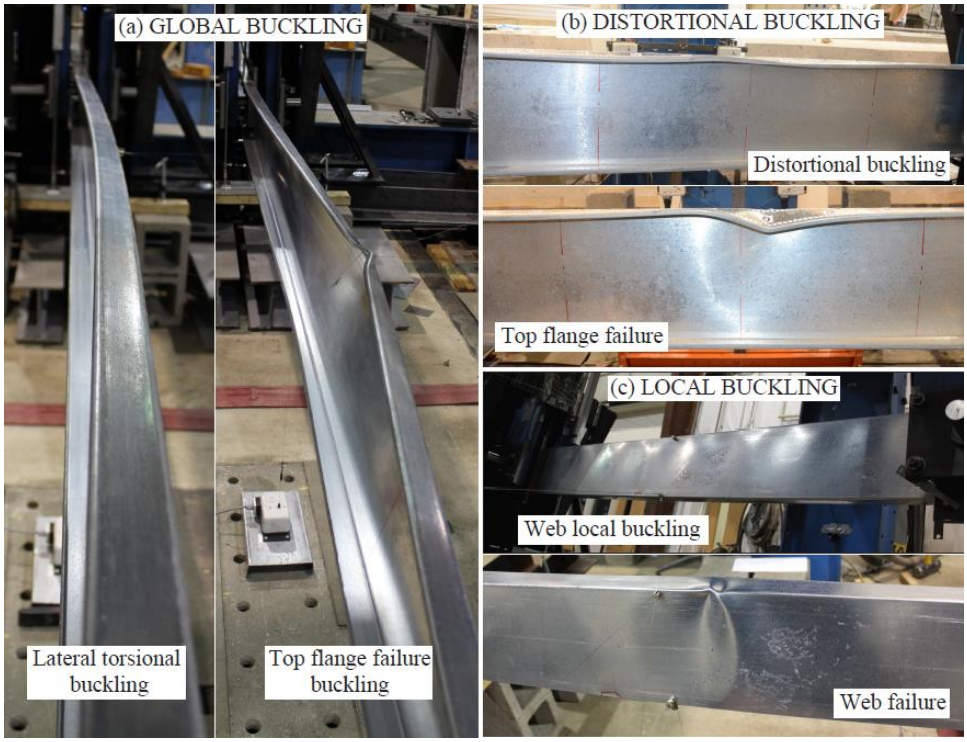

Fig. 6.4. Buckling modes, (a) lateral torsional buckling;
(b) distortional buckling; (c) local buckling.

Table 6.5. Test maximum moments.

Specimen	M_{max}	M_{min}	θ_{Mmax}	θ_{Mmin}	θ_y	M_{max}/M	M_{min}/M_n	θ_{Mmax}/θ_y	θ_{Mmin}/θ_y
	(kN-mm)			(×10-3rad)					
1200S162-97-GFC-1	10291	-10448	13	-13	23	0.66	0.67	0.57	-0.56
1200S162-97-GFC-2	11270	-11256	12	-11	24	0.71	0.71	0.50	-0.45
1200S162-97-GFM-1	11503	-	13	-	23	0.75	-	0.55	-
1200S162-97-GFM-2	11306	-	14	-	23	0.68	-	0.61	-
800S162-97-GFC-1	6903	-6632	20	-20	35	0.69	0.66	0.58	-0.58
800S162-97-GFC-2	7065	-6773	21	-20	35	0.72	0.69	0.59	-0.57
800S162-97-GFM-1	6499	-	21	-	35	0.67	-	0.59	-
800S162-97-GFM-2	6906	-	21	-	36	0.72	-	0.59	-
1200S250-97-DFC-1	28504	-29078	17	-16	12	1.03	1.05	1.44	-1.34
1200S250-97-DFC-2	28121	-28591	16	-16	11	1.07	1.09	1.48	-1.42
1200S250-97-DFM-1	26885	-	16	-	11	1.00	-	1.39	-
1200S250-97-DFM-2	28849	-	16	-	12	1.06	-	1.39	-
800S250-68-DFC-1	12028	-13407	23	-26	17	1.17	1.31	1.40	-1.55
800S250-68-DFC-2	13243	-11175	26	-22	16	1.25	1.06	1.61	-1.33
800S250-68-DFM-1	13068	-	26	-	16	1.23	-	1.61	-
800S250-68-DFM-2	12991	-	26	-	16	1.21	-	1.61	-
1000S200-43-LFC-1	6389	-7182	14	-15	15	1.05	1.19	0.97	-1.05
1000S200-43-LFC-2	6941	-7423	16	-16	15	1.13	1.21	1.08	-1.11
1000S200-43-LFM-1	6706	-	16	-	14	1.10	-	1.07	-
1000S200-43-LFM-2	6553	-	15	-	15	1.08	-	1.06	-
800S200-33-LFC-1	3490	-3326	16	-15	15	1.09	1.04	1.12	-1.01
800S200-33-LFC-2	3211	-3473	14	-14	12	0.96	1.03	1.15	-1.14
800S200-33-LFM-1	3353	-	16	-	15	1.05	-	1.10	-
800S200-33-LFM-2	3298	-	15	-	15	1.01	-	1.04	-

M_{max},θ_{Mmax}= maximum moment and corresponding rotation; M_{max},θ_{Mmax}= minimum moment and corresponding rotation; $\delta_y = M_y L_u / 2EI_x$, the elastic yielding rotation.

Table 6.6. Test-to-predicted statistics.

Specimen	M_{max}/M_n		M_{min}/M_n		θ_{Mmax}/θ_y		θ_{Mmin}/θ_y	
Group	μ	cov	μ	cov	μ	cov	μ	cov
Global	0.70	0.04	0.68	0.03	0.57	0.06	0.54	0.11
Distortional	1.13	0.09	1.13	0.11	1.49	0.07	1.41	0.07
Local	1.06	0.05	1.12	0.08	1.07	0.05	1.08	0.05
L & D	1.09	0.08	1.12	0.09	1.28	0.18	1.24	0.19
Cyclic	0.96	0.22	0.98	0.24	1.04	0.40	1.01	0.38
Monotonic	0.96	0.21	-	-	1.05	0.38	-	-
All Spec.	0.96	0.21	0.98	0.24	1.05	0.37	1.01	0.38

μ= mean value; cov= coefficient of variation; L&D= Local and Distortional

6.5.2 Cyclic flexural responses

For all members, the cyclic response started as linear elastic past the first six cycles with equal stiffness in both loading directions (see, Fig. 6.5a, Fig. 6.9a, and Fig. 6.7a). Buckling deformations started after cycle 10 in the same fashion as for the monotonic members and as illustrated in Fig. 6.4 to Fig. 6.7. The buckled cross-section in general occurred at different locations when loading upwards than when loading downwards due to

redistribution of stresses around the first collapsed cross-section. Despite this, the cyclic response was symmetric for most of the members as expected with three exceptions described below. The average ratio of test peak moment to predicted moment for cyclic tests was 0.96 (*cov*=0.22) and 0.98 (*cov*=0.24) for positive and negative moment respectively. The large variations are caused by the low test-to-predicted ratio for global buckling members. When considering the local and distortional buckling members only, the ratios improved to 1.09 (*cov*=0.08) and 1.12 (*cov*=0.09) for positive and negative moment respectively. Sweep imperfections on the order of *L*/1495 are the reason low M/M_n values for global buckling members and thus maximum strength should be less than the predicted values M_{cre}. Sweep imperfections were negligible for the local and distortional members and had minimal influence on the peak moment. Some additional details for each buckling member group are described next.

6.5.2.1 Global buckling members GFC

Global buckling members (GFC) exhibited lateral torsional buckling as described for their monotonic counterparts and illustrated in Fig. 6.4a and Fig. 6.5d. Strength decreased rapidly after the peak to about 65% M_{max}, then continued to degrade slowly. The moment-rotation response stabilized around $0.2M_y$ for both cross-section types, an interesting result important to seismic design, see Fig. 6.5c. Even though the flanges have buckling and are not contributing to the flexural-torsional stiffness, the members are still able to carry load for large deformations because of redistribution of the stresses towards the loading supports through the web and web-flange intersections compatibility-based membrane tension stiffening. Pinching of the response (Fig. 6.5b) occurred because upon unloading the member straightened out (towards the unbuckled initial position) before starting to load in the opposite direction. Damage due to inelastic strains accumulated at the buckled flanges close to the stiffening lips which led to tearing during the last cycles. This tearing did not propagated to the flanges. When comparing the cyclic response to the monotonic responses, it appears that strength degradation due to cyclic loading is minimal as evidence by the small gap between the monotonic curves and the cyclic responses in Fig. 6.6. Strength and stiffness degradation are characterized and described in section 7.2.

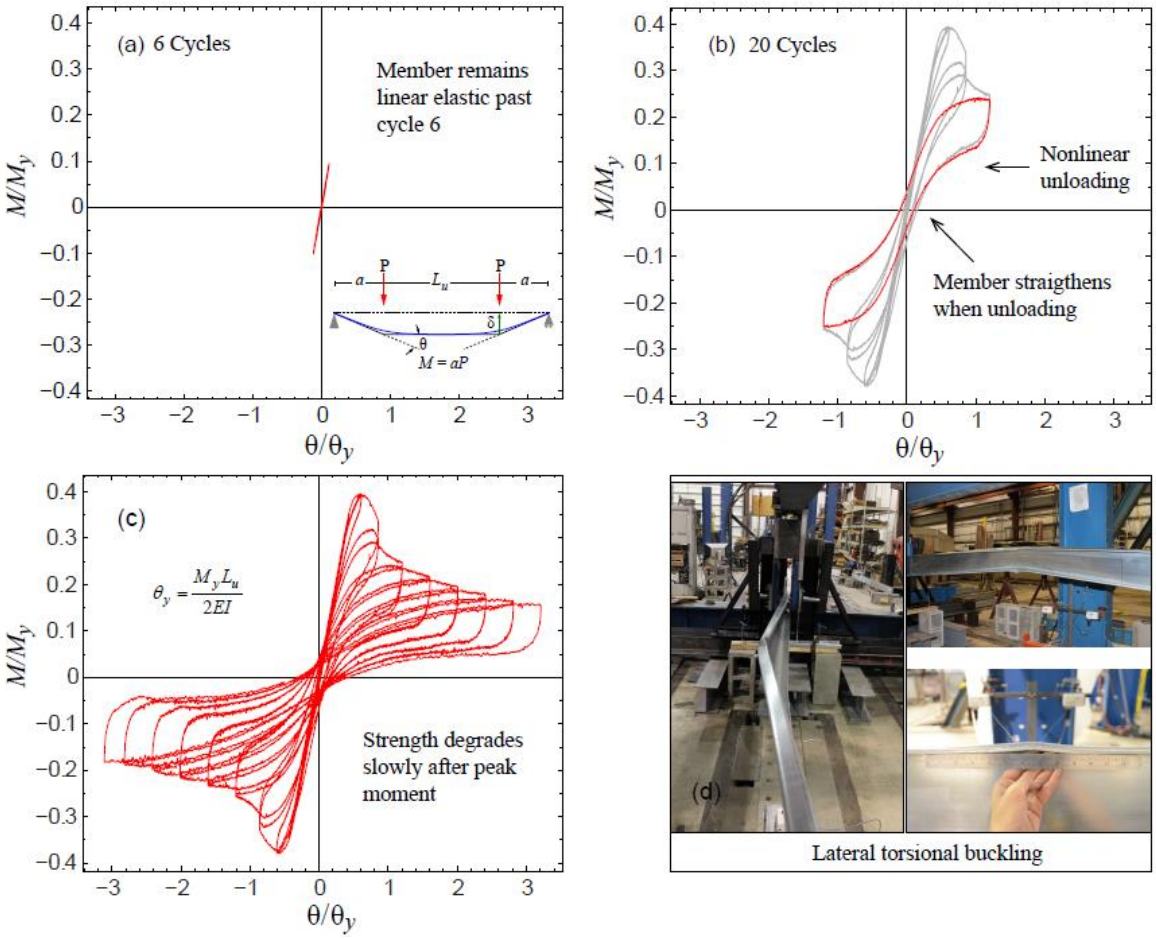

Fig. 6.5. Cyclic moment-rotation response specimen 800S162-97-GFC-2,
(a) 6 cycles, (b) 20 cycles, (c) complete response, (d) failure mode.

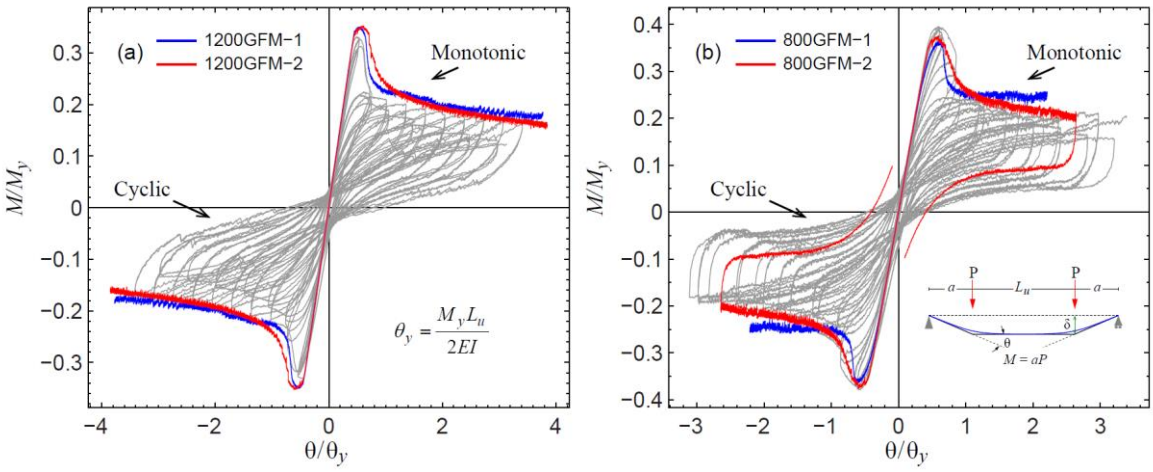

Fig. 6.6. Global buckling monotonic response envelope, (a) 1200 series, (b) 800 series.
(Monotonic responses are mirrored in the negative quadrant for comparison)

6.5.2.2 Distortional buckling members DFC

Distortional buckling members (DFC) exhibited distortional buckling of the top flange as described for their monotonic counterparts and illustrated in Fig. 6.4b and Fig. 6.7d. Strength dropped instantly after the peak moment to about 60% and 70% of the peak for the 800DFC and 1200DFC members respectively. Strength then degraded as the inelastic deformations accumulated at the buckled flanges evidenced by the gap between the monotonic curves and cyclic envelopes in Fig. 6.8. Stiffness degraded with every cycle as well (see section 7.2). Slight pinching of the response occurred upon unloading because the buckled flange tried to straighten before loading started in the opposite direction (Fig. 6.7b). The response of the 1200DFC members was highly symmetric with collapse of the cross-section after buckling happening at the mid-span, and large deformations are observed while carrying moments around $0.2M_y$ (Fig. 6.7c). Damage also accumulated close to the loading points for the 1200DFC as hinges formed in the last cycles resembling lateral torsional-buckling. The response of the 800DFC members on the other hand, was slightly asymmetric because the collapsed cross-section after buckling occurred at two different locations, at the mid-span for positive moment and close to the loading point for negative moment. This ultimately affected their post-peak behavior which consisted of folding of the buckled cross-section without formation of secondary additional hinges.

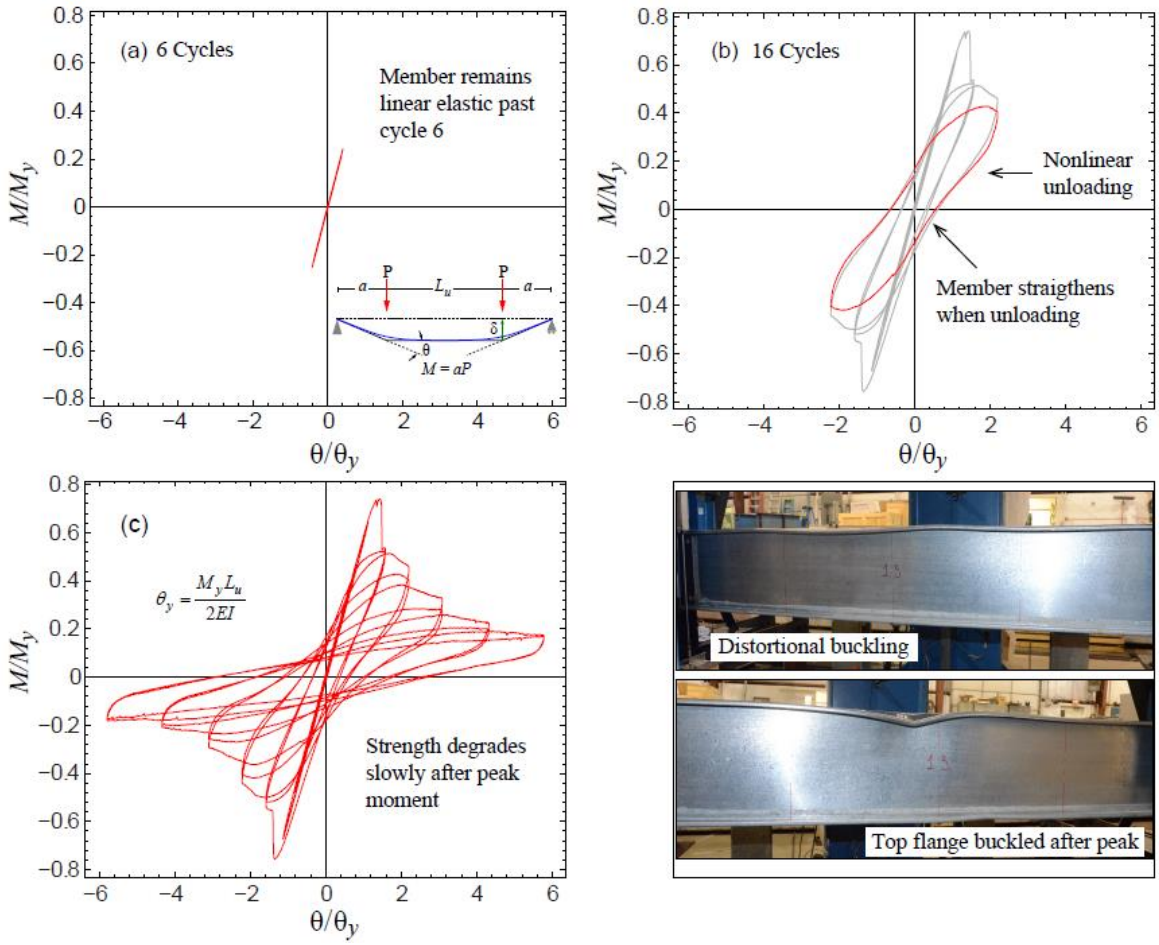

Fig. 6.7. Cyclic moment-rotation response specimen 1200S250-97-DFC-1,
(a) 6 cycles, (b) 16 cycles, (c) complete response, (d) failure mode.

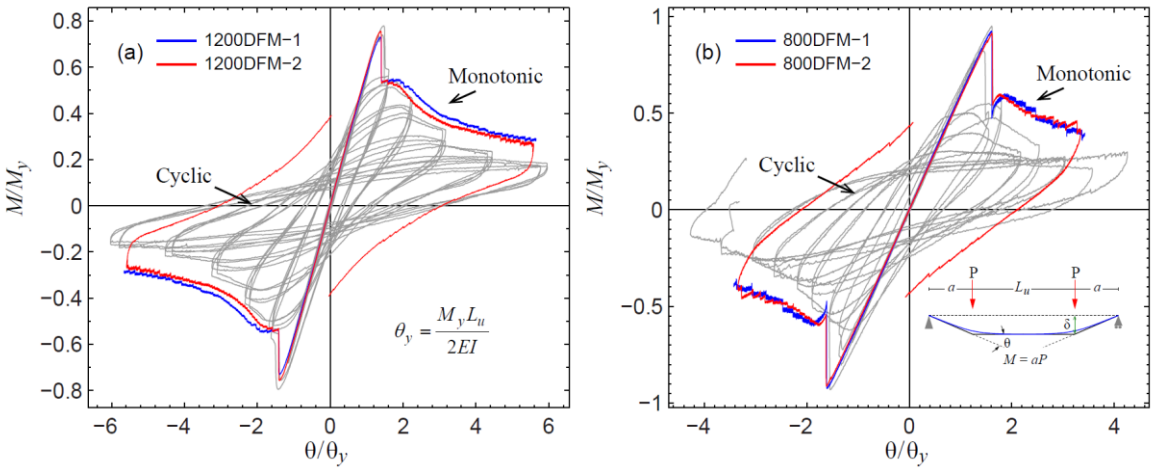

Fig. 6.8. Distortional buckling monotonic response envelope, (a) 1200 series, (b) 800 series.
(Monotonic responses are mirrored in the negative quadrant for comparison)

6.5.2.3 Local buckling members LFC

Local buckling members (800LFC) exhibited web local buckling as described for their monotonic counterparts and illustrated in Fig. 6.4c and Fig. 6.9d. Strength dropped instantly after the peak moment to about 40% of M_{max}, then degraded as the inelastic deformations accumulated at the top part of the web close to the junction to the flange. Slight pinching of the response occurred upon unloading because the member straightened before loading start loading in the opposite direction (Fig. 6.9b). The response of the 800LFC-1 member was symmetric with collapse of the cross section after buckling happening at the mid-span, and endured large deformations while still carried moments around $0.1M_y$ (Fig. 6.9c). Damage also accumulated close to one of the loading points for this member. The response of member 800LFC-2 shown in Fig. 6.10b, was similar to 800LFC-1 however, the cross-section at the only hinge folded into itself as deformations increased providing stiffness and a gain in strength in both directions in the last cycles.

Local buckling members (1000LFC) exhibited local buckling of the web before peak load that quickly shift to distortional buckling as described for their monotonic counterparts. These members had also stiffening lips shorter than the nominal values (compare nominal 15.8mm to the measured 10.3mm). Strength dropped instantly after the peak moment to about 55% of M_{max} and then degraded as deformations accumulated at the mid span and in later cycles close to the loading points. The response of 1000LFC-2 member was asymmetric because of the different direction the out of plane deformations took for positive moment and negative moment. The out of plane deformations in the positive moment direction favored higher strengths because of compatibility-based membrane tension stiffening. This stiffening effect was not present in the negative moment direction because the bottom flange buckled close to the loading supports forming additional hinges.

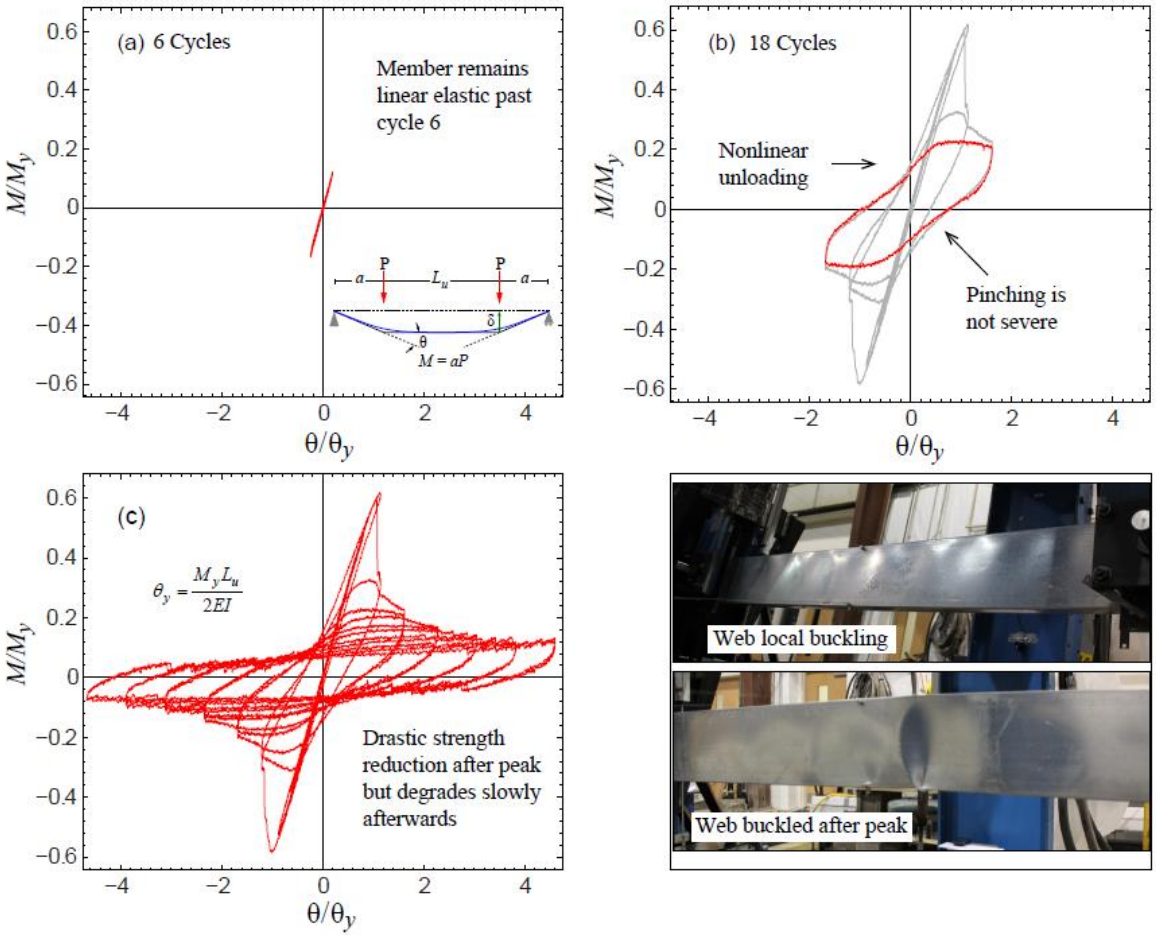

Fig. 6.9. Cyclic moment-rotation response specimen 800S200-33-LFC-1,
(a) 6 cycles, (b) 18 cycles, (c) complete response, (d) failure mode.

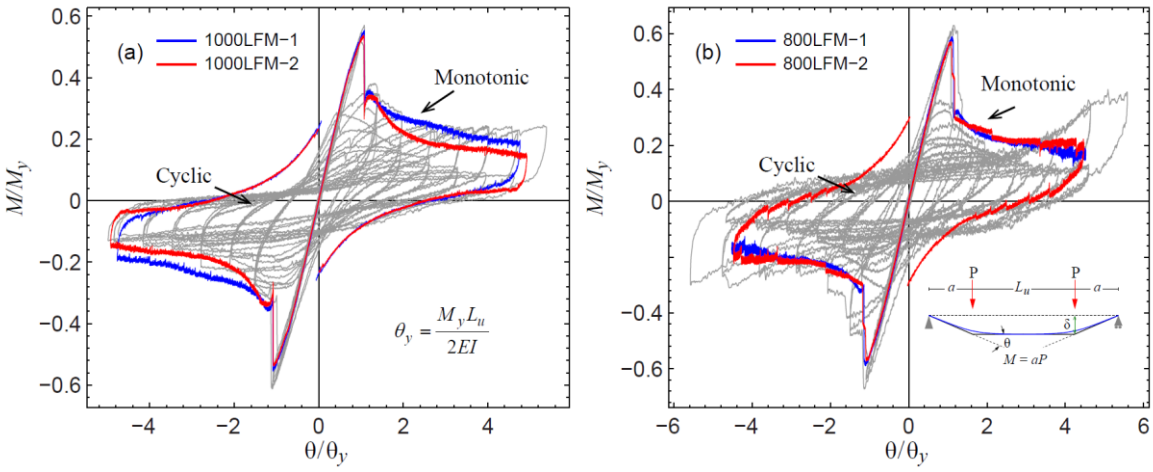

Fig. 6.10. Local buckling monotonic response envelope, (a) 1000 series, (b) 800 series.
(Monotonic responses are mirrored in the negative quadrant for comparison)

6.5.3 Moment-rotation response comparisons

Comparing the hysteretic response across limit states are challenging because of the different cross-sections, specimen lengths, and buckling failure modes considered in this study. The amount of strength degradation, stiffness degradation, and pinching of the hysteretic response varies for the different specimens; however, the behavior is similar across the different buckling modes, unbraced lengths and cross-sections considered. Fig. 6.11 compares the normalized envelopes of the hysteretic response of all the specimens in this study. It can be seen that all the specimens have the same normalized pre-buckling stiffness k/k_e ($k_e=6EI/[3L_u+2a]$). Strength decreased significantly after the peak moment, at least 35% of M_{min} or M_{max}, and degraded at different rates as the flexural deformation θ/θ_y increased ($\theta_y=M_y/k_e$). The moment for all members decreased to an average $0.2M_y$ in both loading directions while enduring large flexural deformations ($\theta/\theta_y \geq 2.5$), an interesting result important for seismic design. Pinching of the hysteretic response is less for distortional and local buckling members than it is for the global buckling members. Such difference correlates to the failure mechanism (i.e., twist at the mid-span) of the global buckling members, which upon unloading straightens, overcoming the torsional displacements involving rigid body motion of the cross-section.

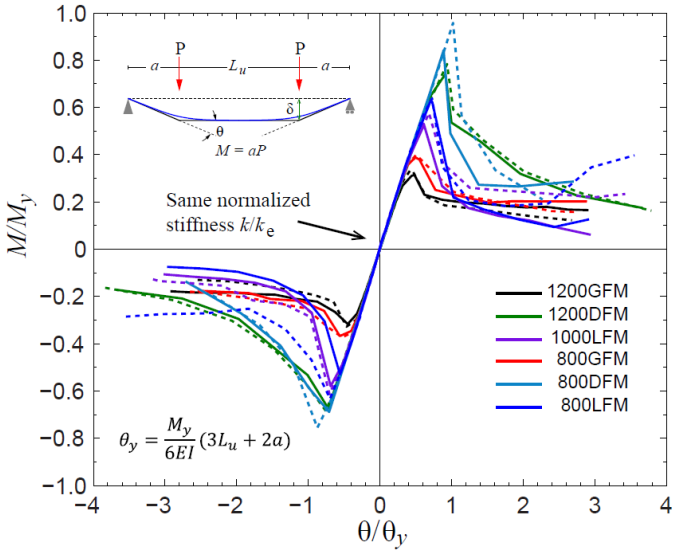

Fig. 6.11. Cyclic *M-θ* response envelopes.

6.6 Energy Dissipation of CFS Flexural Members

Energy dissipation is different for global buckling members (GFC) than for local and distortional specimens. Fig. 6.12 compares the normalized energy dissipated per cycle as a function of the cumulative flexural deformation $\Sigma\theta/\theta_y$. The hysteretic energy dissipated in each cycle E_{ci} is normalized to the area of the rectangle E_{cr} bounded by the maximum and minimum flexural deformation experienced in that cycle and the predicted strength M_n (see inset in Fig. 6.12). Global buckling members dissipate less energy every cycle than local or distortional members. The amount of pinching of the moment-rotation response which was more in the GFC members translated to less energy dissipated per cycle as shown in Fig. 6.12. However, energy dissipation capabilities remain constant for GFC members with increasing flexural deformations. Local and distortional buckling member energy dissipation capabilities instead decreases as flexural deformations increases. This difference is related to the failure mechanism and how damage accumulated after peak moment at the failed cross-sections and along the unbraced length. Damaged in global members was concentrated in the buckled flanges at the mid-span for most of the cycles and close to the loading points at the final cycles when the second hinges formed. In local and distortional buckling damaged initially accumulated at the compression portion of the cross section (web/flange) and quickly spread across the cross section creating yield lines and folding with every cycle. Because in global buckling members damage did not involve the web and yield lines or folding were absent, the energy dissipation capabilities remained constant.

The cumulative energy dissipated is similar for all GFC members for different values of cumulative flexural deformation, see Table 6.7. This trend is expected because the global slenderness of all GFC specimens are similar, compare $M_{cre}=0.55M_y$ for the 800S specimens versus $M_{cre}=0.47M_y$. Similar member slenderness values should produce similar magnitudes of energy dissipation based on the observations from the axial tests, see section 4.7 and [39] (Padilla-Llano et. al., 2012). However, this observation only applies if most damage accumulates at only one location as it was the case of global buckling. In the case local (LFC) and distortional (DFC) buckling members the damage accumulated in more than one location, and therefore the amounts of energy dissipation vary for the same $\Sigma\theta/\theta_y$ values despite having similar cross-sectional slenderness (Table 6.7) . For instance, the DFC have

similar λ_ℓ values, but damage in the 800DFC members accumulated at two different locations whereas in the 1200DFC the damage accumulated mostly at the mid-span.

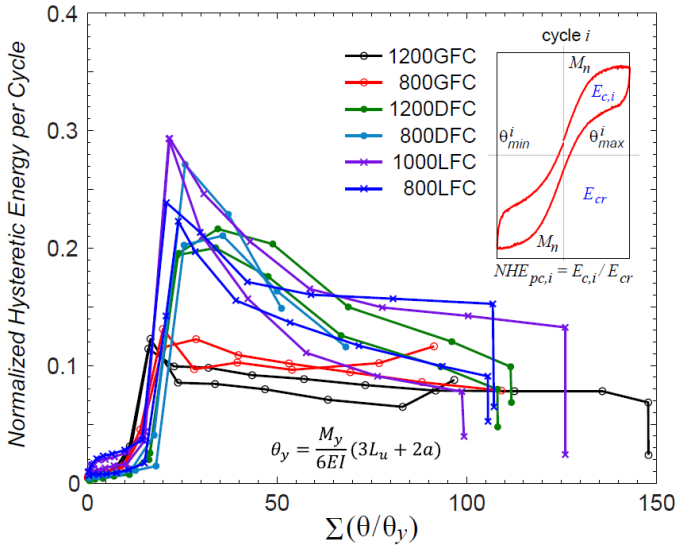

Fig. 6.12. Normalized hysteretic energy per cycle vs. cumulative flexural deformation

Table 6.7. Hysteretic energy dissipation for flexural members.

Specimen	HE_{10}	HE_{20}	HE_{40}	HE_{80}	HE_T	HE_{10}/L_{cr}	HE_{20}/L_{cr}	HE_{40}/L_{cr}	HE_{80}/L_{cr}	HE_T/L_{cr}	$max\ \Sigma\theta/\theta_y$
	(kN-mm)					(kN-mm/mm)					
1200S162-97-GFC-1	41	306	982	2255	4258	0.03	0.20	0.64	1.48	2.79	148
1200S162-97-GFC-2	34	296	879	1960	2497	0.02	0.19	0.58	1.29	1.64	97
800S162-97-GFC-1	30	276	965	2279	2811	0.02	0.18	0.63	1.50	1.84	91
800S162-97-GFC-2	31	238	939	2291	3196	0.02	0.16	0.62	1.50	2.10	109
1200S250-97-DFC-1	31	165	2003	4690	6038	0.08	0.44	5.32	12.46	16.04	108
1200S250-97-DFC-2	19	132	1781	4518	6098	0.05	0.36	4.86	12.32	16.62	112
800S250-68-DFC-1	17	56	1212	-	2537	0.04	0.14	2.95	-	6.18	68
800S250-68-DFC-2	22	126	1413	-	2019	0.05	0.28	3.13	-	4.48	51
1000S200-43-LFC-1	17	135	677	1251	1460	0.05	0.37	1.86	3.45	4.02	99
1000S200-43-LFC-2	27	150	774	1663	2530	0.07	0.41	2.12	4.56	6.94	126
800S200-33-LFC-1	4	37	289	649	835	0.04	0.34	2.64	5.94	7.65	106
800S200-33-LFC-2	15	76	330	755	1028	0.14	0.70	3.03	6.95	9.45	107

HE_{xx} = cumulative hysteretic energy dissipated up to $\Sigma\theta/\theta_y$ = xx; HE_T = cumulative hysteretic energy dissipated end of test. $\max(\Sigma\theta/\theta_y)$ = cumulative deformation at the end of the test.

7 Hysteretic Model for CFS Flexural Members

A hysteretic model for cold-formed steel flexural members is defined in similar fashion as done for the axial members in section 5. The hysteretic model Hysteretic model should accurately simulate the behavior of CFS flexural members, including strength and stiffness degradation, as well as, pinching of the moment-rotation curve. Characterization of the cyclic response is pursued herein using the uniaxial material model *Pinching4* [40] as implemented in OpenSees [41]. The model (shown in Fig. 7.1) is defined by a symmetric backbone curve, unloading-reloading paths that account for pinching, and a damage model for strength and stiffness degradation. The backbone curves are derived from normalized monotonic responses and the damage model for strength and stiffness deterioration is calibrated by comparing the monotonic and cyclic responses. The calibration procedure is the same described in section 5 for axial members with some modifications described in the following sections.

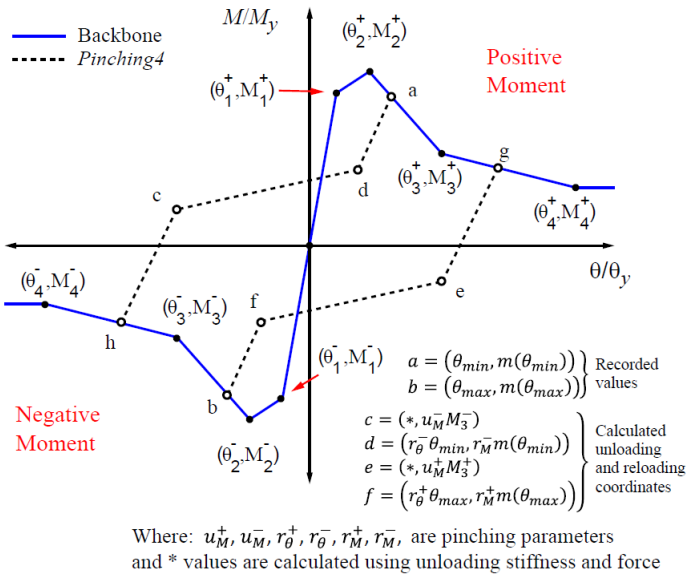

Fig. 7.1. *Pinching4* uniaxial material model.

7.1 Monotonic Response Characterization – Backbone

Backbone curves were fit to the monotonic test data using a combination of defined anchor points and fit values to match the energy represented by the area under the monotonic load-deformation curve. The backbone consists of load and displacement coordinates,

labeled as θ_i, M_i in Fig. 7.1, for eight unique points, four for positive moment, and four for negative moment. It is noted that the backbone characterization is conducted in normalized coordinates (θ/θ_y, and M/M_y) to allow more direct comparison between specimens and to facilitate application of the hysteric parameters to different configurations. The anchor points of the backbone for positive and negative moment were set at points (θ_2,M_2) and (θ_4,M_4). Point (θ_2,M_2) as shown in Fig. 7.1 was fixed to the point of maximum normalized moment and corresponding normalized rotation. Point (θ_4,M_4) was fixed based on an flexural deformation $\theta = 2\theta_y$ and associated moment. This point corresponds to post-peak strength loss of at least 40% for all tested specimens and a zero-slope is assumed beyond this point. The remaining values were selected using a least squares method to minimize the error between the energy dissipated in the monotonic tests and the energy dissipated by the multi-linear model. The fit was performed separately for pre-peak and post-peak energy to prevent over or under compensation of the dissipated energy [42]. Additional constraints were utilized to encourage the model backbone to resemble the experimental curve.

Two segments prior to the peak load were used to capture the elastic and pre-buckling nonlinearities in the response. Two post-peak segments with negative slope were included to account for the softening and post-peak strength loss as observed from the tests. Point (θ_3,M_3) was constrained to be slightly to the right/left of point (θ_2,M_2) for distortional and local members to avoid convergence problems caused by a close to infinity slope. The coordinates defining the fitted backbones are summarized in Table 7.1. The obtained points are used to establish the backbone for both sides of the moment-rotation hysteretic model.

Table 7.1. Backbone definition points for each specimen.

	Specimen	M_y	k_e [(a)]	θ_y [(b)]	θ_1/θ_y	θ_2/θ_y	θ_3/θ_y	θ_4/θ_y	M_1/M_y	M_2/M_y	M_3/M_y	M_4/M_y	k_1/k_e	k_2/k_e	k_3/k_e	k_4/k_e
		(kN)	(MN/mm)	(rad $\times 10^{-3}$)										$\times 10^{-3}$		
1	1200S162-97-GFM-1	32668	1193.1	27.38	0.328	0.443	0.631	2.000	0.314	0.349	0.237	0.193	960	303	-594	-32
2	1200S162-97-GFM-2	31850	1192.2	26.72	0.325	0.515	0.761	2.000	0.317	0.352	0.236	0.185	976	185	-473	-41
3	800S162-97-GFM-1	17711	429.6	41.22	0.332	0.495	0.625	1.880	0.326	0.363	0.258	0.252	984	223	-800	-5
4	800S162-97-GFM-2	18182	432.1	42.08	0.347	0.511	0.808	2.000	0.337	0.374	0.253	0.211	969	228	-408	-35
5	1200S250-97-DFM-1	36673	2073.8	17.68	0.725	0.879	0.905	2.000	0.656	0.729	0.577	0.387	906	472	-6015	-173
6	1200S250-97-DFM-2	37977	2069.5	18.35	0.732	0.883	0.925	2.000	0.680	0.755	0.538	0.361	929	498	-5215	-165
7	800S250-68-DFM-1	14007	546.1	25.65	0.881	1.018	1.089	2.000	0.830	0.923	0.571	0.408	942	673	-4983	-179
8	800S250-68-DFM-2	14148	550.7	25.69	0.892	1.023	1.109	2.000	0.821	0.912	0.538	0.440	920	700	-4346	-110
9	1000S200-43-LFM-1	11983	525.2	22.81	0.532	0.685	0.737	2.000	0.497	0.552	0.307	0.230	933	362	-4707	-61
10	1000S200-43-LFM-2	12045	526.2	22.89	0.524	0.675	0.738	2.000	0.483	0.536	0.279	0.176	920	356	-4074	-82
11	800S200-33-LFM-1	5575	243.8	22.87	0.550	0.698	0.752	2.000	0.526	0.585	0.283	0.193	957	396	-5569	-72
12	800S200-33-LFM-2	5632	244.6	23.02	0.549	0.684	0.751	2.000	0.510	0.567	0.274	0.218	929	421	-4384	-45

7.2 Cyclic Response Characterization

Strength and stiffness deterioration are simulated in *Pinching4* using damage rules that are a function of the hysteretic energy dissipated and the historic deformation demand [35, 36]. Three damage rules are available in *Pinching4*, to simulate strength, unloading stiffness and reloading stiffness deterioration. Both strength (Eq. 5.1) and unloading stiffness (Eq. 5.2) degradation were incorporated in the proposed hysteretic model whereas reloading stiffness deterioration was neglected. The damage rules are defined using the damage index for backbone strength, $\eta_{f,i}$, and damage index for stiffness, $\eta_{k,i}$, and are calculated using Eqs. (5.1) to (5.3). A least square fit method using Eq. (5.3) and experimental values of the damage index η_i calculated from the tests, were employed to obtain values β_i for each tested member. For the proposed hysteretic model, the damage was computed as a function of energy rather than peak deformations so the term relating damage to peak displacements was removed by setting $\beta_1 = \beta_3 = 0$.

7.2.1 Strength degradation

Strength deterioration was calculated as the positive difference on strength between the monotonic backbone moment ($f_{max,o}$) and the cyclic moment envelope ($f_{max,i}$). The strength degradation behavior is less pronounced for global buckling members than it is for the other members, see Fig. 7.3. The $f_{max,i}/f_{max,o}$ values close to one mean that the cyclic envelope is close to the monotonic envelope (see Fig. 6.6), and the strength has not been reduced due to damage accumulated during cyclic loading. For local and distortional buckling members strength degrades no more than 40% the corresponding strength under monotonic loading. It appears strength degrades more for members with higher cross-sectional slenderness (compare the averages λ_d =1.09 for distortional, and λ_ℓ = 1.77 for local buckling members); however, this correlation is not clear. In the *Pinching4* hysteretic model, the accumulation of damage is defined to be the same in both loading directions; hence, to define the degradation parameters β_2 and β_4 in Eq. 5.3, the average of the strength deterioration in both directions was used. The fitted β_i values fitted to each specimen's curve are listed in Table 5.2.

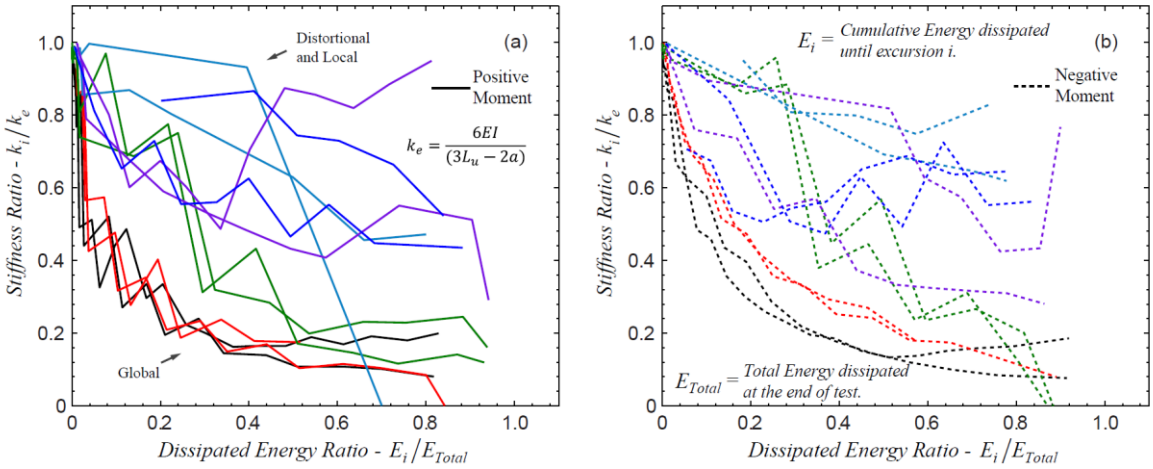

Fig. 7.2. Stiffness degradation, (a) positive moment; (b) negative moment.

7.2.2 Stiffness degradation

Unloading stiffness values were obtained by fitting a line to the unloading paths of the cyclic responses. The model is fit using a least squares method to minimize the error on the predicted load. The unloading stiffness is therefore the slope of segments *g-e* and *h-c* as shown in Fig. 7.2. Stiffness degradation for global buckling members is more pronounced than it is for the local and distortional buckling members. A reduction of more than 60% occurs before 20% of the hysteretic energy is dissipated for global members. For local and distortional members stiffness degradation is less than the global buckling members. It appears from Fig. 7.2 that there is no correlation between the amount of degradation and the cross-section slenderness besides the difference between global buckling members and the other members. As in the case with strength degradation, the average of the stiffness deterioration in both directions was used to develop the stiffness degradation parameters. The fitted β_i values are listed in Table 5.2.

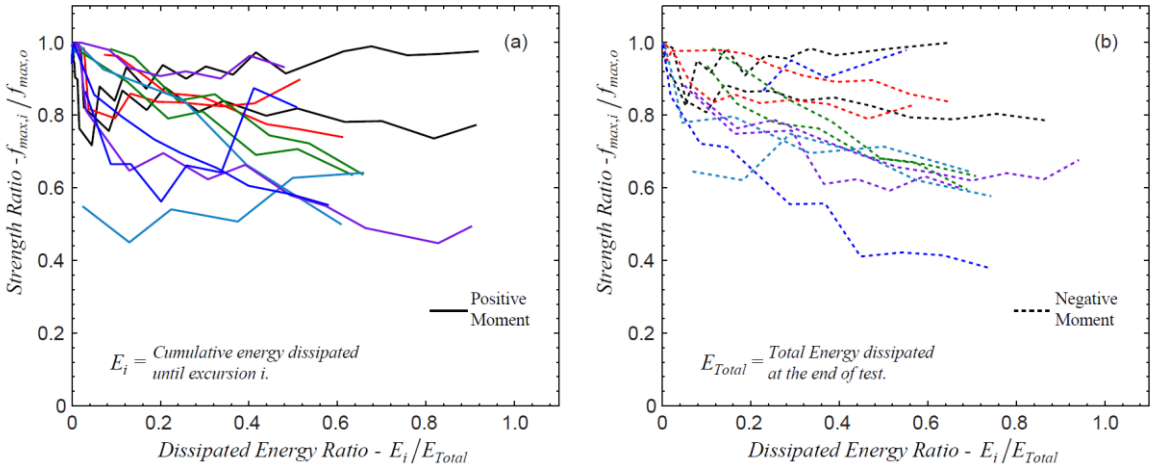

Fig. 7.3. Strength degradation, (a) positive moment; (b) negative moment.

7.2.3 Pinching behavior

The pinching behavior is defined by a set of pinching parameters, u_{M+}, u_{M-}, $r_{\theta+}$, $r_{\theta-}$, r_{M+}, and r_{M-}. The parameters $r_{\theta-}$ and $r_{\theta+}$ are the ratio of the deformation at which reloading starts (points *d* and *f* in Fig. 7.1) to the maximum/minimum historic deformation, θ_{min} and θ_{max}. The parameters r_{M-} and r_{M+} are the corresponding ratios of the load at the point at which reloading starts (points *d* and *f*) to the load corresponding to the maximum historic displacement, $f(\theta_{min})$ and $f(\theta_{max})$. The parameters u_{M-} and u_{M+} are the ratios of the load developed after unloading (point *c* and *e* in Fig. 7.1) to the load coordinate of backbone point 3, M_{3-} and M_{3+}.

An initial attempt to characterize pinching was made by fitting a tri-linear model to each unloading and reloading curve using a least squares method. The coordinates of the fitted points defining each segment were used to derive a first estimate of pinching parameters $r_{\theta+}$, $r_{\theta-}$, r_{M+}, r_{M-}, u_{M+}, and u_{M-} for every cycle. These values are not constant and varied as the number of cycles increased. Since the pinching behavior in *Pinching4* is defined using constant pinching parameters, the average was taken for these values. The values are listed in Table 7.2. Optimization of the *Pinching4* parameters is being carried out in the same fashion as described for the axial members in section 5.3 and generalization of the expression will be available in future conference/journal paper.

Table 7.2. *Pinching4* model parameters for each specimen.

Specimen	Damage Parameters						Pinching Parameters						
	Strength [a]		Stiffness [a]				Compression			Tension			Backbone
	β_2	β_4	β_2	β_4	γ_E	E_M [b]	$r_{\theta-}$	r_{M-}	u_{M-}	$r_{\theta+}$	r_{M+}	u_{M+}	Used [c]
1200S162-97-GFM-1	0.067	0.000	1.01	0.32	11.32	374.0	0.17	0.29	-0.18	0.20	0.32	-0.21	2
1200S162-97-GFM-2	0.250	0.347	1.11	0.38	6.51	381.3	0.23	0.33	-0.17	0.23	0.35	-0.21	2
800S162-97-GFM-1	0.237	0.318	1.18	0.46	7.71	360.2	0.22	0.33	-0.18	0.22	0.33	-0.19	4
800S162-97-GFM-2	0.304	0.806	1.08	0.39	8.51	372.3	0.21	0.32	-0.18	0.26	0.36	-0.21	4
1200S250-97-DFM-1	0.581	1.096	0.95	0.67	10.45	577.0	0.19	0.34	-0.20	0.20	0.38	-0.19	5
1200S250-97-DFM-2	0.510	0.694	1.04	0.72	10.83	562.4	0.10	0.27	-0.21	0.23	0.42	-0.17	5
800S250-68-DFM-1	0.398	0.000	0.49	0.74	7.16	353.7	0.22	0.36	-0.15	0.22	0.36	-0.19	7
800S250-68-DFM-2	0.519	0.572	0.92	1.61	5.74	351.1	0.15	0.29	-0.16	0.24	0.38	-0.19	7
1000S200-43-LFM-1	0.481	0.416	0.75	0.48	9.21	158.1	0.09	0.28	-0.19	0.21	0.41	-0.17	10
1000S200-43-LFM-2	0.486	0.736	0.35	0.31	17.86	141.1	0.07	0.21	-0.16	0.22	0.40	-0.18	9
800S200-33-LFM-1	0.703	0.495	0.58	0.41	11.95	69.8	0.11	0.30	-0.14	0.23	0.45	-0.19	11
800S200-33-LFM-2	0.212	0.000	0.35	0.02	14.68	69.9	0.11	0.29	-0.16	0.28	0.48	-0.11	11

(a) Fit using positive and negative excursions; (b) Energy in units of kN-mm; (c) Backbone curve from Table 7.1

8 Conclusions

Experimental investigation of cold-formed steel (CFS) axial and flexural members was investigated. The experimental responses were characterized and a hysteretic model was calibrated for axial and flexural members as part an effort to develop a computational efficient toolbox of nonlinear elements capable of accurately and efficiently simulating the seismic behavior of CFS members and the infinite number of possible configurations in cold-formed steel structures. A cyclic loading protocol was adapted from the FEMA 461 for testing of CFS structural components with target deformations defined using elastic buckling parameters. The following two sections summarize the conclusions from this study.

8.1 CFS Axial Members

Cold-formed steel axial members under cyclic loading can dissipate hysteretic energy, provide post-buckling stiffness and endure large axial deformations after buckling. The amount of strength degradation, stiffness degradation, and pinching of the hysteretic response varies for the different specimens; however, the behavior is similar across the different buckling modes, lengths and cross-sections considered. Post-peak strength reductions of more than 50% the peak load occurred at axial deformations larger than the elastic yielding deformation (i.e., $\delta/\delta_y > 1.4$ for global buckling and $\delta/\delta_y > 2.0$ for distortional and local buckling) in both monotonic and cyclic tests. Results shows that post-peak strength degradation in compression is independent of the cross-section and the length of the members. Unloading stiffness from compression was different for the different buckling modes and affected the amount of hysteretic pinching when reloading in tension. Stiffness degradation in compression was more pronounced in members with larger cross-sectional slenderness. In tension, strength and stiffness degradation was negligible and only started when tearing of the cross-section started.

Initial imperfections influenced the initial stiffness and peak strength of members under monotonic loading. The initial stiffness was generally less than it was for members under cyclic loading. Under cyclic loading the imperfections straightened out during the early tension excursions, thus reducing their influence on the initial stiffness and peak compressive strength.

Energy dissipation occurred through buckling deformations and cold bending in compression, and yielding in tension. Damage accumulated in single half-wave after the member reached the peak strength. A clear correlation was observed between cross-sectional slenderness and the total hysteretic energy dissipated within the damaged half-wavelength. The total energy dissipated within the damaged half-wave decreases with increasing cross-sectional slenderness (i.e., λ_ℓ or λ_d). The larger energy dissipation capabilities of less slender (locally stocky) members compared to members with larger cross-sectional slenderness is at the cost of cost of less cumulative axial deformation before tensile rupture. Based on these results, cold-formed steel axial members with small to intermediate cross-sectional slenderness experiencing local or distortional buckling could prove beneficial on seismic energy dissipation.

The cyclic axial responses of CFS members were characterized and a hysteretic model was calibrated including strength and stiffness degradation. Backbone curves were developed from monotonic tests for each specimens and generalized as a function of the three slenderness λ_e, λ_d and λ_ℓ. Parameters for the uniaxial material model *Pinching4* were derived based on the hysteretic energy dissipated for each specimen, and generalized as a function of the three slenderness λ_e, λ_d and λ_ℓ as well. The derived hysteretic models captured reasonably well the main characteristics of the experimental response such as strength degradation, stiffness degradation, and pinching behavior. This study identified improvements that could be made to the *Pinching4* model formulation to better capture the hysteretic response of CFS axial members. The study suggests different sets of coefficients β_2 and β_4 to capture the inherently different modes of damage accumulation (different in tension than in compression). The shape of the unloading-reloading curve from tension to compression could also be modified to better capture the cyclic buckling response.

8.2 CFS Flexural Members

Cold-formed steel flexural members can dissipate energy and provide post-buckling stiffness during cyclic loading even though the flanges and/or web have buckled. The amount of strength degradation, stiffness degradation, and pinching of the hysteretic response varies

for the different specimens; however, the behavior is similar across the different buckling modes, lengths and cross-sections considered. Flexural strength decreased rapidly/instantly after peak and decreased to a stable average flexural strength of $0.2M_y$, while enduring large deformations ($\theta/\theta_y>2$), a result important for seismic design. The unloading mechanism affected the amount of pinching observed. Energy dissipated through inelastic strains and cold-bending at the collapsed cross-section/s. Energy dissipation varied depending on the buckling mode and number of locations were damage accumulated along the unbraced length. Energy dissipation capabilities remained constant for members experiencing lateral torsional buckling while enduring large deformations. Members experiencing local and distortional buckling dissipated more energy per cycle but the dissipation capabilities rapidly decreased as flexural deformations increased. When damaged accumulated at more than one location along the unbraced length (i.e., two flexural hinges), the total cumulative deformation endured by the members was less as well as the total energy dissipated.

The tested monotonic capacity provides insight into the accuracy of current code strength prediction assumptions (e.g., AISI-S100-07 Section C.3.1.2.1 or Appendix 1.2.2.1) and the validity of the warping fixed boundary condition assumption at the loading points. Comparing the test-to-predicted strength between members experiencing lateral torsional buckling and the members experiencing local and distortional buckling, shows that the AISI-S100-07 strength prediction $M_{ne}=M_{cre}$, for $M_{cre}<0.56M_y$ is unconservative. Unconservative code-based predictions for cold-formed steel joists have been pointed out before [45], and the results add supporting evidence that imperfections should be considered for beams in the elastic buckling range, in the same way that they are considered for columns (i.e., $P_n=0.877P_{cre}$). Finite element and analytical studies suggest that the assumption of warping fixity could improve the test-to-predicted statistics. For example, if $k=0.6$ is assumed then M_{test}/M_n improves to 0.98 ($cov=0.04$) for the global buckling members tested.

9 Acknowledgements

The authors are grateful to the American Iron and Steel Institute (AISI) for supporting this project, to the AISI Project Monitoring Task Group especially Bonnie Manley, Ben Schafer, Jay Larson, Colin Rogers, Steve Tipping, and to ClarkDietrich Building Systems for the specimen donations. Special thanks to Dennis W. Huffman and Brett N. Farmer at the Structures and Materials Laboratory at Virginia Tech for their help preparing test specimens and test setup.

10 References

[1] AISI S213-07, North American Standard for Cold-Formed Steel Framing: Lateral Design. American Iron and Steel Institute, Washington, D.C. ANSI/AISI-S213-07. 2007.

[2] Shamim I., Rogers C. A. (2012). Numerical Modeling and Calibration of CFS framed shear walls under dynamic loading, Proceedings of the 21st International Specialty Conference on Cold-Formed Steel Structures, October 24-25, 2012, St. Louis, Missouri.

[3] FEMA, FEMA P695 - Quantification of Building Seismic Performance Factors, Federal Emergency Management Agency (FEMA), Document No. FEMA 965. 2009, Washington, D.C.

[4] Higginbotham, A. B., and Hanson, R. D., Axial Hysteretic Behavior of Steel Members. Journal of the Structural Division, 1976; 102(7), 1365-1381.

[5] Ikeda, K., and Mahin, S. A., Cyclic Response of Steel Braces. Journal of Structural Engineering, 1986; 112(2), 342.

[6] Tang, X., and Goel, S. C., Seismic Analysis and Design Considerations of Concentrically Braced Steel Structures. Report No UMCE 87-4, Department of Civil Engineering, The University of Michigan, Ann Arbor, MI. 1987.

[7] Papadrakakis, M., and Loukakis, K., Elastic-plastic hysteretic behaviour of struts with imperfections. Engineering Structures, 1987; 9(3), 162-170.

[8] Nonaka, T., An elastic-plastic analysis of a bar under repeated axial loading." International Journal of Solids and Structures, 1973; 9(5), 569-580.

[9] Sohal, I. S., and Chen, W. F., Local buckling and inelastic cyclic behavior of tubular sections. Thin-Walled Structures, 1988; 6(1), 63-80.

[10] Goel, S. C., Cyclic Post-Buckling Behavior of Steel Bracing Members. Stability and Ductility of Steel Structures Under Cyclic Loading. pp75-84 CRC Press, 1992.

[11] Goggins, J. M., Broderick, B. M., Elghazouli, A. Y., and Lucas, A. S., Behaviour of tubular steel members under cyclic axial loading. Journal of Constructional Steel Research, 2006; 62(1–2), 121-131.

[12] Popov, E. P., and Black, R. G., Steel Struts under Severe Cyclic Loadings. Journal of the Structural Division, 1981; 107(9), 1857-1881.

[13] Jain, A. K., Hanson, R. D., and Goel, S. C., Hysteretic Cycles of Axially Loaded Steel Members. Journal of the Structural Division, 1980; 106(8), 1777-1795.

[14] Popov, E. P., Mahin, Stephen A, and Zayas, V. A., Cyclic Inelastic Buckling of Thin Tubular Columns. Journal of the Structural Division, 1979; 105(11), 2261-2277.

[15] Yao, T., and Nikolov, P. I., Numerical Experiment on Buckling/Plastic Collapse Behavior of Plates under Cyclic Loading. Stability and Ductility of Steel Structures Under Cyclic Loading. pp203-214 CRC Press. 1992.

[16] Usami, T., and Ge, H. B., Cyclic behavior of thin-walled steel structures–numerical analysis. Thin-Walled Structures, 1998; 32(1–3), 41-80.

[17] Watanabe, E., Sugiura, K., Mori, T., and Suzuki, I., Modeling of Hysteretic Behavior of Thin-Walled Box Members. Stability and Ductility of Steel Structures Under Cyclic Loading. pp225-235 CRC Press. 1992.

[18] Calderoni, B., De Martino, A., Formisano, A., and Fiorino, L., Cold formed steel

beams under monotonic and cyclic loading: Experimental investigation. Journal of Constructional Steel Research, 2009; 65(1), 219–227.

[19] Ayhan, D., and Schafer, B.W., "Moment-Rotation Characterization of Cold-Formed Steel Beams Depending on Cross-Section Slenderness", Proceedings of the 15th World Conference on Earthquake Engineering, September 24-28, Lisbon, Portugal., 2012.

[20] Calderoni, B, Giubileo, C., and De Martino, A., "Assessment of Hysteretic Cyclic Behaviour of Plastic Hinge in Cold-Formed Steel Beams" Proceedings of the fifth international conference on behaviour of steel structures in seismic areas (STESSA) pp. 185-190., 2006.

[21] Calderoni, B, Giubileo, C., and Tarantino, M., "Influence of Connections on the Seismic Behaviour of Hybrid Hot-Rolled and Cold-Formed Steel Frames" Proceedings of the Seventh International Conference on Behaviour of Steel Structures in Seismic Areas (STESSA) pp. 517-522. 2012.

[22] Hsu, H.-L., Chi, P.-S., "Flexural Performance of Symmetrical Cold-Formed Thin-Walled Members Under Monotonic and Cyclic Loading." Thin-Walled Structures, 2003, Vol. 41, pp. 47-67.

[23] Wong, M.F., and Chung, K.F., "Structural Behaviour of Bolted Moment Connections in Cold-Formed Steel Beam-Column Sub-Frames", Journal of Constructional Steel Research, Vol. 58, pp. 253-274., 2002.

[24] Uang, C.-M., Sato, A., Hong, J.-K., and Wood, K., "Cyclic Testing and Modeling of Cold-Formed Steel Special Bolted Moment Frame Connections", Journal of Structural Engineering, Vol. 136, No. 8, pp. 953-960., 2010

[25] AISI-S100-07, North American Specification for the Design of Cold-Formed Steel Structural Members. American Iron and Steel Institute, Washington, D.C. ANSI/AISI-S100-07. 2007.

[26] SSMA Steel Stud Manufacturers Association, Product Technical Information, ICBO ER-4943P, <http://www.ssma.com>, December 15, 2011.

[27] Moen, C. D., Direct strength design for cold-formed steel members with perforations. Ph.D. dissertation, Johns Hopkins University, Baltimore. 2008.

[28] Schafer BW, Adany S. Buckling analysis of cold-formed steel members using CUFSM: conventional and constrained finite strip methods. In: Proceedings of the 18th international specialty conference on cold-formed steel structures. Orlando, FL, United states: University of Missouri-Rolla; 2006.

[29] ASTM. E8M-04, Standard Test Methods for Tension Testing of Metallic Materials (Metric). ASTM International, West Conshohocken, PA. 2004.

[30] Moncarz, P.D., and Krawinkler H., Theory and Application of Experimental Model Analysis in Earthquake Engineering. The John A. Blume Earthquake Engineering Center Report No. 50. 1981.

[31] AISI-S910-08, Test Method for Distortional Buckling of Cold-Formed Steel Hat Shaped Compression Members. American Iron and Steel Institute, Washington, D.C. ANSI/AISI-S910-08. 2008.

[32] Krawinkler, H., Loading histories for cyclic tests in support of performance assessment of structural components. The 3rd International Conference on Advances in Experimental Structural Engineering, San Francisco. 2009.

[33] FEMA, FEMA 461 - Interim protocols for determining seismic performance characteristics of structural and nonstructural components through laboratory testing, Federal Emergency Management Agency (FEMA), Document No. FEMA 461. 2007.
[34] Moen CD, Schafer BW. Experiments on cold-formed steel columns with holes. Thin-Walled Structures 2008; 46(10):1164–1182.
[35] Zeinoddini, V. M., Geometric imperfections in cold-formed steel members. Ph.D. dissertation, Johns Hopkins University, Baltimore. 2011.
[36] EOS Systems Inc., PhotoModeler help topics manual (build 2012.1.1.668), (http://www.photomodeler.com), Vancouver, Canada. 2012.
[37] ASTM-C955, Standard Specification for Load-Bearing (Transverse and Axial) Steel Studs, Runners (Tracks), and Bracing or Bridging for Screw Application of Gypsum Panel Products and Metal Plaster Bases. West Conshohocken, PA. 2009.
[38] Schafer B.W., Pekoz T. Computational modeling of cold-formed steel: characterizing geometric imperfections and residual stresses. Journal of Constructional Steel Research 1998; 47(3):193–210.
[39] VTechWorks, <http://hdl.handle.net/10919/18721> (Feb, 2013).
[40] Lowes, L., Mitra, N., and Altoontash, A., A Beam-Column Joint Model for Simulating the Earthquake Response of Reinforced Concrete Frames, PEER Report 2003/10, Pacific Earthquake Engineering Research Center, 2004.
[41] Mazzoni, S., McKenna, F., Scott, M. H., and Fenves, G. L., Open System for Earthquake Engineering Simulation User Command-Language Manual, OpenSees Version 2.0, Berkeley, California, 2009.
[42] Ayhan D.and Schafer B.W., Characterization of moment-rotation response of cold-formed steel beams. Proceedings of the Annual Stability conference, April 18-21, 2012, Grapevine, Texas.
[43] MATLAB (2011), Version 7.12.0.635. The Mathworks, Inc., www.mathworks.com.
[44] Padilla-Llano D., Moen C. D., Eatherton M., McAnallen L., Bruce T., "Compression-Tension hysteretic response of cold-formed steel C-section framing members.", Proceedings of the 21st International Specialty Conference on Cold-Formed Steel Structures, October 24-25, 2012, St. Louis, Missouri.
[45] Put, B., Pi, Y., and Trahair, N., "Lateral Buckling Tests on Cold-Formed Channel Beams." J. Struct. Engineering, 1999, 125(5), 532–539.

American Iron and Steel Institute

25 Massachusetts Avenue, NW
Suite 800
Washington, DC 20001

www.steel.org

Research Report RP 13-2